Uplift history of the Troodos ophiolite from the Late Cretaceous until Late Pleistocene

Five phases constrained from numerical modelling and field observations

Outcrop of the conglomerate within the Kakkaristra Formation on Cyprus nearby the Troodos ophiolite.

Robin de Waal
2635764
Supervisor Dr. A. Beniest
Second assessor Dr. W.P. Schellart

Amsterdam 31/07/2023
Master thesis
Code AM_1186, 27 ECTS

Abstract

The Troodos ophiolite on Cyprus is one of the few worldwide subaerially exposed pieces of oceanic crust and oceanic mantle, but the tectonic processes pushing an ophiolite undeformed subaerial is still an ongoing debate. The Troodos ophiolite formed during Turonian times in a supra-subduction zone setting simultaneously with the closure of the Neo-Tethyan Ocean. Uplift started with obduction initiation since the early to middle Late Cretaceous during north-south oriented convergence between Africa and Eurasia, emplacing the ophiolite on land, and is still ongoing today through serpentinization processes that are not well understood. During this project, the complete uplift history of the Troodos ophiolite since the Late Cretaceous is investigated with numerical models and fieldwork. The numerical models simulate the topographic variations that result from different types of footwall, including oceanic, oceanic-continental or continental lithospheres. With nine lithosphere-scale numerical models the topographic response was simulated, while varying the type of footwall, the convergence velocity and the subduction angle. Results showed that an oceanic originated lithosphere converging with 2 cm/year and varying dip angles of 13^{o} till 45 km depth followed by ~28^{o} is most likely to cause the uplift that is needed to explain the initial uplift of the ophiolite from the submerged seabed (~3.0 km depth below sea level) to sea level. From the field data, clasts originating from the ophiolite were analyzed in various conglomerates of the sedimentary cover and allowed the quantification of more recent uplift during the Miocene up to the Pleistocene. Calculated maximum and minimum uplift rates for the obduction event and deposition of all individual conglomerates, i.e. Pakhna, Nicosia, Kakkaristra and Fanglomerate Formations, distinguished four separate uplift phases and one erosional phase. The complete uplift history started with the obduction event causing 0.35 km uplift per Myr during the early to middle Late Cretaceous, constrained from the best fitting numerical model, followed by 0.02 km uplift per Myr during the 90^{o} counterclockwise rotation of the Troodos ophiolite in the Late Campanian-Maastrichtian times. The field analysis revealed that during the Miocene, uplift rates increased to 0.69 km/Myr, which coincides with initiation of the underthrusting of the Eratosthenes Seamount. The main uplift phase occurred during the Pliocene with uplift rates between 2.78 to 10.46 km/Myr, which is related to the accelerated serpentinization of mantle rocks by seawater. Since the Late Pleistocene, the Troodos ophiolite became subaerially exposed along with decreasing subduction velocities resulting in a final phase being erosional lacking an uplift component due to reduced compressive forces. The calculated uplift rates correlate properly with major tectonic events in the Eastern Mediterranean. Hence, combining numerical modelling and field observational data contributes to our knowledge about ophiolite obduction and provides more insight in the processes pushing an ophiolite subaerial.

Contents

Chapter 1 Introduction

1.1 Ophiolites

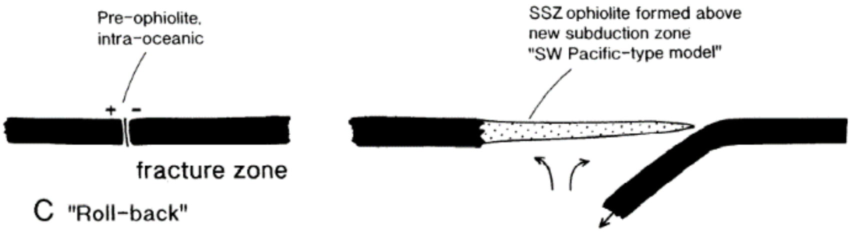

Figure 1.1 The proposed geologic setting in which a supra-subduction zone originating ophiolite forms (Robertson, 2004).

An ophiolite is an exposed piece of oceanic crust and oceanic mantle emplaced on land due to obduction (Robertson, 2004). Normally, oceanic crust forms at a mid-ocean ridge during seafloor spreading (Robertson, 2004), but based on geochemical evidence, authors do also plead for a supra-subduction zone (SSZ) or embryonic arc setting as origin for ophiolites (Morag et al., 2016; Robertson, 2004). A supra-subduction zone likely initiates along a transform fault once rollback, i.e. backward migration, of the subducting slab occurs. The created gap allows upwelling of the asthenosphere forming the future ophiolite (fig. 1.1; Robertson, 2004). The circumstances that allow dense oceanic lithosphere to be pushed upward, obducted and become subaerial instead of sinking into the asthenosphere (Morag et al., 2016) are still an ongoing debate.

Obduction occurs in a convergence subduction-related setting, in which either continental lithosphere, which collapsed prior to emplacement, underthrusts young, hence hot and buoyant oceanic lithosphere (Searle and Stevens, 1984), or the oceanic lithosphere overthrusts onto old and hence heavy oceanic lithosphere (Agard et al., 2007; Robertson, 1998a; Searle and Stevens, 1984). Obduction initiates once convergence velocities accelerate, changing the plate's visco-elastic behavior, resulting in an induced or spontaneous intra-oceanic subduction zone (Agard et al., 2007). In combination with regional tectonic and diapiric uplift due to collision and serpentinization, which occurs once saline surface or groundwater hydrate the mantle peridotites causing > 44% volume increase, respectively (Morag et al., 2016; Ring and Pantazides, 2019; Robertson, 1998a), the ophiolite will eventually become subaerial (Searle and Stevens, 1984). In the past, authors proposed several models causing the emplacement, consisting of uplift in the compressional regime emerged from convergence (Agard et al., 2007) and subsidence, e.g. caused by scraped off sediments from the subducting plate accreting to the overriding plate (Welland and Mitchell, 1977), of the ophiolite. However, there is not one single model explaining the emplacement and obduction of all ophiolites across the world. The present position of the ophiolites are possibly caused by a combination of various models (Searle and Stevens, 1984). Firstly, the Troodos ophiolite is emplaced by transform-fault processes. The Troodos massif was uplifted by the combination of major transcurrent movements together with minor subduction and thrusting components (Brookfield, 1977). Secondly, the Alpine-ophiolites are suggested to be emplaced by gravitational sliding processes, in which oceanic lithosphere gravitationally glided onto inactive continental margins due to intruding-extruding mantle material as a result of tension (Stoneley, 1975). Thirdly, the Semail ophiolite is suggested to be emplaced by gravitational induced thrusting, i.e. either by gravity sliding or spreading processes. The serpentinization of the metamorphic sole forms a low-friction, ductile-deformed decollement layer which, in combination with gravity forces by elevation differences, enables the ophiolite to slide or spread laterally along a trust fault (Searle and Malpas, 1980). Nevertheless, the obduction of the Semail Complex is also suggested to be caused by collision-subduction-accretion processes with a subduction polarity dipping either towards, i.e. Cordilleran-type (Searle and Stevens, 1984), or away (Searle and Stevens, 1984), i.e. Tethyan-type, from the continental margin. In a continent-arc collisional setting, the subducting continental lithosphere will start to underthrust underneath the oceanic overriding plate at a certain moment. During subduction, the friction scrapes off the sedimentary cover which accretes to the overriding plate. Obduction results from the combination of subduction, underthrusting and accretion (Welland and Mitchell, 1977).

1.2 Troodos ophiolite

The Troodos ophiolite, located on Cyprus, is an example of an ophiolite originating from an SSZ, either autochthonous or allochthonous (Whitechurch et al., 1984). This is one of the best preserved and minor deformed ophiolites, by obduction or post-obduction processes, in the world, making Cyprus an interesting site for geologists (Feld et al., 2017; Varga, 1991; Varga and Moores, 1985). Due to the good preservation, almost the entire sequence of oceanic lithosphere from pelagic sediments to mantle rocks is examinable (fig. 1.2; Feld et al., 2017; Morag et al., 2016).

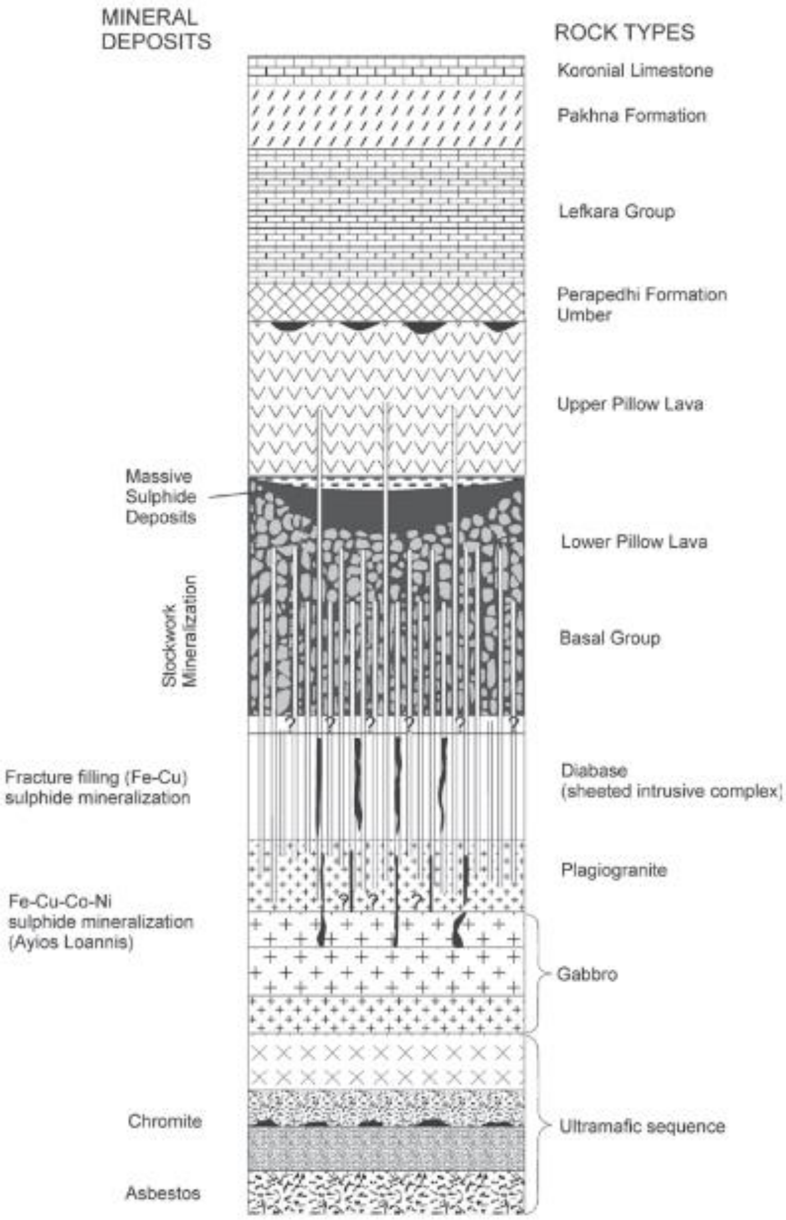

Figure 1.2 The Troodos ophiolite sequence on Cyprus (Robinson et al., 2003).

Hypothesis for obduction include two different settings in which either oceanic or thinned continental lithosphere subducts, i.e. oceanic lithosphere vs. continental lithosphere hypothesis, respectively (Khair and Tsokas, 1999). An alternative hypothesis includes both oceanic and continental lithospheres causing the obduction of the Troodos ophiolite (fig. 1.3). This hypothesis proposes that once the oceanic lithosphere is completely consumed during subduction, the continental lithosphere is pulled downward and starts to underthrust beneath Cyprus causing buoyancy-driven uplift (Khair and Tsokas, 1999; Morag et al., 2016). The ophiolite obducted from the north in a southward-vergence movement during the Late Mesozoic (Harrison, 2008). Once the ophiolite obducted, another mechanism is required to become subaerial. The Eratosthenes Seamount, located south of Cyprus (fig. 1.4), arrived at the southern edge of the now subaerial island of Cyprus during the Miocene and started to underthrust, resulting in surface uplift. As a consequence, the ophiolite is pushed subaerial, in combination with serpentinization, during the Plio- and Pleistocene, i.e. Quaternary times (Khair and Tsokas, 1999; Morag et al., 2016; Robertson and Xenophontos, 1993; Robertson, 1998a).

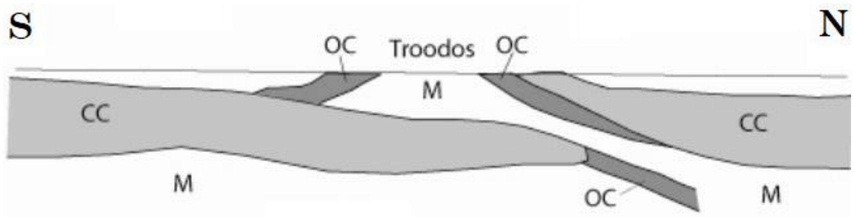

Figure 1.3 Oceanic crust (OC) followed by continental crust (CC) subduction into the mantle (M) due to a slab-pool force (Harrison, 2008; Morag et al., 2016).

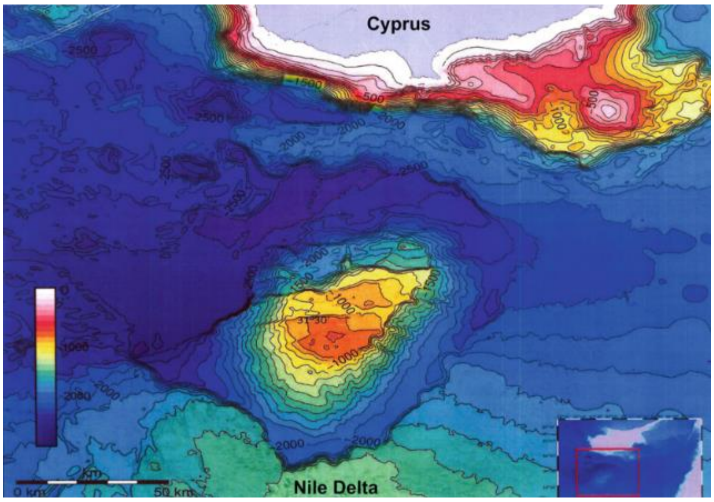

Figure 1.4 A bathymetric map showing the location of the Eratosthenes Seamount with respect to Cyprus (Papanikolaou, 2021).

Some authors plead for a continental origin causing the ophiolite to become subaerial, in which the Eratosthenes Seamount is either a rifted continental fragment from the African margin surrounded by oceanic lithosphere (fig. 1.5) or an extended part of the thinned North African crust underthrusting in northward direction underneath Cyprus (Morag et al., 2016; Papanikolaou, 2021; Robertson and Xenophontos, 1993; Robertson, 1998a).

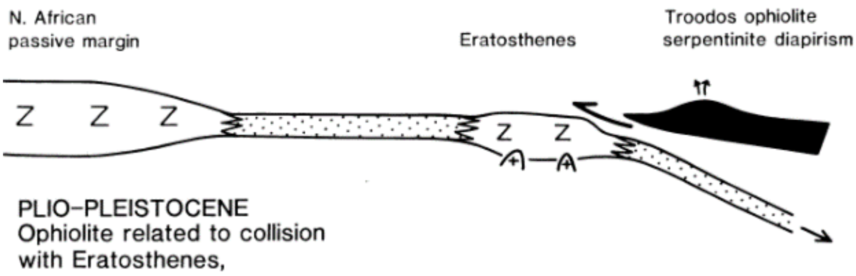

Figure 1.5 Scenario in which the Eratosthenes Seamount is a rifted continental fragment surrounded by oceanic lithosphere (Robertson, 1998b).

Others plead for an oceanic origin causing obduction and pushing the ophiolite subaerial. These authors provide evidence for an oceanic Eastern Mediterranean since the Triassic, in which the oceanic lithosphere dips northeastward underneath Cyprus (Robertson, 1998a). In this scenario, continental fragments rifted away from the large continents, forming a small ocean basin within the Eastern Mediterranean. Currently, this ocean basin undergoes closure (Khair and Tsokas, 1999). Additionally, the dome-shape structure of the Troodos ophiolite indicates serpentinite diapirism, implying an oceanic origin. Serpentinization reactions only occur during oceanic lithosphere subduction, instead of buoyant continental lithosphere subduction and/or collision, introducing the required water for the serpentinization-driven uplift (Morag et al., 2016). Furthermore, Feld et al. (2017) proposes another theory for the oceanic lithosphere hypothesis. According to these authors, ophiolite obduction occurred onto an oceanic originated Eratosthenes Seamount, consisting of the deeper gabbroic layer, i.e. 'gabbroic layer 3', of the ophiolitic, i.e. oceanic crustal and mantle, sequence (Feld et al., 2017).

1.3 Aim, objective and report structure

As outlined above, regional patterns within the Eastern Mediterranean do not clearly show if continental or oceanic domains are subducting underneath Eurasia (Robertson, 1998a). Knowing the nature of the Eratosthenes Seamount would allow us to identify the nature of the lithosphere. However, this data is currently not available, which is why different methods are used to investigate the nature of the subducting plate. My aim is to reject one or more hypotheses about the nature of the subducting lithosphere as explained in section 1.2.

The main research question of this master thesis is: '*What type of lithosphere subducted underneath the Troodos ophiolite during obduction and how did the subsequent uplift history lead to its subaerial exposure?'.* This is tested by 1) performing lithosphere-scale numerical modelling to simulate the topographic response to different types of lithosphere, and 2) complementing the uplift history with observations from the field. During the period of the 6th of February till 1st of May 2023, I have performed a coherent set of numerical models (see '*Chapter 3 Methodology'* for details). This includes testing what type of lithosphere makes up the footwall of Cyprus. Does the subducting plate consists of oceanic, continental or oceanic-continental material? Other parameters tested are the subduction angle and the convergence velocity, and how this contributes to uplift and the topography of the Troodos ophiolite. The field observations were made during the period of the 2nd till 14th of May 2023, to constrain the amount of uplift by later processes, e.g. serpentinization. By combining the numerical modelling and field observation data, the uplift history of the Troodos ophiolite is constrained based on various uplift rates during different time periods.

To reach the aim of this master thesis, this report is structured in multiple chapters. In 'Chapter 2: Geological setting', the regional tectonic evolution, local tectonic setting and earlier obtained evidence for obduction and uplift are described. 'Chapter 3: Methodology' includes how the numerical model operates and which model setups were used. Furthermore, this chapter contains a description of the sites visited during fieldwork and how the optical microscopy was performed. 'Chapter 4: Results' is divided in a numerical modelling, a field observations and an optical microscopy part. In 'Chapter 5: Discussion', the numerical model and field observation results are discussed. By combining the data, hypotheses about the origin of Cyprus' footwall are confirmed and/or rejected. The uplift history of the Troodos ophiolite is constrained based on calculated uplift rates throughout time. The main conclusions are given in 'Chapter 6: Conclusion', including recommendations for follow-up research.

Chapter 2 Geologic setting

2.1 Tectonic setting

2.1.1 Regional tectonic evolution

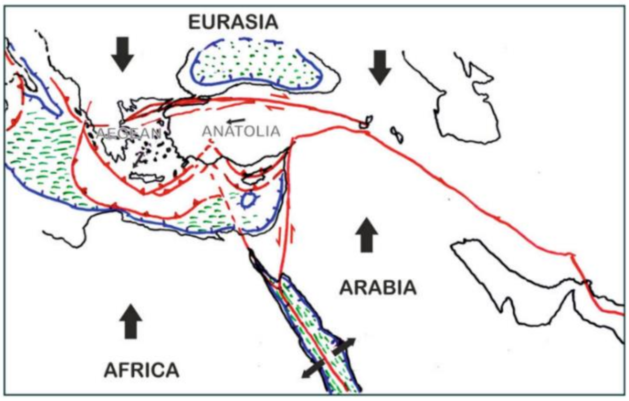

Figure 2.1 The major plate movements around Cyprus since the Middle Miocene (Papanikolaou, 2021).

The regional tectonic evolution in the Eastern Mediterranean started with the breakup of Gondwana during the early Mesozoic. During this time, the South Atlantic Ocean opened, which is the main driver of the tectonic deformations in the Eastern Mediterranean (Gaieb and Jallouli, 2017; Harrison, 2008). Other minor drivers affecting the tectonic evolution in the Eastern Mediterranean is the continued rifting of the Atlantic in northward direction breaking up Laurasia and opening the North Atlantic and Arctic Oceans (Harrison, 2008; Papanikolaou, 2021). This is followed by the collision of India with Eurasia during the Eocene and ends with Arabia separating from the African plate and colliding with Eurasia forming the Dead Sea, closing the Tethys Ocean, creating the Mediterranean and initiating westward escape tectonics of the Anatolian plate during the Miocene (fig. 2.1; Harrison, 2008; Papanikolaou, 2021).

Simultaneously with the breakup of Gondwana and the opening of the South Atlantic Ocean, northeastward convergence between the African and Eurasian plates began in the late Early Cretaceous ~120 Ma (Harrison, 2008; Robertson, 1998a). Within the southern Neo-Tethyan oceanic basin, a northward-dipping subduction zone initiated the closure of the Neo-Tethyan Ocean (Robertson, 1998a). The downgoing plate consisted of old, cold and hence heavy Triassic oceanic lithosphere (201 to 252 Ma), that was formed during Mesozoic times. Sheeted dyke orientations provided evidence that rollback of this oceanic slab created an east-west oriented spreading center offset by north-south oriented transform faults, known as the Arakapas fault zone on Cyprus (Dilek and Thy, 1990; Whitechurch et al., 1984). Extension resulted in a weak zone within the oceanic crust, i.e. intra-oceanic subduction zone (Robertson, 2004), allowing the asthenosphere to well up, forming the supra-subduction oceanic lithosphere for the later Troodos ophiolite in the forearc setting during Turonian times 91 $\pm$ 1.4 Ma, based on U-Pb ages (Clube and Robertson, 1986; Feld et al., 2017; Maffione et al., 2017; Wacey et al., 2014). The Troodos oceanic lithosphere is thus a remnant of the Neo-Tethyan ocean (Dilek and Flower, 2003; Morag et al., 2016; Robertson, 1998a). The time period covering subduction initiation, rollback, extension and magmatism is extremely short-lived, only 10 Myr (Morag et al., 2016). During the early to middle Late Cretaceous (90 Ma) convergence between Africa and Eurasia became more north-south oriented (Dilek and Thy, 1990). The proposed conceptual model (fig. 2.2) of Jolivet et al. (2016) is based on the regional geological observations and its convection regime in the large-scale tectonic evolutionary context, showing the orientation change is due to a northward asthenospheric flow, pushing these plates towards each other (Jolivet et al., 2016). This resulted in the subduction of the continental African margin due to the slab pull of the old and hence cold oceanic lithosphere. The old and cold continental lithospheric mantel started to underthrust below the young and hot oceanic lithosphere (Jolivet et al., 2016), initiating obduction (Robertson, 1998a). As a result of the continued convergence between the African and Eurasian plates, the Troodos ophiolite underwent a counterclockwise rotation of ~90^{o} during the Late Campanian-Maastrichtian, in which

~65° rotation accommodated before Maastrichtian times (McPhee and van Hinsbergen, 2019; Robertson, 1998a). Various authors argued that paleo-rotation occurred due to the oblique subduction of oceanic lithosphere underneath Troodos which was the driving force (Clube and Robertson, 1986; Morag et al., 2016), by comparing paleomagnetic data of lava samples and Lefkara sediments (Clube et al., 1985). Nevertheless, the most recent hypothesis explaining why the counterclockwise rotation occurred is due to a giant deep ring structure (GDRS) in the Eastern Mediterranean, centered underneath Cyprus. The presence of the GDRS is based on paleomagnetic, seismic tomography, mineralogical-petrological, tectonic and geodynamic data, polynomial approximations, residual gravity anomalies, GPS vector patterns and geoid isolines (Eppelbaum et al., 2020). Once rotation stopped, subduction velocities slowed down 25 Ma to ~14 mm/year, because the African northward plate motion reduced with respect to Eurasia (Reilinger et al., 2015). Since the Miocene, the Eratosthenes Seamount reached Cyprus and started to underthrust, causing the southward migration of the subduction zone (Khair and Tsokas, 1999; Robertson, 1998a). Hence, the Troodos ophiolite is uplifted and subaerially exposed since ca. 2 Ma (Ring and Pantazides, 2019; Robertson, 1998a). Concurrently, the subduction velocity decreased towards 6 to 10 mm/year (Saleh, 2013; Symeou et al., 2017) and is presently still ongoing in the Eastern Mediterranean (Papanikolaou, 2010).

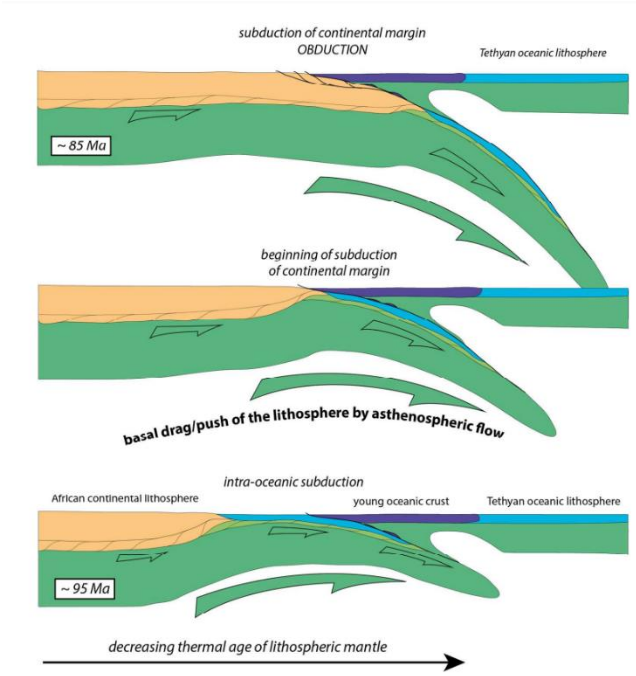

Figure 2.2 The conceptual model based on regional observations and its convection regime in the regional tectonic evolutionary context, showing obduction initiation (Jolivet et al., 2016).

2.1.2 Local tectonic setting Cyprus

Cyprus is an island located within the northeastern area of the Mediterranean Sea (Feld et al., 2017), along the northward subducting plate boundary between Africa and Eurasia marked by a 2.5 km deep active trench, known as the Giermann fault (fig. 2.3; McPhee and van Hinsbergen, 2019; Morag et al., 2016; Robertson, 1998a). The island formed by the merge of three large tectonic units: the Mamonia Complex, Troodos ophiolite and Kyrenia Range (fig. 2.4).

Figure 2.3 The location of Cyprus in the northeastern corner of the Mediterranean Sea (Google Earth, 2023).

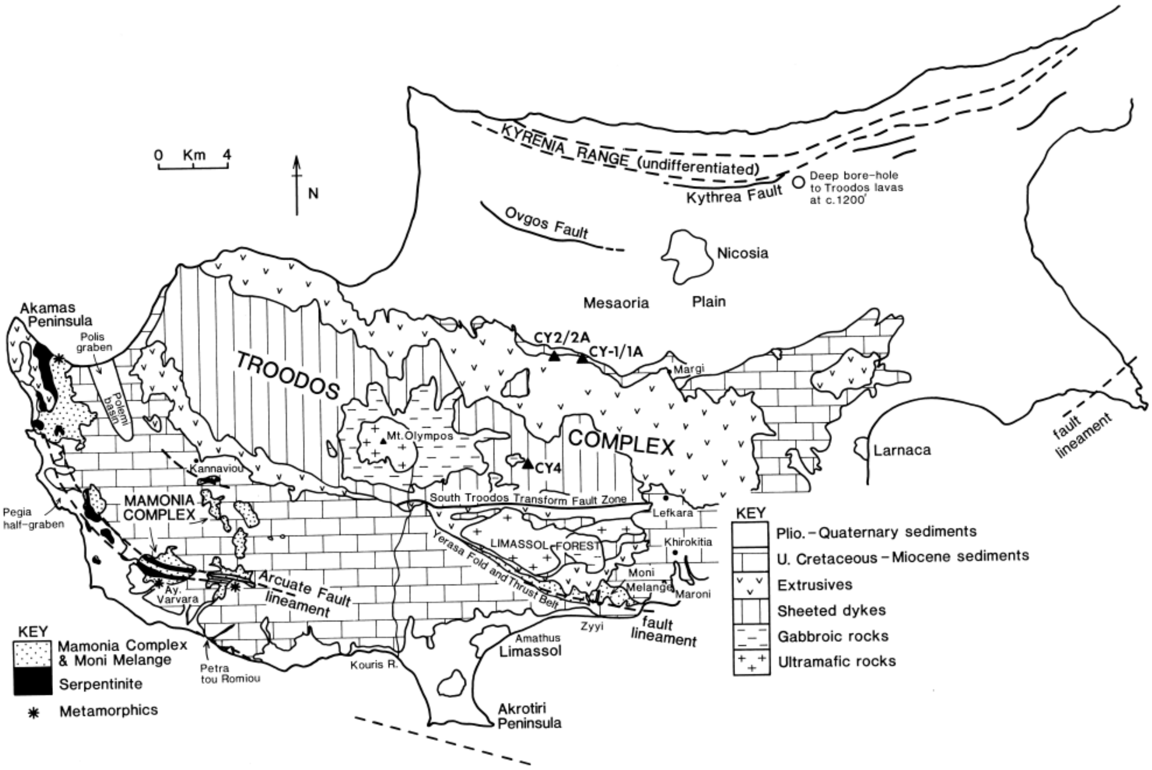

Figure 2.4 The location of the Mamonia complex in the southwest, Troodos ophiolite in the center and Kyrenia terrain in the north of Cyprus (Robertson, 1998a).

The Mamonia Complex in the southwestern corner consists of a chaotic assemblage of deformed sedimentary and volcanic rocks originating from oceanic domains and continental passive margins of Triassic to Early Cretaceous times (Maffione et al., 2017; McPhee and van Hinsbergen, 2019; Morag et al., 2016; Ring and Pantazides, 2019) and minor high-grade metamorphic rocks predating the Troodos ophiolite formation (Dilek and Thy, 1990; Ring and Pantazides, 2019). The accurate origin of the building blocks from the accretionary prism are still debated (Maffione et al., 2017). The center of the island is a gentle domal pericline originating from the Neo-Tethyan oceanic lithosphere, exposing the Penrose-type pseudostratigraphy of Late-Cretaceous age, known as the Troodos ophiolite (Maffione et al., 2017; Morag et al., 2016). The Mount Olympus, which is the highest peak of the island at 1,952 meters above sea level (a.s.l.), is located in the center of the Troodos massif (Ring and Pantazides, 2019). Nevertheless, Evans et al. (2021) divided the Troodos massif into two domains (fig. 2.5), firstly the western Olympus Domain containing partially serpentinized harzburgites (50-70%), and secondly the eastern Artemis domain containing completely serpentinized peridotites. The proposed simple 1D uplift model by the authors is based on the formula: *elevation = uplift - erosion* showing a variability in elevation between the two domains due to the differential serpentinization degrees of the harzburgites and peridotites (Evans et al., 2021).

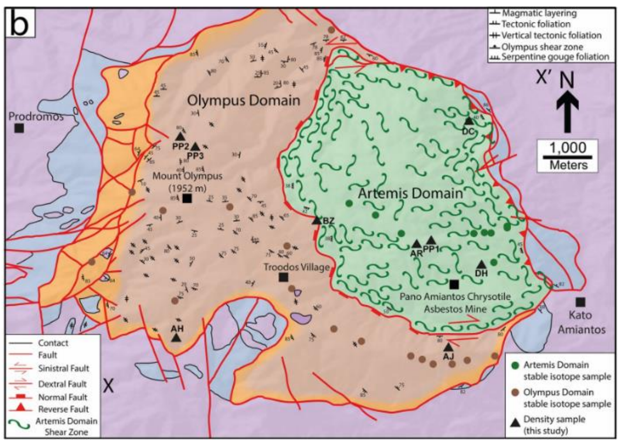

Figure 2.5 The subdivision of the Mount Olympus in the western Olympus Domain and eastern Artemis Domain based on varying serpentinization degrees (Evans et al., 2021).

The Mamonia Complex started to juxtapose the Troodos ophiolite during its counterclockwise rotation in the latest Cretaceous and is located along the extended part of the E-W oriented Arakapas fault zone, i.e. fossil transform fault (Dilek and Thy, 1990; Maffione et al., 2017; Ring and Pantazides, 2019). The Mamonia Complex and Troodos ophiolite are separated by a steep fault zone filled with serpentinite and they are sealed by mass flow deposits comprising pelagic sediments of Maastrichtian age, i.e. Lefkara Formation (Maffione et al., 2017; McPhee and van Hinsbergen, 2019). The movement along the Mamonia fault zone is proposed as either dip-slip thrusting, or right- or left-lateral oblique (McPhee and van Hinsbergen, 2019). The Arakapas fault zone actually separates the Limassol Forest Complex in the southeast from the Troodos ophiolite in the northwest (Dilek and Thy, 1990). The Limassol Forest Complex comprises intrusive and extrusive rocks, e.g. volcaniclastic rocks, pillowed and massive basaltic lavas, dykes, mafic plutons and tectonically deformed peridotite and serpentinite, from the oceanic lithosphere (Dilek and Thy, 1990). This part of the oceanic lithosphere underwent a more complicated tectonic and magmatic history compared to the main massif (Clube and Robertson, 1986).

The Troodos ophiolite is separated from the Kyrenia Range by the Ovgos fault. The Kyrenia Range is a narrow, steep mountain chain in the north of the island (McPhee and van Hinsbergen, 2019; Ring and Pantazides, 2019). The Kyrenia Range is a Miocene fold-and-thrust belt containing Late Paleozoic-Cenozoic volcanics, marine sediments and metamorphosed/recrystallized carbonates (Garzanti et al., 2000; Maffione et al., 2017; McPhee and van Hinsbergen, 2019; Morag et al., 2016; Ring and Pantazides, 2019).

2.2 Previous work

Previous work provides multiple lines of evidence for 1) the amount and movement of uplift, and 2) the fact that the Troodos ophiolite indeed obducted. In this sub-chapter, the different themes are reviewed and divided into the following sub-sub-chapters: the sedimentary stratigraphy, field observations and modelling.

2.2.1 Sedimentary stratigraphy

The first line of evidence is the sedimentary stratigraphy (fig. 2.6) within the Mesaoria Basin covering the Troodos ophiolite, documenting uplift from seabed towards ca. 2,000 meters a.s.l. (Kinnaird et al., 2011). The Troodos ophiolite is uncomfortably overlain by the Perapedhi Formation (90.3 – 83.0 Ma) (Gass, 1977; Gass et al., 1994). The 10 meters thick (Chen and Robertson, 2019) deep-marine pelagic sediments, i.e. radiolarites and umbers (Garzanti et al., 2000) are overlain by the Kannaviou Formation (83.0 – 74.0 Ma) consisting of a 750 meter thick (Chen and Robertson, 2019) volcanogenic facies deposition, deposited near or beneath the Carbon Compensation Depth (CCD) (Chen and Robertson, 2019; Clube and Robertson, 1986; Gass et al., 1994; Kinnaird et al., 2011). The pelagic carbonates and chalks of the Lefkara Formation are deposited at a depth of 2.6 to 3.2 km below sea level (Jenkyns and Winterer, 1982) in a contouritic environment during the Maastrichtian to Early Miocene (74.0 – 23.3 Ma) with a total thickness of 950 meters (Clube et al., 1985; Kinnaird et al., 2011; Payne and Robertson, 1995). Since the Miocene, the Eratosthenes Seamount started to underthrust (Robertson, 1998a). The initiation of uplift changed the deep-water depositional environment towards more hemi-pelagic/shallow marine circumstances depositing the 450 meters thick (Kinnaird et al., 2011) marly and silty pack- and grainstones, conglomerates and coral reefs of the Pakhna Formation during Miocene (23.3 – 6.5 Ma) times (Garzanti et al., 2000; Kinnaird et al., 2011; Payne and Robertson, 1995). Within the Pakhna formation, lava clasts from the Troodos ophiolite are found, indicating a short period in which the ophiolite was already partly exposed (Ring and Pantazides, 2019). The Messinian Salinity Crisis (6.5 – 5.2 Ma) resulted in the deposition of the 20 meters thick (Kinnaird et al., 2011) Kalavasos Formation containing evaporites and gypsum precipitations (Krijgsman et al., 1999; Payne and Robertson, 1995). At the end of the Miocene, the sea flooded the area, thereby again depositing the

280 meters thick (Kinnaird et al., 2011) shelf-depth marls with terrigenous silts, sands and conglomerates, i.e. diabase and lava clasts, of the Nicosia Formation in a deltaic setting during the Pliocene (5.2 – 2.5 Ma). The conglomerates within the Nicosia Formation indicate a second period of partly exposure of the uppermost ophiolite (Evans et al., 2021). The Athalassa, Kakkaristra and Apalos Formations mark the transition from shallow marine towards continental facies, in which biocalcarenites, sandstones and again conglomerates containing the first gabbroic clasts are deposited (Clube and Robertson, 1986; Evans et al., 2021; Kinnaird et al., 2011). The Athalassa and Kakkaristra Formations are together 100 meters thick (Kinnaird et al., 2011), deposited during the same time period 2.5 – 2.0 Ma (Payne and Robertson, 1995). The 45.5 meters thick (Schirmer et al., 2010) Apalos Formation is deposited 2.0 – 1.8 Ma within the Pleistocene epoch (Payne and Robertson, 1995) in a fluvial deposition environment (Poole and Robertson, 1998). Since 1.8 – 0.01 Ma, the ophiolite became completely subaerial and exposed to erosion and weathering (Payne and Robertson, 1995; Ring and Pantazides, 2019). The maximum 86 meters thick (Poole and Robertson, 1998) erosional products, i.e. non-marine ophiolite derived (ultramafic) clasts and sands (Gass et al., 1994), are deposited in a radial pattern around the Troodos massif in a fluvial environment within the Fanglomerate Formation (Clube and Robertson, 1986; Kinnaird et al., 2011). In the literature, the Fanglomerate Formation is subdivided into four members, namely F1 – F4. The individual units have various topographic levels and terrace ages. Furthermore, the composition of the matrix and how its sorted, as well as the clast size and angularity vary between the different conglomerates (Poole and Robertson, 1998). The subdivision within the Fanglomerate Formation is beyond the scope of this report.

Summarized, the at least 1,932 meter thick sedimentary stratigraphy includes sediments originating from deep marine shallowing-upwards conditions towards continental depositional environments. During the depositional evolution the stratigraphy was partly exposed in which ophiolitic derived erosion products, providing evidence for uplift, are deposited in the conglomerates since 5.2 Ma, followed by complete exposure delivering (ultra)mafic erosion products since 1.8 Ma. This evidence of pulsed uplift is found in the Mesaoria and Pissouri basins, and Polis Graben (Evans et al., 2021; Kinnaird et al., 2011).

2.2.2 Field observations

The second line of evidence that argues for at least two uplift phases, is based on field observations on serpentinite. Schuiling (2011) pleads for a completely vertical uplift movement based on the degree rocks are deformed.

2.2.2.1 Serpentinization

Serpentinization occurs when mantle rocks interact with seawater (Schuiling, 2011). During this transformation, the rocks expand with ~44%, causing a density reduction and change in rheology from dense, anhydrous and low permeable mantle rocks to light, hydrated and weak serpentinites (Evans et al., 2021; Ring and Pantazides, 2019; Schuiling, 2011). The main driving force of uplift is the volume increase proceeding by the following formula: $Mg_2SiO_4 + MgSiO_3 + 2\ H_2O \rightarrow Mg_3Si_2O_5(OH)_4$ (Ring and Pantazides, 2019; Schuiling, 2011), but also the decrease in density makes the serpentinite lighter compared to the overlying ophiolitic rocks. These forces result in serpentinite rising as a diapir (Schuiling, 2011) and isostatic uplift (Evans et al., 2021). Once iron is present in a large volume of hot seawater, iron converts to magnetite causing an even larger amount volume increase of up to 50% (Schuiling, 2011). On the highest peak of the Mount Olympus, highly serpentinized harzburgites and peridotites are found in previous studies (Evans et al., 2021; Ring and Pantazides, 2019; Schuiling, 2011). The remaining question is if this serpentinite diapir is the only mechanism responsible for this amount of uplift, or if other processes are involved.

2.2.2.2 Uplift movement

Schuiling (2011) provides field evidence to conclude that pure vertical movement of the serpentinized harzburgite diapir from the seabed towards present heights took place until at least Miocene times, but is probably still ongoing today, based on how much the surrounding overlying rocks are deformed. As mentioned earlier, the serpentinized harzburgites are the lowest section of the ophiolite sequence but are found at the highest peak (Mount Olympos 1,952 m a.s.l.) of the island. The overlying rocks, i.e. gabbro, sheeted dykes and pillow lavas, are barely deformed during the diapiric rise, except for some preferred orientation or foliation. The rock-seawater interaction was limited in these rock types, with only minor pyroxenes in the gabbro transformed towards amphiboles and some epidotization within the sheeted dyke complex. The glasses between the pillow lavas are not even broken during the geologic history of the Troodos ophiolite, which is interpreted as another indication for vertical uplift of the Troodos ophiolite. The sediments surrounding the Troodos massif show some upward bending due to the diapiric rise (Schuiling, 2011).

2.2.3 Modelling

The last line of evidence is based on modelling exercises. Porkoláb et al. (2021) provided 2D thermo-mechanical numerical simulations with an upper true free surface boundary in which obduction occurred in a subduction setting comprising an oceanic overriding and continental subducting plate. Obduction in such a setting is only possible if an intra-oceanic subduction zone initiates, starting oceanic lithospheric subduction, generating slab pull forces causing the continental passive margin to subduct underneath the oceanic overriding plate. However, the authors provided additional phases explaining the exposed continental window within the ophiolite. Once the continental passive margin subducted below the oceanic overriding plate, the continental upper crust decouples from the lower crust and lithospheric mantle. The localized thrusts enables the upward extrusion of the upper continental crust, causing uplift and gravity-driven extension in the oceanic overriding plate until breakup, followed by extruding continental upper crust towards the surface forming the continental window within the obducted ophiolite (Porkoláb et al., 2021).

Duretz et al. (2016) performed 2D thermo-mechanical numerical models investigating the crucial dynamical and physical parameters of the obduction mechanism. Once oceanic subduction initiates at a thermal anomaly, i.e. mechanically weak zone, in the vicinity of a continental passive margin, slab pull forces result in continental subduction enabling obduction initiation. The authors tested various parameters within their numerical models concluding the crucial parameters enabling obduction and ophiolite emplacement are 1) a certain amount of shortening, 2) including a strong continental crust, and 3) a thermal anomaly (Duretz et al., 2016).

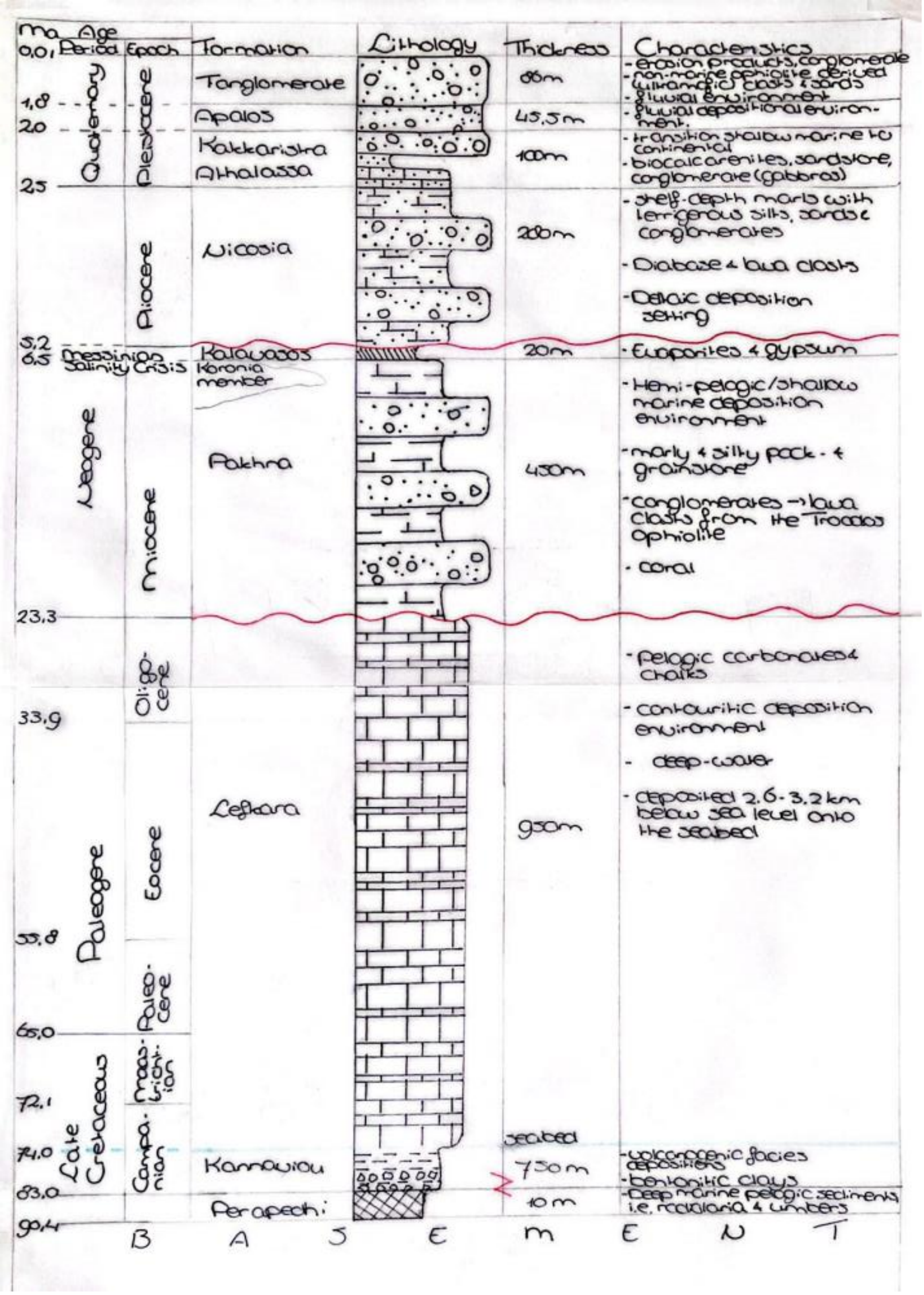

Figure 2.6 The sedimentary stratigraphy overlaying the Troodos ophiolite, i.e. basement, based on the individual formation descriptions in section '2.2.1 Sedimentary stratigraphy' by doing a literature review, including ages, formation names, thicknesses and characteristics. The stratigraphic column is an adjustment of the stratigraphic column in Gass et al. (1994), with thicknesses based on data in the Mesaoria basin by Kinnaird et al. (2011). Lithological patterns are from (Federal Geographic Data Committee, 2006) and fig. 1.2 (Robinson et al., 2003). Red curved lines indicate an unconformity. Vertical scale is based on formation thicknesses with 1 cm = 58.8 m.

Chapter 3 Methodology

3.1 Numerical modelling

3.1.1 Model operation description

A 2D thermo-mechanical numerical FLAMAR code, based on the FLAC-Para(o)voz algorithm, i.e. Fast Lagrangian Analysis of Continuum (Beniest et al., 2017; Le Pourhiet et al., 2004), is used to simulate the physical conditions of plate movements through time and identify boundary conditions for the obduction of the ophiolite on Cyprus, i.e. thermo-mechanical modelling. The code uses a mesh of Cartesian coordinate and solves the Newtonian equation of motion in the hybrid explicit finite element/difference code (Le Pourhiet et al., 2004; Yamato et al., 2007; Yamato et al., 2008). The code also solves constitutive laws such as the 2D large-strain Lagrangian formulas including the heat transfer equation, which is correlated with functions for non-Newtonian viscoelastic behavior material solved with the Maxwell equation and the Mohr-Coulomb failure criteria to solve elastoplastic behavior of material, the Boussinesq approximation and surface boundary conditions, i.e. linear diffusion equation. Once the model runs, strain rate, temperature, state of stress, thermal density variations, evolution of visco-elasto-plastic rheology and topography formation due to deformations of the lithosphere are calculated (Beniest et al., 2017; Yamato et al., 2007; Yamato et al., 2008). Within the model, all rheologies are usable (Le Pourhiet et al., 2004) requiring no pre-imposed internal boundary conditions (Yamato et al., 2008), enabling any plate to deform freely over time (Yamato et al., 2007). Within the existing numerical codes, parameters were adjusted based on geophysical and geological evidence known in the literature (Beniest et al., 2017; Burov, 2011). The thermo-rheological and mechanical parameters are listed in table 3.1. The used model setups after doing a literature review, are described below.

Thermal parameters	**Thermal property**	**Value**	**Unit**	**Reference**
	Surface temperature	0	°C	(Beniest et al., 2017)
	Temperature at the base of the crust	500	°C	
	Temperature at the base of the thermal lithosphere	1330	°C	
	Temperature mantle anomaly	1400	°C	
	Thermal conductivity crust	2.5	W/m °C	
	Thermal conductivity mantle	3.5	W/m °C	
	Radiogenic heat production at the surface	1.0E-9	W/kg	
	Radius radiogenic heat	10	km	
	Thermo-tectonic age of the lithosphere	2	Myr	
	Surface heat flow	40	mW/m^2	
	Mantle heat flow	15	mW/m^2	
Mechanical parameters	**Mechanical property**	**Value**	**Unit**	**Reference**
Oceanic overriding plate				
Oceanic crust *Ocean basalt*	Density Viscosity parameter (N) Viscosity parameter (A) Viscosity parameter (E)	2850 4.7 1.9E2 4.85E5	Kg/m^3 $MPa^{-n}s^{-1}$ J/mol	(Mackwell et al., 1998)
Oceanic lithosphere *Dry olivine*	Density Viscosity parameter (N) Viscosity parameter (A) Viscosity parameter (E)	3300 1 7.7E-9 5.36E5	Kg/m^3 $MPa^{-n}s^{-1}$ J/mol	(Karato et al., 1986)
Serpentinite	Density	2750	Kg/m^3	(Hirth and Kohlstedt, 1996)

Wet olivine	Viscosity parameter (N) Viscosity parameter (A) Viscosity parameter (E)	3.5 4.876E6 5.15E5	 $MPa^{-n}s^{-1}$ J/mol	
Oceanic subducting plate				
Oceanic crust *Ocean basalt*	Density Viscosity parameter (N) Viscosity parameter (A) Viscosity parameter (E)	2900 4.7 1.9E2 4.85E5	Kg/m^3 $MPa^{-n}s^{-1}$ J/mol	(Mackwell et al., 1998)
Oceanic lithosphere *Dry olivine*	Density Viscosity parameter (N) Viscosity parameter (A) Viscosity parameter (E)	3350 1.0 7.7E-9 5.36E5	Kg/m^3 $MPa^{-n}s^{-1}$ J/mol	(Karato et al., 1986)
Continental subducting plate				
Upper crust *Dry quartz*	Density Viscosity parameter (N) Viscosity parameter (A) Viscosity parameter (E)	2600 3.0 6.8E-6 1.56E5	Kg/m^3 $MPa^{-n}s^{-1}$ J/mol	(Ranalli and Murphy, 1987)
Lower crust *High density*	Density Viscosity parameter (N) Viscosity parameter (A) Viscosity parameter (E)	3050 3.05 6.8E-6 2.76E5	Kg/m^3 $MPa^{-n}s^{-1}$ J/mol	
Continental lithosphere *Peridotite*	Density Viscosity parameter (N) Viscosity parameter (A) Viscosity parameter (E)	3330 3.5 2.5E4 5.32E5	Kg/m^3 $MPa^{-n}s^{-1}$ J/mol	(Ranalli, 2000)
Asthenosphere *Wet olivine*	Density Viscosity parameter (N) Viscosity parameter (A) Viscosity parameter (E)	3275 3.0 1.0E4 5.1E5	Kg/m^3 $MPa^{-n}s^{-1}$ J/mol	(Goetze and Evans, 1979)

Table 3.1 Summary of the used mechanical and thermal parameters during this study.

3.1.2 Initial oceanic lithosphere geometry and parameter testing

The model setup is based on geological and geochemical evidence (Yamato et al., 2008). The initial geometry (fig. 3.1D) is achieved by running several test models, in which the geometry, size of the model box including the plate length (Xue et al., 2020), serpentinite thickness and density of the serpentinite are varied (fig. 3.1 and table 3.2). The initial oceanic geometry of Model 1 has a dip angle of 30°, because the subduction zone beneath Cyprus dips toward the NNW with an angle of 25° to 30° (Khair and Tsokas, 1999). In Model 1 is, furthermore, the subduction velocity of the subducting plate set at 2 cm/year (Reilinger et al., 2015). The model box size of Model 1 has a length of 1500 km and depth of 400 km, resulting in a grid size of 601 x 161 nodes, which gives a resolution of 2.5 x 2.5 km per cell (Beniest et al., 2017).

The oceanic crustal thicknesses are based on a thickness-age correlation. An age of 2 Myr correlates with a thickness of 4.6 – 6 km, while an age of 111 to 162 Myr correlates with a thickness of 6.7 – 8 km (Burov, 2011; Van Avendonk et al., 2017). In Model 1, the overriding plate consists of 5 km thick oceanic crust with a lithospheric thickness of 35 km, though the subducting plate consists of an 8 km thick oceanic crust (Ergün et al., 2005; Garzanti et al., 2000), a 50 km thick oceanic lithosphere and a serpentinite layer of 8 km thick, which is the driving force of subduction (Robertson, 1998a). The rheological strength diagrams of the oceanic overriding and oceanic subducting plates are added in figures 3.2 and 3.3. The model runs for 10 Myr, because the Neo-Tethyan ophiolites, including Troodos, formed and obducted in a relatively short time span of ca. 10 Myr (Dilek and Flower, 2003).

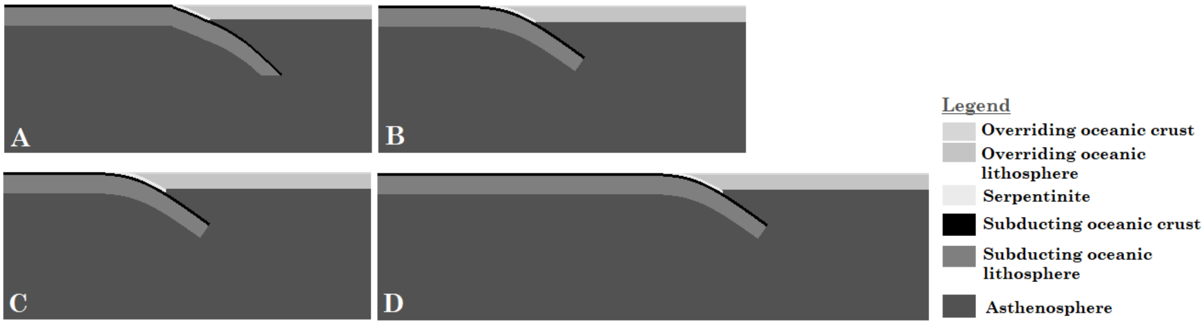

Figure 3.1 The tested geometries to achieve the initial oceanic geometry of Model 1. Figure B is an improved geometry of A. Figure C has the same model setup as B, but with a serpentinite layer of 10 km thick. Figure D, i.e. Model 1, is similar as B, but with a larger model box size, i.e. plate length (Xue et al., 2020), showing the geometry of 'Oceanic models' 1 and 3 to test the oceanic lithosphere hypothesis.

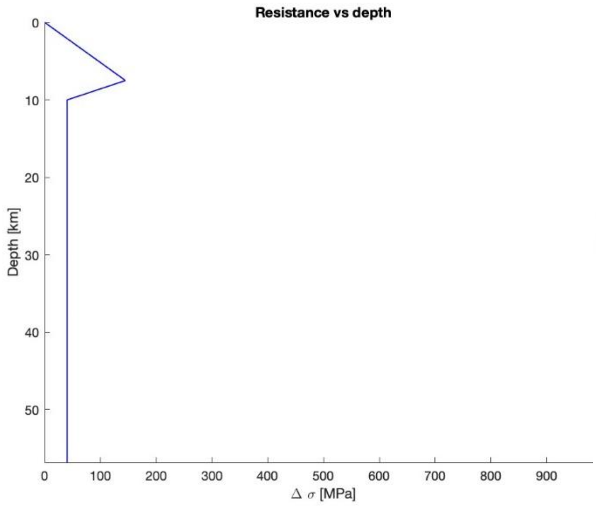

Figure 3.2 Rheological strength model of the oceanic overriding plate.

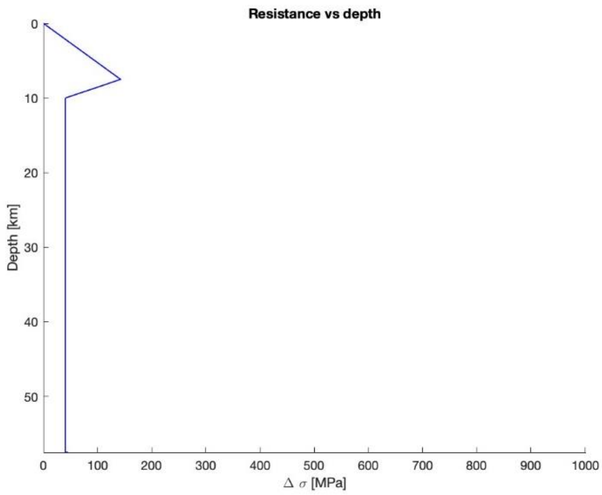

Figure 3.3 Rheological strength model of the oceanic downgoing plate.

3.1.3 Varying oceanic lithosphere models based on the initial oceanic geometry

The model setup of Model 2 is similar as the setup of Model 1, in which oceanic lithosphere subducts with 2 cm/year but has another geometry (fig. 3.4). In the literature, some authors plead for a varying dip angle of the subducting plate, which dips with 13° till 45 km depth, followed by a dip angle of ~28° (Feld et al., 2017) testing how subduction angle affects the results.

Oceanic model setups of Models 3 and 4 test how subduction velocity affects the results, since this parameter is uncertain. An exact convergence rate between the African and Eurasian plates during the middle to early Late Cretaceous was not obtained during the literature review. Based on knowledge that the northward motion of the African plate with respect to Eurasia slowed down 25 Ma to 14 mm/year, indicates that convergence rates were higher in the past (Reilinger et al., 2015). Therefore, these geometries are similar as Models 1 (fig. 3.1D) and 2 (fig. 3.4) but subduction velocity increased to 3 cm/year.

Figure 3.4 The geometry of ‘Oceanic models’ 2 and 4 to test the oceanic lithosphere hypothesis. Colors are used as in fig. 3.1.

Model	Size (km)	Size (nodes)	Serpentinite thickness (km)	Serpentinite density (kg/m^3)	Geometry	OO or TCO subduction?	Rheological strength diagram overriding plate	Rheological strength diagram subducting plate	Dip-angle	Velocity
A	1000 x 400	401 x 161	8	2950[1]	Fig. 3.1A	OO	Fig. 3.2	Fig. 3.3	30°	2 cm/year
B	1000 x 400	401 x 161	8	2950[1]	Fig. 3.1B	OO	Fig. 3.2	Fig. 3.3	30°	2 cm/year
C	1000 x 400	401 x 161	10	2950[1]	Fig. 3.1C	OO	Fig. 3.2	Fig. 3.3	30°	2 cm/year
D	1000 x 400	401 x 161	8	2750[2]	Fig. 3.1B	OO	Fig. 3.2	Fig. 3.3	30°	2 cm/year
E	1000 x 400	401 x 161	10	2750[2]	Fig. 3.1C	OO	Fig. 3.2	Fig. 3.3	30°	2 cm/year
1	1500 x 400	601 x 161	8	2750[2]	Fig. 3.1D	OO	Fig. 3.2	Fig. 3.3	30°	2 cm/year
2	1500 x 400	601 x 161	8	2750[2]	Fig. 3.4	OO	Fig. 3.2	Fig. 3.3	13° till 45 km depth, ~28°	2 cm/year
3	1500 x 400	601 x 161	8	2750[2]	Fig. 3.1D	OO	Fig. 3.2	Fig. 3.3	30°	3 cm/year
4	1500 x 400	601 x 161	8	2750[2]	Fig. 3.4	OO	Fig. 3.2	Fig. 3.3	13° till 45 km depth, ~28°	3 cm/year
5	1500 x 600	601 x 241	8	2750[2]	Fig. 3.5	TCO	Fig. 3.2	Fig. 3.6	30°	2 cm/year
6	1500 x 600	601 x 241	8	2750[2]	Fig. 3.7	OO + TCO	Fig. 3.2	Fig. 3.6	30°	2 cm/year
7	1500 x 600	601 x 241	8	2750[2]	Fig. 3.8	OO + TCO	Fig. 3.2	Fig. 3.6	13° till 45 km depth, ~28°	2 cm/year
8	1500 x 600	601 x 241	8	2750[2]	Fig. 3.7	OO + TCO	Fig. 3.2	Fig. 3.6	30°	3 cm/year
9	1500 x 600	601 x 241	8	2750[2]	Fig. 3.8	OO + TCO	Fig. 3.2	Fig. 3.6	13° till 45 km depth, ~28°	3 cm/year

Table 3.2 Summary of the varied parameters to obtain the initial geometry of Model 1 [1](Mackwell et al., 1998) [2](Hirth and Kohlstedt, 1996). Models A to E are test models to achieve the reference model 'Model 1'. The models identified with numbers are performed in this study. OO = Oceanic-Oceanic subduction; TCO = Thinned Continental-Oceanic subduction.

3.1.4 Adjusted models based on the initial oceanic geometry

To test the thinned continental lithosphere subduction hypothesis (Robertson, 1998b), the initial oceanic geometry of Model 1 is adjusted.

In the model setup of Model 5, all input parameters are the same as the setup of Model 1, except the geometry of the subducting plate and model box size have changed to a continental setting (fig. 3.5). The subducting plate subducts with an angle of 30° (Khair and Tsokas, 1999), a velocity of 2 cm/year (Reilinger et al., 2015), a serpentinite thickness of 8 km with a density of 2750 kg/m^3 (Hirth and Kohlstedt, 1996). The thinned continental lithosphere is divided into a 12 km thick upper crust (Lau et al., 2015), 22 km thick lower crust (Luccio and Pasyanos, 2007; Welford et al., 2015) and a continental lithospheric thickness of 55 km based on the lithosphere-asthenosphere boundary at 90 km depth (Saleh, 2013). The geometry for the overriding plate did not change. The rheological strength diagrams of the oceanic overriding and continental subducting plates are added in figures 3.2 and 3.6. To ensure a long enough plate length for subduction, the model box size increased to 1500 km long and 600 km deep, i.e. 601x241 nodes.

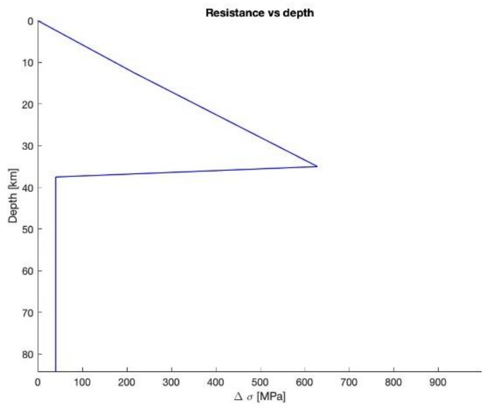

Figure 3.6 Rheological strength model of the continental downgoing plate.

Figure 3.5 The geometry of 'Continental model' 5 to test the continental lithosphere hypothesis.

3.1.5 Alternative models

To test the oceanic-continental lithosphere hypothesis (Harrison, 2008; Khair and Tsokas, 1999; Morag et al., 2016), a new geometry is required.

The setup of Model 6 is a combination of Models 1 and 5. The subducting plate subducts with an angle of 30° (Khair and Tsokas, 1999), a velocity of 2 cm/year (Reilinger et al., 2015) and a serpentinite thickness of 8 km with a density of 2750 kg/m^3 (Hirth and Kohlstedt, 1996). The subducting plate starts with an 8 km thick oceanic crust (Ergün et al., 2005; Garzanti et al., 2000) and a 50 km thick oceanic lithosphere, followed by thinned continental lithosphere divided into a 12 km thick upper crust (Lau et al., 2015), 22 km thick lower crust (Luccio and Pasyanos, 2007; Welford et al., 2015) and a continental lithospheric thickness of 55 km based on the lithosphere-asthenosphere boundary at 90 km depth (Saleh, 2013). The geometry of the overriding plate, as well as the model box size of 601x241 nodes, did not change (fig. 3.7).

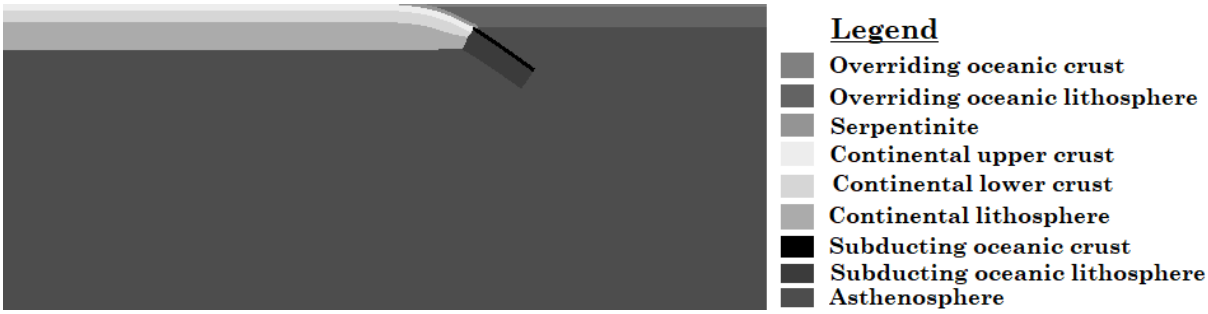

Figure 3.7 The geometry of 'Oceanic-continental models' 6 and 8 to test the oceanic-continental lithosphere hypothesis.

The setup of Model 7 is an adjustment on Models 2 and 6, testing how subduction angle affects the results. In the literature, some authors plead for a varying dip angle of the subducting plate, which dips with 13° till 45 km depth, followed by a dip angle of ~28° (Feld et al., 2017). In this geometry the continental lithosphere subducts with 13° till 45 km depth, followed by oceanic lithosphere subducting with ~28° (fig. 3.8). This distinction is based on continental and oceanic crustal and lithospheric densities. Continental crust has a lower density, causing more resistance to subduction, whereas the heavier oceanic crust subducts easier (Zheng, 2012).

The model setups of Models 8 and 9 test how subduction velocity affects the results. These geometries are similar as Models 6 (fig. 3.7) and 7 (fig. 3.8) but with a subduction velocity of 3 cm/year.

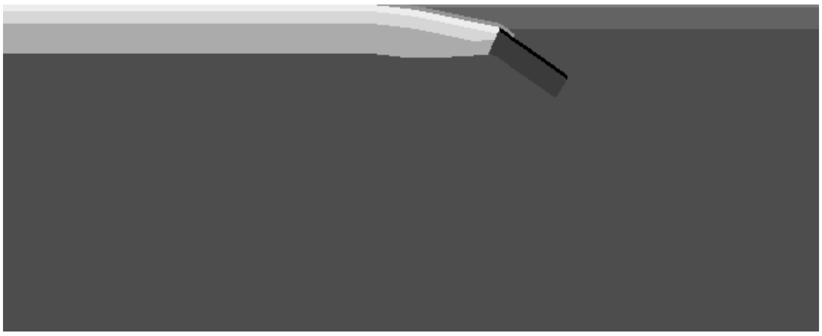

Figure 3.8 The geometry of 'Oceanic-continental models' 7 and 9 to test the oceanic-continental lithosphere hypothesis. Colors are used as in fig. 3.7.

3.1.6 Model result descriptions

The numerical modelling results are described in '*Chapter 4.1 Numerical modelling*' and focusses on the topographic expression after 10 Myr. The topography in a typical subduction zone consists, from the subducting plate across the trench to the overriding plate, of four main features (fig. 3.9), namely 1) the outer rise, i.e. viscous forebulge, 2) the subduction trench, 3) the collisional high and/or island- or volcanic-arc, and 4) the back-arc depression, i.e. a basin. The outer rise, i.e. viscous forebulge, is an uplifted area on the subducting plate that forms in response to the downward bending of the subducting plate. Above the collision zone, the trench forms a depression. The collisional high forms due to continuous plate convergence causing compression and an elevated region. In nature, an island- or volcanic-arc develops in this region as well, but in my models magmatism is not simulated and thus topography is created only through tectonic activity. The back-arc depression, i.e. a basin, is formed by the downward deflection of the overriding plate, located in the hinterland behind the collisional high and/or island- or volcanic-arc (Crameri et al., 2017). For each individual model, variations in strain rate, topography and deformation patterns of the system are described after 10 Myr of simulations, because I am interested in the long-term response of topography to subduction. Figures and graph of the phases, topography and strain rate of all models can be found in Appendix A.

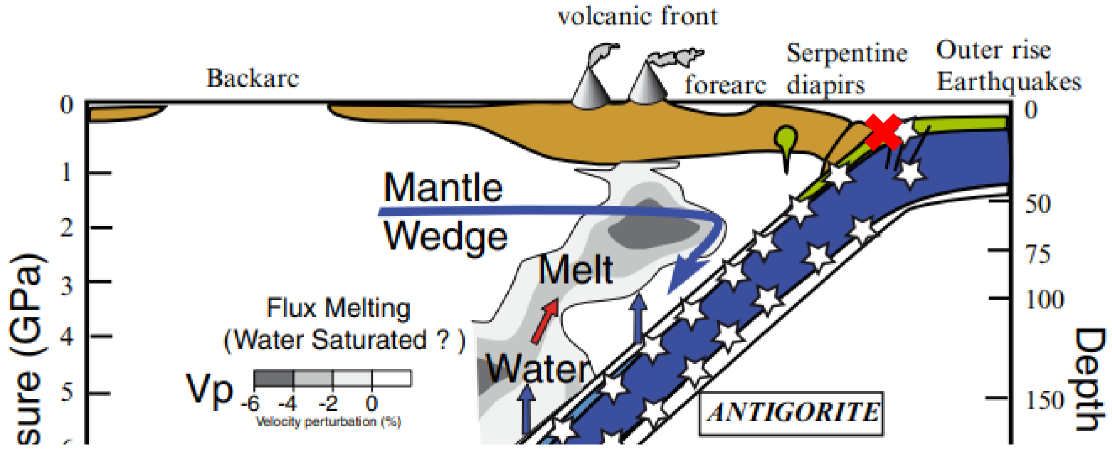

Figure 3.9 The typical subduction setting geometry containing the four main features from right to left: 1) the outer rise, i.e. viscous forebulge, 2) the subduction trench indicated with the red crotch, 3) the volcanic front and/or collisional high, and 4) the back-arc depression, i.e. a basin (Lallemand and Funicello, 2009).

3.2 Fieldwork

From 2 to 14 May 2023, fieldwork was performed with a team of two students, Demi Schutte and Robin de Waal, and one supervisor, Anouk Beniest. We investigated the conglomerates within the Pakhna, Nicosia, Kakkaristra and Fanglomerate Formations to quantify the amount of uplift from the Miocene until the Quaternary. To identify clasts within the conglomerates, we did a reconnaissance of the ophiolite units from the mantle sequence (harzburgites) towards the first sedimentary deposits (Lefkara and Pakhna Formations). The sedimentary formations in between the mafic rocks of the oceanic lithosphere and the conglomerates, e.g. Lefkara, Kalavasos, Athalassa and Apalos Formations, were also examined to investigate changes in depositional environments.

The sites visited (fig. 3.10 & table 3.3) are determined by using the Cyprus Geology and Geochemistry field excursion guidebook (AM_450229), studies found in the literature (Follows, 1990; McCallum, 1989; McCallum and Robertson, 1995; Poole and Robertson, 1998; Schirmer et al., 2010), the Geological Survey Department of Cyprus, Geological map of Cyprus and Geological Sites known by Cyprus' government. For each outcrop, a general description about the matrix was made, followed by a more detailed description of the clasts within the outcrop. To determine the sphericity (fig. 3.11) and sortedness (fig. 3.12) of the conglomerates, the '*Onderwijslint voorbereiding veldwerk 1*' from University Utrecht was used (Trabucho Alexandre, 2017).

Figure 3.10 Overview of the visited sites in the period 2nd till 14th of May 2023. Red pins are Pakhna conglomerates, orange pins are Nicosia conglomerates, black pins are Kakkaristra conglomerates and green pins are Fanglomerate conglomerates. The yellow pins are all other formations, i.e. Lefkara, Kalavasos, Athalassa and Apalos, and locations where serpentinite was collected for D. Schutte (Google Earth, 2023). Coordinates are included in table 3.3.

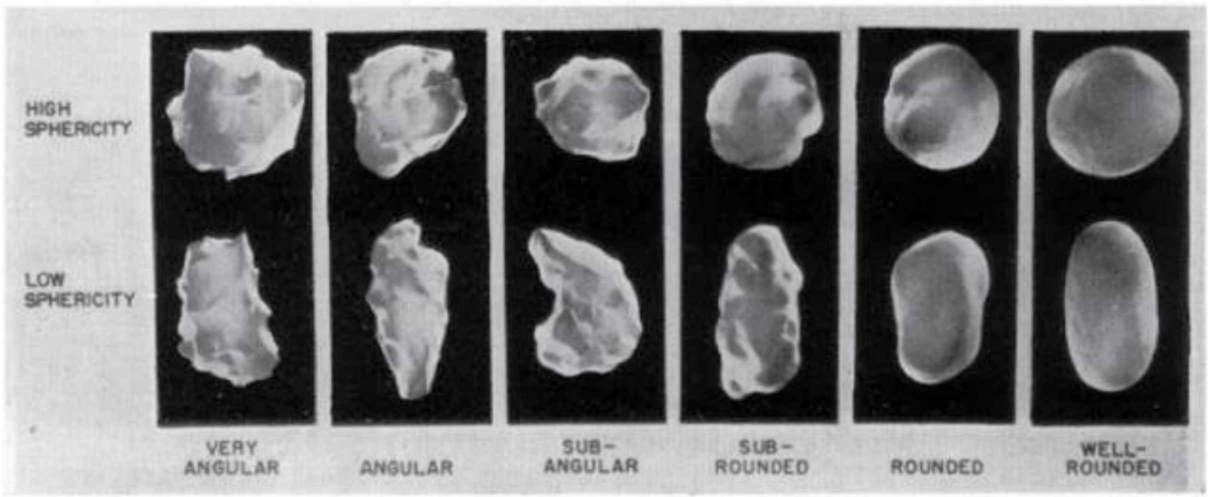

Figure 3.11 Roundness scale (Powers, 1953).

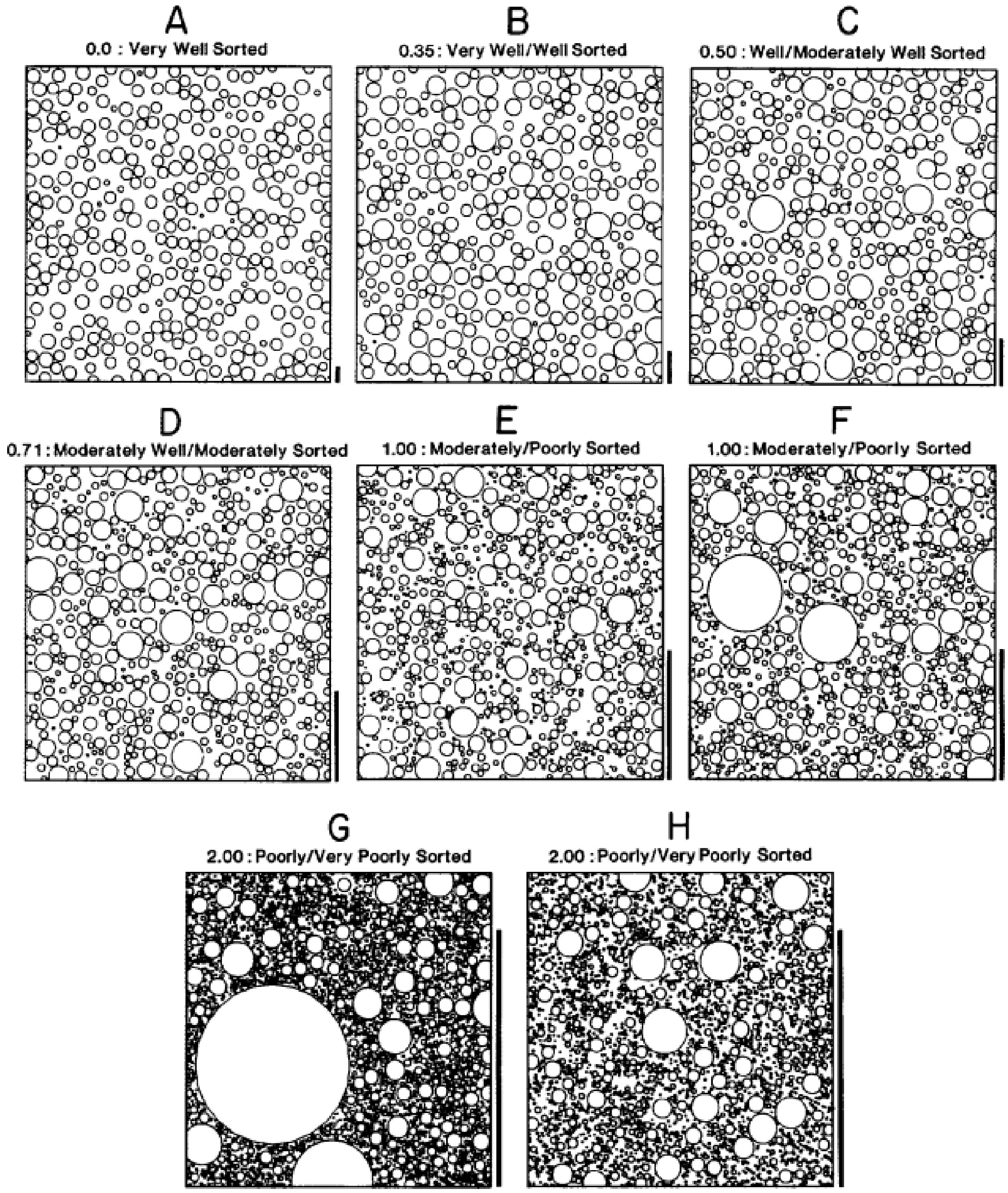

Figure 3.12 Sortedness scale (Longiaru, 1987).

Stop	Formation	Source	Latitude	Longitude
Day 1 04-05-2023				
1.1	Lefkara	Stop 1.3 Guidebook & Geosite 16	35.047311	33.15386
1.2	Pakhna	Stop 1.3 Guidebook & Geosite 16	35.048198	33.153695
1.3	Koronia member	Location found during this study	35.049242	33.152826
1.4	Lefkara and Pakhna	Location found during this study	35.048741	33.149437
1.5	UPB and Lefkara	Location found during this study	35.047803	33.146813
1.6	Pakhna	(Follows, 1990)	35.046874	33.119909
1.7	Pakhna	(Follows, 1990)	35.055168	33.126671
1.8	Pakhna	(Follows, 1990)	35.060863	33.10043
Day 2 05-05-2023				
2.1	Kalavasos	Geosite 15	35.060099	33.100165
2.2	Fanglomerate	Location of Nicosia determined by (McCallum, 1989; McCallum and Robertson, 1995), but defined as Fanglomerate by analyzing field data	35.067071	33.136694
2.3	Nicosia	Stop 1.4 Guidebook	35.024551	33.240705
2.4	Nicosia	(McCallum, 1989; McCallum and Robertson, 1995)	35.02463	33.248095
Day 3 06-05-2023				
3.1	Nicosia	(McCallum, 1989; McCallum and Robertson, 1995)	35.035151	33.224715
3.2	Nicosia/Athalassa/Kakkaristra	Stop 2.2 Guidebook	35.068861	33.22742
Day 4 08-05-2023				
4.1	Nicosia/Athalassa/Kakkaristra	Location found during this study	35.071694	33.229656
4.2	Kakkaristra	Location found during this study	35.04736	33.220882
Day 5 09-05-2023				
5.1	Apalos and Fanglomerate	(Schirmer et al., 2010)	35.089487	33.249079
5.2	Kakkaristra	(Schirmer et al., 2010)	35.072768	33.230046
5.3	Fanglomerate	Stop 2.3a Guidebook	35.126943	33.012939
5.4	Fanglomerate	(Poole and Robertson, 1998)	35.102745	33.075623
Day 6 10-05-2023				
6.1	Apalos and Fanglomerate	(Schirmer et al., 2010) & Geological Survey Department Cyprus	35.089513	33.249781
6.2	Fanglomerate	Geological Survey Department Cyprus	35.1001	33.240435
6.3	Fanglomerate	Geological Survey Department Cyprus	35.10165 35.089513 35.074462	33.208661 33.249781 33.198855
6.4	Fanglomerate or Holocene	Geological Survey Department Cyprus	35.07329	33.301912
Day 7 11-05-2023 → Search for serpentinite for Master thesis D. Schutte				
7.1	Dunite, pyroxenite and lherzolite	Stop 4.4 Guidebook	34.929595	32.925477
7.2	Asbestos mine	Stop 4.3 Guidebook & Geosite 11	34.932808	32.913146
7.3	Harzburgite serpentinite (north of Arakapas Fault Zone)	Start Artemis trial	34.933184	32.871453
7.4	Obduction contact	Stop 5.4 Guidebook	34.771257	32.516202
7.5	Harzburgite serpentinite (south of Arakapas Fault Zone)	Knowledge A. Beniest	34.776275	33.081947

Day 8 12-05-2023				
8.1	Kakkaristra	Geological map	35.105025	32.972587
8.2	Fanglomerate	Geological map	35.073282	32.999848
8.3	Unknown	Geological map	35.090232	33.005066
8.4	Kakkaristra	Geological map	35.10885	33.028154
Day 9 13-05-2023				
9.1	Nicosia/Athalassa/Kakkaristra	Redo stop 3.2 and 4.1	n/a	n/a
9.2	Apalos or Fanglomerate	Location found during this study	35.047775	33.221515
9.3	Kakkaristra	Geological map	35.003611	33.223641

Table 3.3 Summary of the stops visited during the period of the 2nd till 14th of May 2023 including the formations, sources, latitude and longitude.

3.3 Optical microscopy

During fieldwork, we were not able to identify one rock type within the conglomerates at stops 5.3, 5.4 and 6.3a/b. Distinguishing and identifying minerals was tough with the hand lens, resulting in an inaccurate rock type classification. These rocks were gathered and returned to the Netherlands to produce a thin section of stop 6.3a/b helping to recognize minerals more precise and obtain an accurate rock type. The thin section is observed by using the microscope with 4x to 10x magnification on the Vrije Universiteit Amsterdam. Mineral identification is based on characteristics in both Plane Polarized Light (PPL) and Crossed Polarized Light (XPL). In PPL the color, relief and pleochroism were determined, whereas in XPL the interference color, extinction, twinning and/or structure provide knowledge helping to identify the minerals.

Chapter 4 Results

4.1 Numerical modelling

This section describes the model results with the models for oceanic – oceanic subduction, continent – oceanic subduction and combined continent-oceanic – oceanic subduction. The model results in which the highest strain rate transports onto the overriding plate, localizing a new zone of high strain, Models 2, 4 and 5, are shown in the main text below. The other model results, in which a normal subduction zone geometry forms, including the viscous forebulge, the subduction trench and the collisional high, and the region behind the collision high deforms (fig. 3.9), can be found in Appendix A (A.1 to A.9).

4.1.1 Oceanic lithosphere models

In Model 1 (table A.1), the highest strain rate is localized on the plate contact during the entire run time of the model (fig. 3, 6, 9, 12 and 15, Appendix A.1). Deformation and topography are concentrated at the collision zone. The topography of the collisional high increases to 8 km after 4 to 6 Myr (fig. 5 and 8, Appendix A.1), followed by subsidence and a topographic high that is 5.8 km high after 10 Myr (fig. 14, Appendix A.1). Over time, the region behind the collisional high subsided 0.8 km and is bounded relative by 0.8 km high hills with respect to the subsided area but did not change in absolute elevation compared to the reference depth of 0 km (fig. 14, Appendix A.1). At the collision zone, the trench deepens to 12 km in the first 8 Myr (fig. 11, Appendix A.1). After 10 Myr, the trench has a depth of 8.5 km (fig. 14, Appendix A.1). The topography of the forebulge on the subducting plate reaches 1.5 km after 10 Myr (fig. 14, Appendix A.1).

In Model 2 (table A.2), the highest strain rate is localized on the plate contact during the first 8 Myr (fig. 3, 6, 9 and 12, Appendix A.2). During the last 2 Myr, the highest strain rate is transported 200 km away from the trench, in the overriding plate (fig. 4.1). During the first 8 Myr, topographic heights mainly concentrate in the collision zone with 1.5 km subsidence in the region directly behind the collision high bounded by a 1.5 km high hill, subsided area and 1.0 km high hill in the hinterland (fig. 11, Appendix A.2). During the last 2 Myr both the collisional high and its hinterland deform (fig. 4.3). The topography of the collisional high increases to 7.5 km after 6 Myr (fig. 8, Appendix A.2), followed by subsidence resulting in a 3.5 km high collisional high after 10 Myr (fig. 4.3). After 10 Myr, the trench deepened to 8.0 km depth and the forebulge heightened 2.5 km high (fig. 4.3). Furthermore, during the first 8 Myr, a 1.0 km deep subsided area formed in the region behind the collisional high, which is bounded by 1.5 km high hills (fig. 11, Appendix A.2). After 10 Myr, the change of location for the highest strain rate leads to a 3.0 km high forebulge, a 4.0 km deep trench and a 2.8 km high collisional high with a depression behind the collisional high (fig. 4.3).

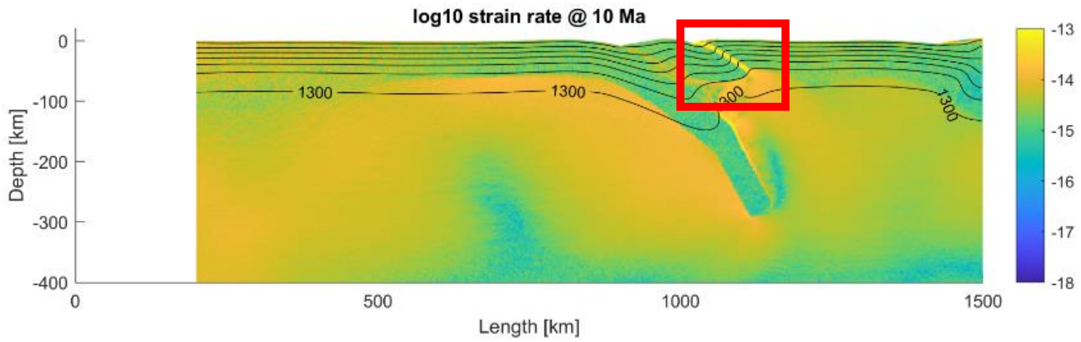

Figure 4.1 Strain rate of Model 2 after 10 Myr.

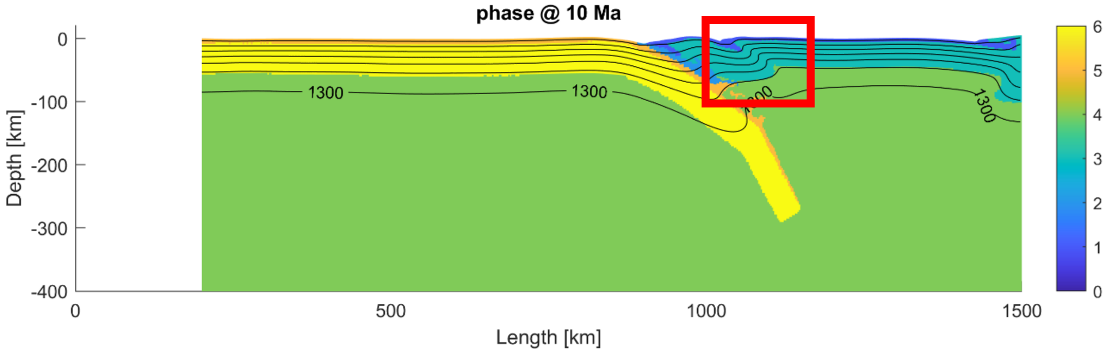

Figure 4.2 Phases of Model 2 after 10 Myr.

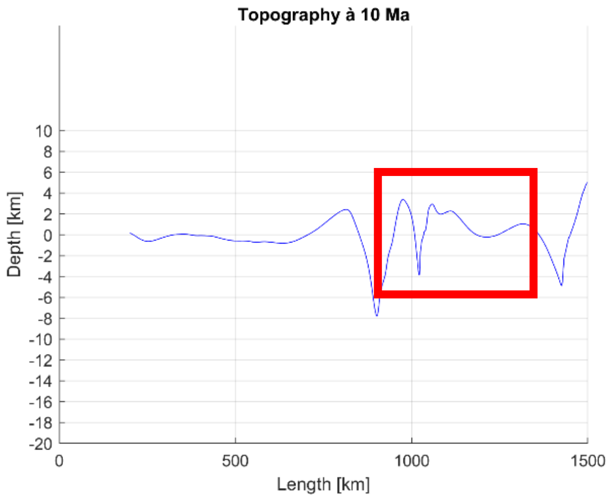

Figure 4.3 Topography of Model 2 after 10 Myr.

In Model 3 (table A.3), the highest strain rate is localized on the plate contact during the first 6 Myr (fig. 3, 6 and 9, Appendix A.3). During the first 1.5 Myr, the topography of the collisional high reaches 5 km, whereas the trench is 6 km deep at the collision zone and the forebulge on the subducting plate becomes 8 km high (fig. 2, Appendix A.3). After 6 Myr, the topography of the collisional high becomes 8 km high, 10 km deep in the trench and 2 km high in the forebulge (fig. 8, Appendix A.3). Behind the collisional high a depression develops. Between 8 to 10 Myr, the strain rate is almost constant throughout the model, with -13 s^{-1} for the plate contact and mainly -13.5 to -13 s^{-1} for the rest of the model box with some areas of -15 s^{-1} (fig. 12 and 15, Appendix A.3). This results in major topography in the hinterland of both the overriding and subducting plates with 4 km high hills separated by 3 km deep valleys (fig. 14, Appendix A.3). After 10 Myr, the subduction system consists of an 8 km high collisional high, an 8 km deep trench and a 4.8 km high forebulge (fig. 14, Appendix A.3).

In Model 4 (table A.4), the highest strain rate is localized on the plate contact during the first 9 Myr (fig. 3, 6, 9 and 12, Appendix A.4). During the first 6 Myr, the collisional high heightens to 8.5 km (fig. 8, Appendix A.4), followed by subsidence resulting in a 5 km high collisional high after 10 Myr (fig. 14, Appendix A.4). The trench deepens to 8.2 km during the first 8 Myr (fig. 11, Appendix A.4) and becomes 6 km deep after 10 Myr (fig. 14, Appendix A.4). During the first 8 Myr, a relatively 3.5 km depression develops behind the collisional high (fig. 11, Appendix A.4). Over time, the forebulge on the subducting plate heightens 4.5 km (fig. 14, Appendix A.4). The geometry of the subduction zone varies over time. After 9.5 Myr, the highest strain rate is transported 200 km onto the overriding plate (fig. 4.4). This second location of strain localization consists of a 1.5 km high forebulge, a 2.0 km deep trench and a 3.8 km high collisional high (fig. 4.6). In this geometry, no clear depression is observed behind the collisional high. During the last 0.5 Myr, the strain rate is almost constant throughout the model, varying between -14 – -13 s^{-1} (fig. 15, Appendix A.4) changing the geometry. Consequently, the initiation of the newly located strain localization point vanished (fig. 14, Appendix A.4).

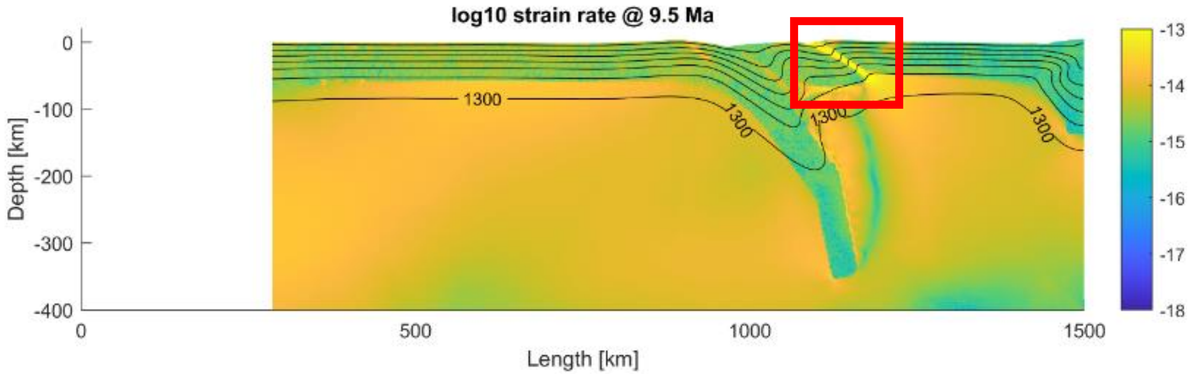

Figure 4.4 Strain rate of Model 4 after 9.5 Myr.

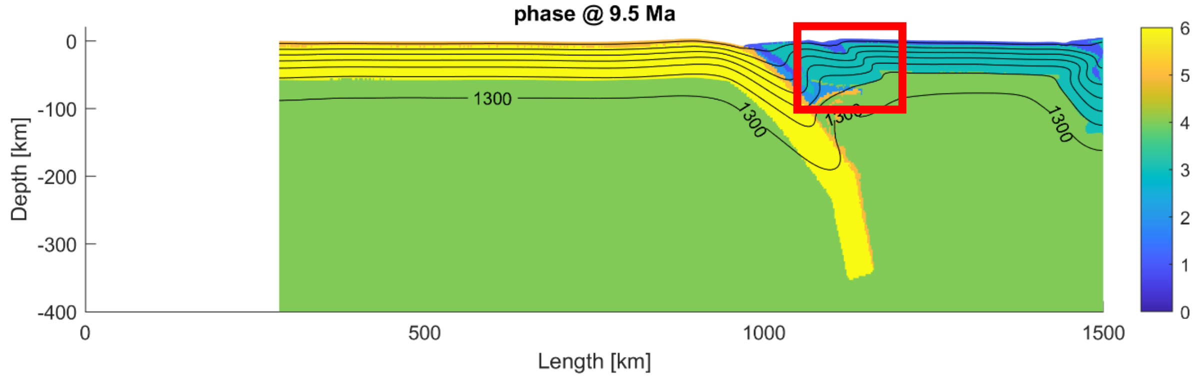

Figure 4.5 Phases of Model 4 after 9.5 Myr.

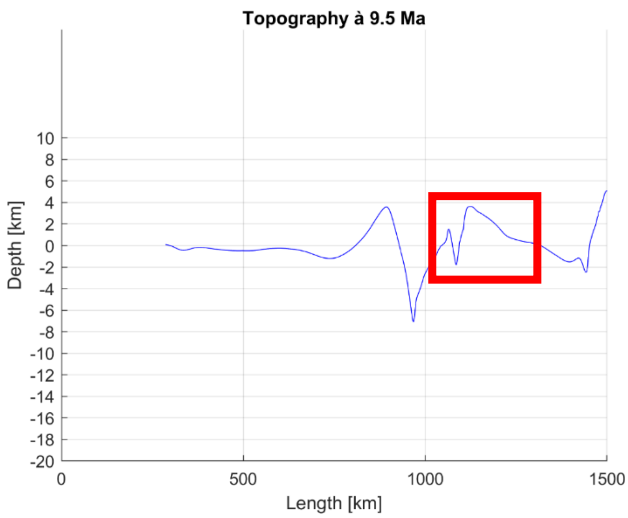

Figure 4.6 Topography of Model 4 after 9.5 Myr.

4.1.2 Continental lithosphere model

In Model 5 (table A.5), strain rate localizes on the plate contact until 5 Myr (fig. 3, 6 and 9, Appendix A.5). Instead of subduction actually occurring, the subducting plate starts flowing (fig. 1, Appendix A.5). Topography develops mainly at the subduction contact and the collisional zone during the first 3 Myr (fig. 5, Appendix A.5). In this period, a 7.0 km high collisional high, a 4.5 km deep trench and a 1.0 km high forebulge formed. Between 3 to 5 Myr, the subducting slab starts to flow and delaminate (fig. 4 and 7, Appendix A.5), along with topography formation in the region behind the collisional high (fig. 8, Appendix A.5). After 10 Myr, a 6.5 km high collisional high, a 5.0 km deep trench and a 1.0 km high forebulge formed (fig. 4.9). Furthermore, at 10 Myr the highest strain rate has moved 400 km into the overriding plate (fig. 4.7). This new zone of strain localization consists of a 1.5 km high forebulge, a 9.0 km deep trench and a 1.5 km high collisional high (fig. 4.9).

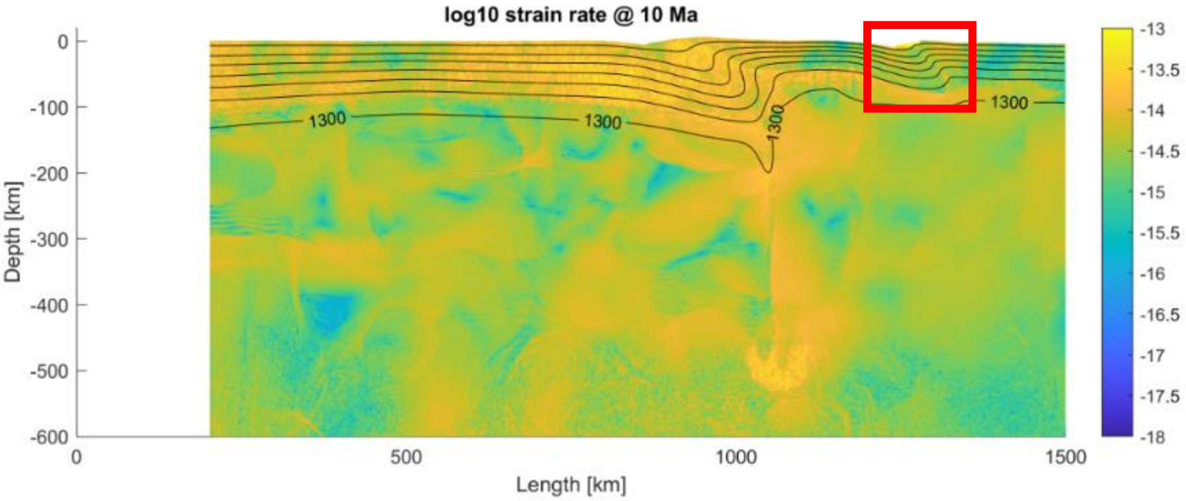

Figure 4.7 Strain rate of Model 5 after 10 Myr.

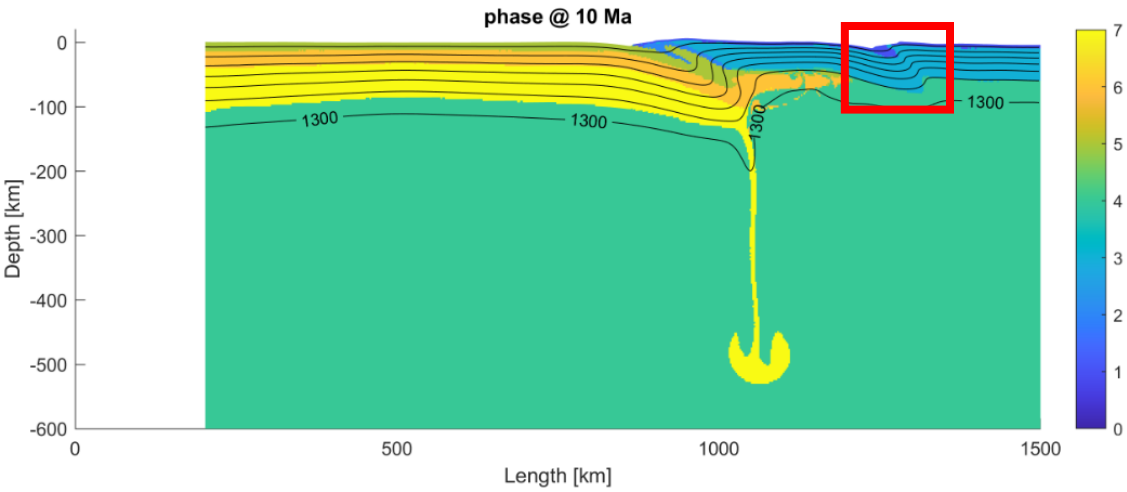

Figure 4.8 Phases of Model 5 after 10 Myr.

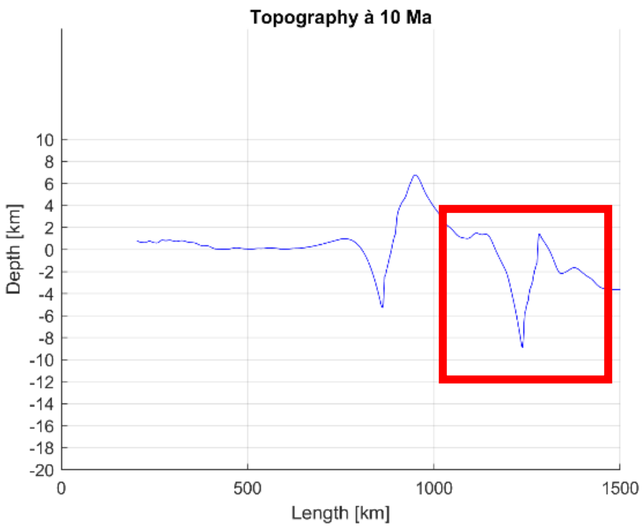

Figure 4.9 Topography of Model 5 after 10 Myr.

4.1.3 Ocean-continental lithosphere models

In Model 6 (table A.6), the highest strain rate is localized on the plate contact throughout the model run (fig. 3, 6, 9, 12 and 15, Appendix A.6). Topography develops mainly in the collision zone, with the collisional high reaching 8.5 km after 6 Myr (fig. 8, Appendix A.6). This is followed by subsidence resulting in a 7.5 km high collisional high after 10 Myr (fig. 14, Appendix A.6). Over time, the region behind the collisional high subsided 2.0 km, the trench deepens to 6.0 km and the forebulge reaches 2.0 km (fig. 14, Appendix A.6). After 10 Myr, the oceanic lithospheric part of the subducting plate starts to break off (fig. 13, Appendix A.6).

In Model 7 (table A.7), the highest strain rate is localized on the plate contact throughout the model run (fig. 3, 6, 9, 12 and 15, Appendix A.7). Topography forms mainly on the plate contact. During the first 4 Myr, the collisional high reaches 9.0 km (fig. 5, Appendix A.7), followed by subsidence and broadening of the collisional high to 100 km wide with an altitude of 7.5 km after 10 Myr (fig. 14, Appendix A.7). Over time, the domain directly behind the collisional high subsides 1.0 km and deepens up to a 3.0 km deep depression with increasing distance from the collisional high. The trench deepens to 5.5 km depth and broadens to 200 km width. The forebulge on the subducting plate reaches 3.5 km (fig. 14, Appendix A.7). After 10 Myr, the oceanic lithospheric part of the subducting plate starts to break off (fig. 13, Appendix A.7).

In Model 8 (table A.8), the highest strain rate is localized on the plate contact throughout the model run (fig. 3, 6, 9, 12 and 15, Appendix A.8). During the first 4 Myr, the collisional high heightens to 9.0 km and the trench deepens to 6.0 km (fig. 5, Appendix A.8). From 4 to 10 Myr, the collisional high subsides to 7.0 km high and the trench becomes 5.0 km deep (fig. 14, Appendix A.8). Over time, the forebulge on the subducting plate heightens 1.5 km. After 6 Myr, topography develops in the region behind the collisional high in the form of a 6.5 km deep valley (fig. 8, Appendix A.8). After 8 Myr, the oceanic lithospheric part of the subducting plate starts to break off (fig. 10, Appendix A.8) and almost finishes rupturing after 10 Myr (fig. 13, Appendix A.8).

In Model 9 (table A.9), the highest strain rate is localized on the plate contact throughout the model run (fig, 3, 6, 9, 12 and 15, Appendix A.9). Topography mainly occurs in the collisional zone. The collisional high heightens to 8.0 km after 4 Myr (fig. 5, Appendix A.9), which is followed by subsidence to a 6.5 km high collisional high along with broadening to a 300 km wide mountain after 10 Myr (fig. 14, Appendix A.9). The depression behind the collisional high subsides 2 km during the first 8 Myr (fig. 11, Appendix A.9). In the last 2 Myr, the topography in this area becomes more curved. Directly behind the collisional high, the topography starts with a 3.0 km deep valley, followed by alternating small hills of relative 2.0 km high, separated by an absolute 3.8 km deep valley with increasing distance from the collisional high. Over time, the trench deepens 6 km and the forebulge heightens 1.5 km (fig. 14, Appendix A.9). The oceanic lithospheric part of the subducting plate starts breaking off after 8 Myr (fig. 10, Appendix A.9) and is completely broken off at 10 Myr (fig. 13, Appendix A.9).

4.2 Fieldwork observations

Observations made in the field are described below for each individual formation.

4.2.1 Observations oceanic crust and mantle sequence

In table 4.1 observations of the oceanic crustal and mantle units are summarized. Within the ophiolitic sequence, some boundaries between the units are not well-defined and can occur at similar depths, indicated by dotted lines. As observed in the outcrop of Geosite 33, the Sheeted Dyke Complex intrudes into the Plagiogranite making the depth of these boundaries debatable. In the field, distinguishing Plagiogranite from the Massive and Layered Gabbro is tough, especially when the rocks are heavily weathered and hornblende is absent. As a result, mineral identification becomes difficult making clast identification challenging when in the field. In addition, between the Plagiogranite and Massive and Layered Gabbro intermingling relationships are observed in the field (Twining, 1996). The Gabbroic Layer is divided into two sublayers. Based on general knowledge about the fractional crystallization order, from shallow to deep, the Massive and Layered Gabbro are the shallowest units in the crust, which is in turn underlain by the deepest unit, the Garnet-Gabbro. Lastly, Lherzolite and Harzburgite contain the same minerals with varying compositions, making a distinction in the field difficult.

	Lithology	**Minerals**	**Characteristics**
Oceanic crust	Upper pillow basalts (UPB) Lower pillow basalts (LPB) Basal group (BG)	Amygdales = Quartz, calcite or zeolite Shine minerals = Iron-sulfides → Yellowish minerals → Pyrite/Chalcopyrite	Very fine texture Vesicles form through pressure release causing gas expansion Brown to elephant-grey weathered Red-oxidized Hydrothermal veins within UPB filled with sulfides
	Sheeted dyke complex (SDC)	Pyroxene Plagioclase Altered minerals → Epidote and chlorite	Chilled margins Dark grey weathered Very fine texture Intrude into each other – Cut off Dolerite/micro-gabbro
	Plagiogranites (PG)	Hornblende Plagioclase/albite	Needle-like minerals Lenses within the SDC Expect: Quartz, mica, K-feldspar Finer texture than gabbro
	Massive gabbro (MG) Layered gabbro (LG)	Plagioclase (10-60%) Pyroxene (40-90%) Amphibole Garnet	Mineral size 1 – 15 mm Pegmatite vein Greenish Plagioclase- or pyroxene-rich If garnet found → Garnet-Gabbro
	Garnet-gabbro	Plagioclase Pyroxene Garnet	Similar as massive or layered gabbro, but containing some garnet
	Pyroxenite	Grey mineral → Pyroxene (> 60%) White flakes → Plagioclase	Rocks are blackish with green Minerals are not visible with the naked eye (< 1 mm) Very fine texture
	Dunites Chromites	Olivine = weathered and oxidized Chromites = black fine-grained Pyroxenes	> 90% olivine Ochre yellow weathered No individual minerals visible, except some serpentinized olivines
Petrological Moho			

Mantle sequence	Lherzolite	Pyroxene → Large blackish Olivine → Green elongated minerals with clear cleavage White flakes → Plagioclase	Dark green blackish rock Mineral size varies (1 – 5 mm) Plagioclase forms within epidote or pyroxene
	Harzburgites	Pyroxene Olivine Magnetite? Spinel?	Extremely serpentinized minerals 90^o cleavage observable in serpentinized pyroxenes Large shiny minerals Dark brown to greyish weathered
	Serpentinite	Chrysotile Antigorite Magnesite	Opaque/silky fibers Glassy/transparent fibers Dusty/dull white, no crystal structure observable

Table 4.1 Observations of the mantle sequence and oceanic crustal rocks.

4.2.2 Boundary Lefkara Formation and Upper Pillow Basalts

The boundary between the Upper Pillow Basalts and the Lefkara Formation is based on measured dip-directions/dips at stops 1.4 and 1.5. The measured dip-directions/dips of the Lefkara Formation (stop 1.4) were 034/42 and 021/53, whereas the measured dip-direction/dip of the Upper Pillow Basalts (stop 1.5) was 026/40. Based on the measured dips, the boundary between the oceanic crustal sequence and first sedimentary deposits is concordant.

4.2.3 Lefkara Formation

The outcrop at stop 1.1 is the Lefkara Formation consisting of white to beige weathered layers alternating in thickness from 1 to 20 cm. The thin layers are deposited during background sedimentation, whereas the thicker layers are deposited in a high energy environment. The matrix of the marly limestones are coarse silt in size, with some foraminifera classified as a wackestone. The rock consists of calcareous carbonate without silica. On the outcrop bioturbation in the form of burrows and crossbedding dipping towards the west were observed. The measured dip-directions/dips are 048/26, 048/10, 034/15 and 020/020.

4.2.4 Pakhna Formation

The outcrop at stop 1.2 is the Pakhna Formation consisting of grey, brown, red and/or ochre yellow weathered layers of a few cm up to 1 meter in thickness. The ochre yellow matrix is silty in size, does not contain silica, but does include chalk- and shell-fragments. The clasts within the matrix are small pebble to large clasts in size, with a matrix-size of medium sand. The rock is classified as a packstone, i.e. clast-bearing, but becomes more a wackestone upward in the formation. The measured dip-directions/dips are 020/13, 032/22 and 015/24.

4.2.4.1 Koronia member

Stop 1.3 is the Koronia member located in the upper part of the Pakhna Formation, consisting of blotchy weathered clasts. The matrix is coarse silt in size with some larger black grains of fine sand size and shell fragments of granular size. The rock-type of this member is classified as a wackestone. The measured dip-direction/dip is 101/43.

4.2.4.2 Boundary Lefkara and Pakhna Formations

The contact between the Lefkara and Pakhna Formations is observed at stop 1.4. The boundary type between these two formations is based on the measured dip-directions/dips. The measurements for the Lefkara Formation were 034/42 and 021/53, whereas the measured dip-direction/dip of the Pakhna Formation was 033/34. Based on the measured dips, the boundary between the Lefkara and Pakhna Formations is an erosive unconformity.

4.2.4.3 Conglomerates of Pakhna Formation

The detailed descriptions of the conglomerates within the Pakhna Formation, i.e. stops 1.6 to 1.8, are summarized in table 4.2. In general, the conglomerates within the Pakhna Formation are matrix-supported and very poorly sorted. The matrix is calcareous, containing low spherical clasts, which are very angular to subrounded originating all from the Pakhna Formation itself, i.e. monomict, which vary in size from < 1 cm up to 2 meters. The clasts consist of shells, e.g. bivalves, gastropods, reef-structures and coral fragments.

Stop	1.6	1.7	1.8
Matrix	Matrix-supported	Matrix-supported – More matrix than stop 1.6	Matrix-supported
Roundness/angularity	Very angular	Angular to subrounded	Very angular
Sphericity	Low	Low	Low
Sorted	Very poorly sorted	Very poorly sorted	Very poorly sorted
Category	G	H	G
Clast size	< 1 cm – 2 m	< 1 cm – 1 m	< 1 cm – 1 m
Rock-type	Calcareous with forams	Yellowish chalk	n/a
Grain-size matrix	Very fine sand to silt	Fine silt	n/a
Dip-direction/dip	n/a	075/22	n/a
Travel distance	Small	Larger than 1.6	Between 1.6 and 1.7
Monomict/polymict	Monomict	Monomict	Monomict
Clasts			
Fossils	Shells - Bivalve Gastropod Reef-structures Coral	Shells - bivalve Coral Reef-structures	Coral-fragments – Corn-cop shaped
Rock-type	Packstone 70% Wackestone 30%	Packstone 60% Wackestone 40% Grainstone - Ooids	Packstone 70% Wackestone 30%
Specifics	Some clasts are recrystallized/dolomitized	Some clasts are recrystallized	n/a

Table 4.2 Observations of the conglomerates within the Pakhna Formation, May 2023.

4.2.5 Kalavasos Formation

At stop 2.1 the Kalavasos Formation crops out. The description is based on observations made in the field and information given by this Geological Site, i.e. Geosite 15. The formation is divided in two different members. Firstly, gypsum crystallizes in a certain structure, known as selenite. The transparent, grey, beige to white crystals in this structure vary in size from 1 to 15 cm. The second member, known as the Marmara member, is a finely laminated gypsum, consisting of 1 to 3 mm thick layers. The grey to beige anhydrite crystals are finer grained than the crystals in the selenite structure.

4.2.6 Nicosia Formation

At stops 2.3 and 3.2a, the Nicosia Formation is observed. The formation consists of fining upward alternating layers with, i.e. conglomerates, and without clasts (fig. 4.10). The layers without clasts are finely laminated (1 to 10 mm thick) and intercalated with 1 to 2 cm thick white layers which return 7 to 8 times within the outcrop at stop 3.2a, indicating a cyclicity during deposition. The matrix of these layers is well sorted and fine to coarse silt in size. The weathering and/or oxidizing color is brown to beige with a grey original color, i.e. intern color. The measured dip-directions/dips are 016/18 and 342/18.

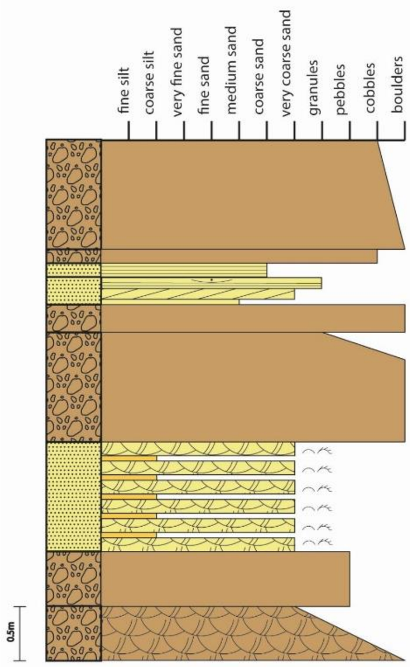

Figure 4.10 The created log of the Nicosia Formation, stop 2.3a/b, made by D. Schutte.

4.2.6.1 Conglomerates within the Nicosia Formation

The outcrop descriptions of the conglomerates within the Nicosia Formation, i.e. stops 2.3, 2.4 and 3.1, are summarized in table 4.3, with individual detailed clast descriptions in table 4.4. In general, the conglomerates within the Nicosia Formation are matrix-supported and moderately well to very poorly sorted. The chalk matrix is fine sand to coarse silt in size, containing lithic fragments, i.e. mafic material, and fossils, e.g. gastropod and shell fragments. The clasts have a low sphericity, are angular to rounded and originate from various formations, i.e. polymict, which vary in size from < 1 cm up to 60 cm. The clasts originate from the Pakhna (15 – 55%) and Lefkara (2 – 25%) Formations of the sedimentary cover and from the Umbers (0 – 4%), Upper and Lower Pillow Basalts and Basal Group (10 – 60%), Sheeted Dyke Complex (0 – 33%) and Plagiogranite (0 – 1%) of the oceanic crust.

Stop	2.3a	2.3b	2.4	3.1
Matrix	Matrix-supported	Matrix-supported	Matrix-supported	Matrix-supported
Roundness/angularity	Angular (Pakhna) to subrounded (mafic material)	Angular (Pakhna) to subrounded (mafic material)	Subangular to rounded	Angular to rounded
Sorted	Poorly/Very poorly sorted	Moderately well – poorly sorted	Moderately well – poorly sorted	Poorly – very poorly sorted
Category	G	D & E	D & E	H
Sphericity	Low	Low	Low	Low
Clast size	5 mm – 60 cm	1 – 30 cm	< 1 – 30 cm	0.5 mm – 50 cm
Rock-type	n/a	n/a	n/a	n/a
Grain-size matrix	Fine sand to coarse silt → Bad sorted	Fine sand	Coarse silt to medium sand	Fine sand
Dip-direction/dip	n/a	028/09	068/24	
Monomict/polymict	Polymict	Polymict	Polymict	Polymict
Specifics	On top of the outcrop > 3 m size clasts of the Pakhna Formation	Two times fining upward with local disruptions of coarse clasts	Fossils in matrix: Gastropod, tapped bivalve and shell fragments within matrix Alternations in amount of clasts Channeling caused cutoff layers	Clasts have no orientation Lithic fragments (5%) within matrix → Mafic material Chalk matrix (95%)

Table 4.3 Outcrop observations of the conglomerates within the Nicosia Formation, May 2023.

Formation	Pakhna	Lefkara	UPB + LPB + BG	SDC	PG	Other
Stop 2.3a						
Size	1 cm – > 1 m	< 10 cm	n/a	< 0,5 – 30 cm	n/a	n/a
Percentage	55%	2%	10%	33%	n/a	n/a
Characteristics	Reef-structures Recrystallized burrow Recrystallized calcite Packstone Coral visible within the clasts	White Sticks to your tongue Angular	Vesicles (< 1 – 5 mm) Brown-red oxidized Very fine texture Amygdales → Filled with epidote and quarts Subangular	Micro-gabbro greenish → Epidotized Micro-gabbro greyish Very fine to fine texture (< 1 mm; visible with naked eye) Rim with more plagioclase → Chilled margin? Albite	n/a	n/a

				Altered pyroxene Oxide-mineral Subangular to rounded		
Stop 2.3b						
Size	5 - < 40 cm	2 – 20 cm	1 – 25 cm	n/a	n/a	n/a
Percentage	25%	25%	50%	n/a	n/a	n/a
Characteristics	White Angular Reef/coral structure Grainstone Recrystallized	White Silty Sticks to your tongue Rounded	Vesicles/amygdales Fine texture Dark rusty weathered Subrounded-rounded Gabbro vein	n/a	n/a	n/a
Stop 2.4						
Size	5 – 30 cm	< 5 cm	1 mm – 30 cm	n/a	n/a	n/a
Percentage	20%	10%	60%	5%	n/a	5%
Characteristics	Grainstone Packstone Subangular Calcite crystals	White Sticks to your tongue Subrounded	Vesicles & amygdales Greenish-greyish weathered Fine texture Subrounded to rounded	Fine texture gabbro with basalt or micro-gabbro vein	n/a	Alveolina wackestone < 20% alveolina in matrix Conchoidal fracturing Greyish brown Small holes **Lefkara**
Stop 3.1						
Size	1 – 20 cm	1 – 20 cm	0.5 – 10 cm	< 0.5 – 15 cm	3 cm	< 5 cm
Percentage	15%	5%	45%	30%	1%	4%
Characteristics	White/beige mud- or wackestone Angular – subangular	Pink/white brecciated mud- or wackestone Alveolina Angular – subangular	Vesicles & amygdales → Oxidized Greenish oxidized → Epidote Fine to very fine texture Subrounded – rounded	Fine texture → Micro-gabbro Very fine texture → Basalt Grey color Plagioclase-rich rim → Chilled margin? Angular – subangular	Felsic Pyroxene Plagioclase Some needle-like minerals → Hornblende (5%) Heavily weathered Subrounded – rounded	Dark rusty weathered (Chalco)pyrite Heavy Angular **Umber**

Table 4.4 Observations of the clasts in the conglomerates within the Nicosia Formation, May 2023.

4.2.6.2 Boundary Nicosia and Athalassa Formations

The boundary between the Nicosia and Athalassa Formations is an unconformity. Within the outcrop at stop 3.2a/b, the massive banks of the Athalassa Formation cuts off the layers of the Nicosia Formation (fig. 4.11). Additionally, the matrix-size changes abruptly from silty to very fine sand.

Figure 4.11 The unconformity between the Nicosia and Athalassa Formation at stop 3.2. Source: Cyprus Geology and Geochemistry field excursion guidebook.

4.2.7 Athalassa Formation

The Athalassa Formation crops out at stop 3.2b. The formation starts with brown weathered massive banks up to 3 meters thick. The silica-rich rock contains quartz. The matrix is well sorted and contains some feldspar minerals. Within the matrix, shell fragments and bivalves (6 cm) are observed. More upward into the Athalassa Formation, the layers become thinner varying between 2 to 15 cm in size. The orange greyish weathered layers contain bioturbation in the form of burrows. The matrix is fine silt in size containing some shell fragments. The measured dip-directions/dips are 040/21, 037/37 and 027/10.

4.2.8 Kakkaristra Formation

The Kakkaristra Formation consists of conglomerates with sand lenses. The matrix of the sand lenses are medium to fine sand in size, and grey colored with beige weathering. The sand lenses' dip direction/dips at stop 3.2c are 036/07 and 045/15.

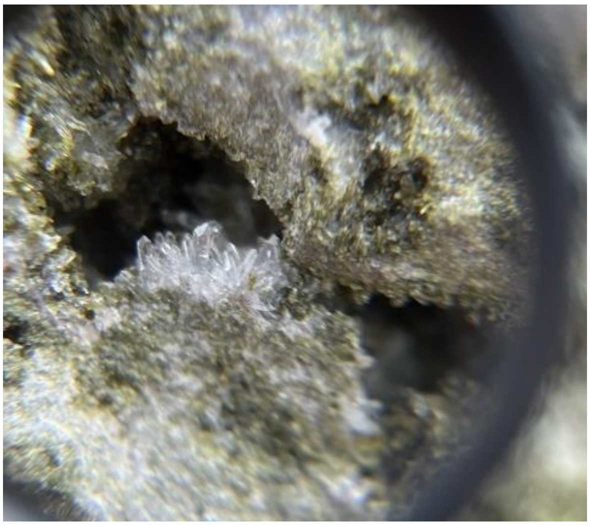

Figure 4.12 Euhedral quartz crystals observed at stop 4.1 zoomed 10x with the hand-lens.

The outcrop descriptions of the conglomerates within the Kakkaristra Formation, i.e. stops 3.2c, 4.1, 4.2, 5.2a/b, 8.1, 8.4 and 9.3, are summarized in table 4.5, with individual detailed clast descriptions in table 4.6. In general, the conglomerates within the Kakkaristra Formation are matrix-supported and moderately well to very poorly sorted. The matrix is fine sand to fine silt in size, containing lithic fragments, i.e. mafic material. In most outcrops, the flattened clast are hydrodynamically oriented. The clasts have a low sphericity, are angular to rounded and originate from various units of the oceanic crustal sequence, i.e. polymict, which vary in size from 1 mm up to 70 cm. The clasts originate from the Umbers (1 – 5%), Upper and Lower Pillow Basalts and Basal Group (10 – 64%), Sheeted Dyke Complex (14 – 80%), Plagiogranite (1 – 20%), Massive and Layered Gabbro (2 – 40%) and Garnet-gabbro (0 – 5%).

The Kakkaristra Formation is also found at stop 9.3, closest located to the Troodos Ophiolite (fig. 3.10). In this stop, there is only 10% Upper and Lower Pillow Basalts and Basal Group found, whereas the Massive and Layered Gabbro cover 24%, which deviates from the general description of other Kakkaristra sites.

Stop	3.2c	4.1	4.2	5.2a	5.2b	8.1	8.4	9.3
Matrix	Matrix-supported	Matrix-supported	Matrix-supported	Matrix-supported	Matrix-supported	Matrix-supported	Matrix-supported	Matrix-supported
Roundness/angularity	Subangular to rounded	Angular to rounded	Subangular to rounded	Subangular to rounded	Subangular to subrounded	Subangular to rounded	Subangular to rounded	Subangular (90%) to rounded (10%)
Sorted	Very poorly sorted	Very poorly sorted	Very poorly sorted	Moderately to poorly sorted	Poorly to very poorly sorted	Poorly to very poorly sorted	Moderately to moderately well sorted	Poorly to very poorly sorted
Category	H	G	G	F	G	G	D	G
Sphericity	Low	Low	Low	Low	Low	Low	Low	Low
Clast size	2 mm – 50 cm	2 mm – 50 cm	1 – 40 cm	1 mm – 70 cm	2 mm – 40 cm	2 mm – 40 cm	2 mm – 20 cm	2 mm – 45 cm
Rock-type	n/a	n/a	n/a	n/a	n/a	n/a	n/a	n/a
Grain-size matrix	Fine to very fine sand	Very fine sand to coarse silt	Very fine sand	Coarse to fine silt	Very fine sand	Fine sand to coarse silt	Coarse to fine silt	Very fine sand
Dip-direction/dip	n/a	029/07	**Not determined due to thunder**	271/23	n/a	n/a	n/a	n/a
Monomict/polymict	Polymict	Polymict	Polymict	Polymict	Polymict	Polymict	Polymict	Polymict
Specifics	Minimal orientation of the clasts → Subhorizontally aligned 99% volcanic clasts 1% umber	Flattened pebbles are subhorizontally aligned A conglomerate layer of 50 cm thick within the sands of Kakkaristra Fm. Surrounding sands are layered → 2 mm thick Matrix scratches in hammer → Quartz	Most clasts have no orientation. The flattened pebbles are subhorizontally aligned	Flattened pebbles (20%) which are subhorizontally aligned	Flattened clasts are hydrodynamically oriented	Outcrop → Red weathered Lithic fragments within the matrix → Mafic material Flattened clasts are subhorizontally aligned	Outcrop consists of contact between Nicosia and Kakkaristra Formation → Unconformity Bedding alternates between well hydrodynamically deposited and not hydrodynamically deposited/mass deposit	Clasts have no orientation → Chaotic Lithic fragments within the matrix → Mafic material Deposited directly on the pillow basalts

Table 4.5 Outcrop observations of the conglomerates within the Kakkaristra Formation, May 2023.

Formation	Umber	UPB + LPB + BG	SDC	PG	LG + MG	Other
Stop 3.2c						
Size	7 cm	1 – 50 cm	< 10 cm	5 – 15 cm	15 – 20 cm	n/a
Percentage	1%	64%	20%	5%	10%	n/a
Characteristics	Dark rusty weathered Quartz Pyrite/chalcopyrite Subangular	Vesicles & amygdales Matrix = fine texture Greenish & reddish weathered Epidotized Radial weathering Subrounded to rounded	Micro-gabbro & basalt Matrix = fine to very fine texture Elephant grey Greenish = Epidotized Subrounded	Feldspar 70% Green minerals = Epidote Oxide-minerals Heavily weathered → Breaks apart easily Subrounded	Plagioclase (40%) Pyroxene (60%) Subrounded Grainsize matrix < 1 mm	n/a
Stop 4.1						
Size	1.5 – 7 cm	2 – 50 cm	1 – 10 cm	n/a	< 30 cm	15 cm
Percentage	1%	40%	14%	n/a	40%	5%
Characteristics	Yellowish gold minerals → Chalcopyrite Conchoidal fracturing → Si-rich (Quartz) Rusty weathered Matrix = yellowish orange weathered Black minerals → Volcanic glass Subangular - subrounded	Vesicles & amygdales Red to green-greyish weathered Very fine texture Subangular - rounded	Fine texture = micro-gabbro Very fine texture = basalt Matrix & minerals < 1 mm Plagioclase Pyroxene Varying weathering degree Grey weathered Rounded to subrounded	n/a	Coarse texture Plagioclase (50%) Pyroxene (50%) Heavily weathered → Breaks apart easily Angular – subrounded	Highly epidotized Epidote crystals → < 1 cm Holes filled with euhedral quartz minerals (fig. 4.12) Quartz Subrounded **Garnet-gabbro**
Stop 4.2						
Size	< 20 cm	< 15 cm	3 – 40 cm	n/a	< 20 cm	n/a
Percentage	3%	20%	70%	n/a	7%	n/a
Characteristics	Euhedral crystals → Quartz Dark rusty weathered Amorph milky crystals with low density	Vesicles Amygdales → Weathered or filled with copper Dark rusty weathered	Fine texture → Micro-gabbro Very fine texture → Basalt Plagioclase & pyroxene < 1 mm Elephant-grey weathered	n/a	Plagioclase 45% Pyroxene 55% Coarse texture (> 1 mm) Subangular-subrounded	n/a

	Conchoidal fracturing Subangular – subrounded	Very fine texture Greenish weathered → Epidotized Subangular – subrounded	Subangular – rounded			
Stop 5.2a						
Size	5 cm	8 cm	2 mm – 20 cm	n/a	2 – 8 cm	n/a
Percentage	3%	10%	80%	n/a	6%	1%
Characteristics	Red-orange color Dark rusty weathered (Chalco)pyrite Subangular	Vesicles & amygdales Very fine texture Red-greyish weathered Subangular	Greenish weathered → Highly epidotized Brown-greyish weathered Fine texture → Micro-gabbro Very fine texture → Basalt Plagioclase (40 – 60%) Pyroxene (40 – 60%) Subrounded – rounded	n/a	Varying weathering degree Blotchy weathered on the outside Coarse texture Minerals > 1 mm Plagioclase (40%) Pyroxene (60%) Subrounded	Black color Very fine texture Heavy Rusty weathering White flakes
Stop 5.2b						
Size	n/a	n/a	n/a	n/a	n/a	n/a
Percentage	5%	15%	75%	1%	4%	n/a
Characteristics	n/a	n/a	n/a	n/a	n/a	n/a
Stop 8.1						
Size	12 cm	< 10 cm	2 mm – 40 cm	< 25 cm	< 10 cm	n/a
Percentage	3%	15%	60%	20%	2%	n/a
Characteristics	Dark rusty weathered Red-orange colored Silicified material Oxide-minerals Quartz (Chalco)pyrite Subangular	Vesicles & amygdales Very fine texture Reddish weathering → Oxidized Subrounded – rounded	Fine texture → Micro-gabbro Very fine texture → Basalt Green greyish colored White to reddish weathering Subrounded – rounded	Needle-like minerals → Hornblende Fine to coarse texture Felsic White to beige colored Plagioclase Pyroxene Quartz Subrounded	Coarse texture Minerals > 1 mm Plagioclase (50%) Pyroxene (50%) Crumbly weathering Subrounded	n/a

Stop 8.4						
Size	< 5 cm	< 5 cm	2 mm – 20 cm	15 cm	< 7 cm	< 5 cm
Percentage	2%	15%	70%	5%	5%	3%
Characteristics	Rusty weathering Red colored Subangular	Vesicles Rusty amygdales Subrounded – rounded	Fine & very fine textures Subangular – rounded	Needle-like minerals → Hornblende (> 1 mm) Rounded	Coarse texture Heavily weathered Subangular – rounded	Greenish → Completely epidotized Fine texture Shiny minerals Subrounded
Stop 9.3						
Size	2 cm	< 10 cm	2 mm – 45 cm	n/a	< 10 cm	n/a
Percentage	1%	10%	65%	n/a	24%	n/a
Characteristics	White greenish colored → Epidotized Subangular	Heavily and crumbly weathered Brown yellowish oxidized Fine texture due to weathering → Becomes sandstone like Rounded	Fine texture → Micro-gabbro Onion weathering Minerals < 1 mm Subangular – rounded	Is expected because its shallower in the oceanic crustal sequence (table 4.1) but due to weathering not found	Heavily and crumbly weathered → Breaks apart easily Minerals > 1 mm Subangular – rounded	n/a

Table 4.6 Observations of the clasts in the conglomerates within the Kakkaristra Formation, May 2023.

4.2.9 Apalos Formation

The Apalos and Fanglomerate Formations are observed in the Vlokkariá cliff, which is a manmade cliff (Schirmer et al., 2010), at stops 5.1a and 6.1. The boundary between the two formations is a discordancy or unconformity. The Apalos Formation shows cyclicity, which cycles starting with gravel alternating and interfingering silty beds with a fining upward trend. The matrix of the silty beds are coarse silt in size. The gravels in the gravel-rich layers are 1 mm to 10 cm in size and vary in quantity. The layers are brown to white weathered with some oxidation of manganese. Within the outcrop, massive bioturbation, e.g. Thallasinoides, up to 10 cm long and 4 cm in diameter are observed, whereas in the silty layers the bioturbation is minor.

4.2.10 Fanglomerate Formation

The outcrop descriptions of the conglomerates within the Fanglomerate Formation, i.e. stops 2.2, 5.1b, 5.3, 5.4, 6.2, 6.3 and 8.2, are summarized in table 4.7, with individual detailed clast descriptions in table 4.8. In general, the conglomerates within the Fanglomerate Formation are mainly matrix-supported with two exceptions at stops 2.2 and 5.1b in which matrix- and clast-supported alternates. The matrix is coarse silt to medium sand in size, containing lithic fragments, i.e. mafic material. The clasts within the matrix have a low sphericity, are well to poorly sorted, vary in size from 1 mm up to 70 cm and are from various units of the oceanic crustal sequence, i.e. polymict. In most outcrops, the (flattened) clasts are hydrodynamically oriented. The clasts originate from the Pakhna (0 – 8%) and Lefkara (0 – 2%) Formations of the sedimentary cover and the Umbers (0 – 10%), Upper and Lower Pillow Basalts and Basal Group (16 – 40%), Sheeted Dyke Complex (37 – >80%), Plagiogranite (0 – 5%) and Massive and Layered Gabbro (0 – 10%).

Stop	2.2	5.1b	5.3	5.4	6.2	6.3a/b	8.2
Matrix	Variation in clast- and matrix-supported	Variation in clast-supported (20%) and matrix-supported (80%)	Matrix-supported	Matrix-supported	Matrix-supported	Matrix-supported	Matrix-supported
Roundness/angularity	Subangular to subrounded	Subangular to rounded	Angular to rounded	Subangular to rounded	Subangular to rounded	Subangular to rounded	Subangular to subrounded
Sorted	Poorly sorted	Moderately well sorted	Poorly sorted	Moderately sorted	Moderately to moderately well sorted	Poorly sorted	Moderately well to well sorted
Category	G	D	G	F	D	G	C
Sphericity	Low to high	Low	Low	Low	Low	Low	Low
Clast size	5 mm – 40 cm	2 mm – 15 cm	1 mm – 30 cm	2 mm – 30 cm	2 mm – 40 cm	2 mm – 70 cm	2 mm – 30 cm
Rock-type	n/a	n/a	n/a	n/a	n/a	n/a	n/a
Grain-size matrix	Fine to medium sand	Coarse silt to fine sand	Coarse silt	Coarse silt to fine sand	Coarse silt to very fine sand	Coarse silt to fine sand	Coarse silt to very fine sand
Dip-direction/dip	174/24, 178/29, 156/31	353/21	213/19	167/17 → Bedding?	220/01 → Sub-horizontal toward SW	n/a	n/a
Monomict/polymict	Polymict	Polymict	Polymict	Polymict	Polymict	Polymict	Polymict
Specifics	Matrix is unconsolidated Brown colored Chalky Sand lenses Clasts are hydrodynamically oriented Flattened and rounded clasts	Lithic fragments within matrix → Mafic material Flattened clasts (30%) are hydrodynamically oriented.	Clasts are not so hydrodynamically oriented.	Moderately poor hydrodynamically orientation of small clasts	Reddish weathering Layers with larger & smaller clasts, alternated with silty layers Some hydrodynamically oriented clasts within the outcrop	Lithic fragments within matrix → Mafic material 2 meter coarse gravel layer at bottom of outcrop followed by alternations of sandy/silty layers with some gravel lenses	n/a

Table 4.7 Outcrop observations within the Fanglomerate Formation, May 2023.

Formation	Pakhna	Lefkara	Umber	UPB + LPB + BG	SCD	PG	LG + MG	Other
Stop 2.2								
Size	n/a	n/a	n/a	n/a	n/a	n/a	n/a	n/a
Percentage	n/a	2%	n/a	16%	> 80%	2%	n/a	n/a
Characteristics	n/a	Recrystallized grain → Calcite Oxidized mineral → Pyrite Red-pinkish weathered White matrix	n/a	Vesicles & amygdales Brown weathered	Greenish → Epidotized Black fine texture → Micro-gabbro Matrix is highly oxidized Brown matrix	Needle-like minerals → Hornblende	n/a	n/a
Stop 5.1b								
Size	n/a	n/a	0.5 – 10 cm	5 mm – 15 cm	< 10 cm	8 cm	6 cm	n/a
Percentage	n/a	n/a	10%	30%	57%	2%	1%	n/a
Characteristics	n/a	n/a	Rusty weathered Brick-red colored Conchoidal fracturing → Si-rich Very small minerals < 1 mm → (Chalco)pyrite Subangular – subrounded	Vesicles Amygdales → Filled with quartz or weathered Orange-red weathered Very fine texture Subangular to rounded	Fine texture → Micro-gabbro Very fine texture → Basalt Plagioclase & pyroxene < 1 mm Brown to greyish weathered Subangular – rounded	Fine texture Plagioclase (50%) Pyroxene (40%) Quartz (10%) Felsic volcanic rock Subrounded	Coarse texture Minerals > 1 mm Plagioclase (40%) Pyroxene (60%) Subrounded Heavily weathered → Unconsolidated, breaks apart very easily Grey, brown, orange, white weathered Subrounded	n/a
Stop 5.3								
Size	< 10 cm	n/a	3 – 5 cm	2 – 15 cm	2 mm – 15 cm	8 cm	3 – 30 cm	5 – 30 cm
Percentage	2%	n/a	5%	40%	37%	1%	10%	5 %
Characteristics	White, beige, pinkish weathered	n/a	Conchoidal fracturing → Si-rich	Vesicles Amygdales → Epidotized, filled	Fine texture → Micro-gabbro	Felsic volcanic rock Needle-like minerals →	Coarse texture Minerals > 1 mm Plagioclase (40%)	Mafic → Dark grey or black colored

	Coral fragments Forams & pellets Some dolomitization Packstone Wackestone Angular – subrounded		Green dots → Copper Rusty greenish weathered Subangular	with quartz or epidote Olive-brown weathered Very fine texture Subangular – subrounded	Very fine texture → Basalt Epidotized Minerals < 1 mm Plagioclase (40 – 60%) Pyroxene (40 – 60%) Subrounded to rounded	Hornblende (0.5 – 3 mm) Feldspar Quartz Coarse texture Subrounded – rounded	Pyroxene (60%) Some alternation between darker and lighter layers within the clast Subrounded	Pyroxene (70%) White flakes → Plagioclase (20%) Unknown mineral (10%) Coarse to very coarse texture Subrounded **(Micro-)Gabbro**
Stop 5.4								
Size	n/a	n/a	n/a	2 mm – 15 cm	2 mm – 30cm	n/a	5 – 30 cm	10 – 15 cm
Percentage	n/a	n/a	n/a	25 – 30%	55 – 60%	n/a	10%	5%
Characteristics	n/a	n/a	n/a	Amygdales Subrounded – rounded	Subangular – rounded	n/a	Mineral size > 1 mm Subrounded – rounded	Coarse texture Black & green minerals Plagioclase (< 40%) Pyroxene (> 60%) Unknown mineral Subrounded **(Micro-)Gabbro**
Stop 6.2								
Size	4 – 15 cm	n/a	2 – 8 cm	1 – 20 cm	2 mm – 40 cm	< 6 cm	< 7 cm	n/a
Percentage	8%	n/a	3%	30%	50%	2%	7%	n/a
Characteristics	Conchoidal fracture Forams Very fine grained Wackestone Grey-beige weathered Subrounded	n/a	Jasper Conchoidal fracturing → Si-rich & Quartz Silicified Red/orange/dark rusty weathered Subangular	Vesicles Amygdales → Filled with chalcopyrite Very fine texture Dark rusty weathered Subrounded – rounded	Fine texture → Micro-gabbro Very fine texture → Basalt Epidotized Grey/black greenish weathered Subrounded – rounded	Quartz (45%) Greenish transparent needles → Hornblende (20%) Plagioclase (20%) Pyroxene (< 15%) Felsic volcanic rock Subrounded	Coarse texture Minerals > 1 mm Plagioclase (40%) Pyroxene (60%) Heavily weathered Subrounded – rounded	n/a

Stop 6.3a/b								
Size	18 cm	n/a	1 – 15 cm	< 15 cm	2 mm – 70 cm	???	6 cm	15 cm
Percentage	3%	n/a	5%	20%	70%	0 – 5%	0 – 2%	0 – 2 %
Characteristics	Wackestone Packstone Beige/white colored Forams Subrounded	n/a	Jasper Alternation → Iron- or manganese-oxide minerals Dark rusty weathered Si-rich → Quartz Subangular – subrounded	Vesicles Amygdales → Filled with chalcopyrite or quartz Green reddish weathered Very fine texture Subrounded	Fine texture → Micro-gabbro Very fine texture → Basalt Minerals < 1 mm Plagioclase Pyroxene Subangular – rounded	At stop 6.3a no Plagiogranite is found. Stop 6.3b: Needle-like minerals → Hornblende Covers at 6.3b ~5% of the outcrop Felsic volcanic rock	Clast 1 taken from the ground and not in the outcrop. Minerals > 1 mm Plagioclase Pyroxene Coarse texture Clast 2 in situ Coarse texture Plagioclase Pyroxene Mineral size 1 – 5 mm Pegmatitic part within clast	Black colored Quartz? White flakes → Plagioclase (20%) Black dots → Pyroxene (40%) Greenish minerals → Unknown (40%) Subrounded **(Micro-)Gabbro**
Stop 8.2								
Size	8 cm	n/a	< 5 cm	< 10 cm	2 mm – 30 cm	< 5 cm	< 5 cm	< 7 cm
Percentage	2%	n/a	5%	20%	60%	2%	1%	10%
Characteristics	Beige to white colored Silty No fossils Silicious limestone Subangular	n/a	Rusty weathered Ochre, red-brown colored Transparent milky white clast → Quartz nodule Subangular – subrounded	Vesicles Amygdales filled with oxides Very fine texture Grey greenish or burgundy colored Subangular – subrounded	Fine texture → Micro-gabbro Very fine texture → Basalt Green greyish colored Rusty weathered Subangular – subrounded	Felsic volcanic rock Quartz Feldspar Pyroxene Needle-like minerals → Hornblende Very weathered Subangular	Coarse texture Minerals > 1 mm Heavily weathered → Breaks apart easily Plagioclase (40%) Pyroxene (60%) More feldspar-rich at the rim Subrounded	Mafic White flakes → Plagioclase Black minerals → Pyroxene Green minerals → Olivine or pyroxene Subangular **Micro-gabbro**

Table 4.8 Observations of the clasts within the Fanglomerate Formation, May 2023.

4.3 Optical microscopy

The clasts classified as “Other” at stops 5.3, 5.4 and 6.3a/b are similar but were not identifiable in the field. The mineral characteristics observed during the optical microscopy are summarized in table 4.9. The identified minerals occur in the following proportions, 45% plagioclase, 40% pyroxene, 5% tremolite or actinolite, 8% epidote and chlorite, and 2% oxide-minerals, probably iron- or manganese-oxides. Based on the proportions of the present minerals, the rock is identified as an altered micro-gabbro.

Minerals	Percentage	Characteristics PPL (fig. 4.13)	Characteristics XPL (fig. 4.14)
Plagioclase Feldspar	45%	Color: Colorless Relief: Low Pleochroism: No	Color: Black, grey or white Interference: First-order Extinction: Undulous & Inclined Twinning: Polysynthetic type Anisotropic
Pyroxene	40%	Color: Colorless Relief: Higher than feldspar and hornblende Pleochroism: Yes, violet, pinkish to greenish shades	Color: Pink, blue, purple or orange Interference: First- to second-order Extinction: Inclined Twinning: Polysynthetic type Anisotropic
Tremolite – Actinolite	5%	Color: Colorless Relief: Moderate to high Pleochroism: -	Color: Blue, pink, yellow, orange or brown Interference color: Second-order Extinction: Inclined Structure: Fibers Anisotropic
Chlorite and epidote	8%	Color: Green brownish Relief: Higher than plagioclase Pleochroism: Yes, shades of green and bluish green	Color: Orange Interference: Second-order Extinction: Inclined Twinning: No Anisotropic
Oxide-minerals	2%	Color: Black	Color: Black Interference: First-order Extinction: None Twinning: No Isotropic

Table 4.9 Observed PPL and XPL mineral characteristics of the unknown clast at stop 6.3a/b during the optical microscopy.

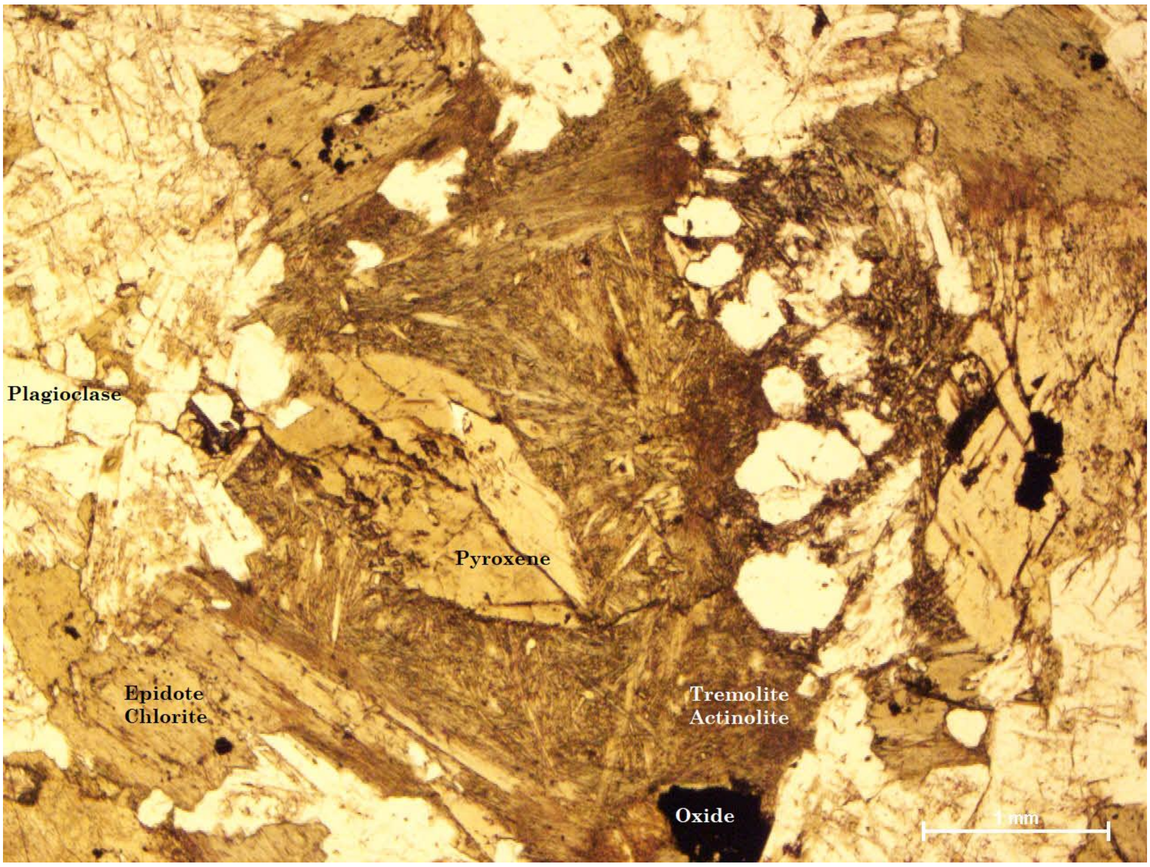

Figure 4.13 PPL image showing the various minerals in the rock "Other" of stop 6.3a/b, zoom 4x.

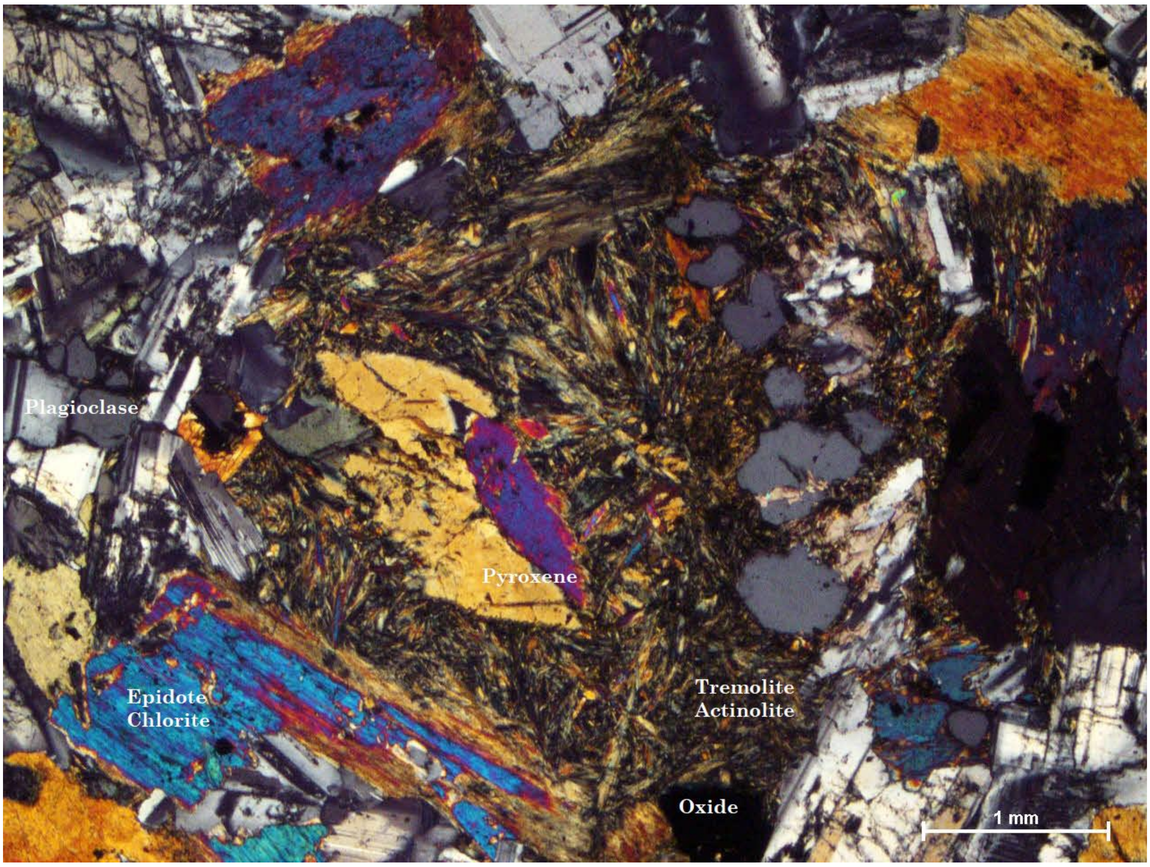

Figure 4.14 XPL image showing the various minerals in the rock "Other" of stop 6.3a/b, zoom 4x.

Chapter 5 Discussion

5.1 Numerical modelling

The surface topography in a subduction system is controlled by the slab's buoyancy, and the rheological and geometrical parameters within the subduction zone (Crameri et al., 2017). Trends observed in the results are discussed in the sections below.

5.1.1 Comparing oceanic lithosphere models

By comparing the oceanic lithosphere models, we firstly observe that the height of the collisional high of Models 2 and 4 are lower than in Models 1 and 3 (table 5.1). Additionally, in Models 2 and 4 a new zone of high strain rate localizes (fig. 4.1 and 4.4) after 9.5 (Model 4) to 10 Myr (Model 2), which is interpreted as 1) a developed back-thrust in response to continuous convergence, or 2) the initiation of a potential new subduction zone. The earlier back-thrust development or subduction initiation in Model 4 is a response to the higher initial imposed subduction velocity of 3 cm/year compared to the 2 cm/year in Model 2. A back-thrust develops in a low-angle Chilean-type subduction setting causing a compressional back-arc region, whereas a Mariana-type subduction zone results in a tensional back-arc region. The coupling of the subducting plate to the overriding plate in Models 2 and 4 result in a horizontally compressional tectonic regime inducing large back-thrusts causing inter-plate earthquakes (Uyeda, 1981). Nevertheless, the dip angle of 13^o till 45 km depth followed by ~28^o in Models 2 and 4 is the main reason why a new subduction zone can initiate. Once the slab dips with an angle < 15^o, the subducting plate has a large interface with the overriding plate causing friction and eventually the subducting plate to stick to the overriding plate (Crameri et al., 2017). As a result, the subduction velocity decreases, subduction becomes inhibited and the subducting plate tends to retreat causing extension in the overriding plate (Crameri et al., 2017). However, due to the continued convergence exerted by the model's velocity boundary condition, compressional forces are transmitted through the overriding lithosphere to an area further away from the trench on the overriding plate, where strain relocalizes and the initiation of a potential new subduction zone emerges. In these cases, the compressional forces are not accommodated on the plate contact but in the region behind the collisional high, explaining why the collisional highs in Models 2 and 4 are lower than in the Models 1 and 3 (table 5.1). When subduction occurs with an angle of 30^o (Models 1 and 3), the interface with the overriding plate is smaller, causing less friction which results in more smoothly subduction. The compressional forces are accommodated on the initial plate contact resulting in higher collisional highs. The second trend observed is a deeper trench in Models 1 and 3 compared to Models 2 and 4. According to Crameri et al. (2017) the depth of the trench is dependent on the subduction angle. Steeper subduction angles cause stresses to be transferred to the surface along the slab (slab pull), amplifying topographic depressions around the trench itself (Crameri et al., 2017). When subduction occurs with a shallow dip, stresses transfer towards the surface through the mantle wedge, i.e. slab suction, forming topographic amplification in the back-arc region (Crameri et al., 2017). By comparing the regions behind the collisional highs, we see a well-developed topographic region, i.e. curved topography, containing 1 – 4 km high hills separated by 2 – 5 km deep valleys in Models 2, 3 and 4, whereas the 0.8 km deep depression in Model 1 forms a flat, i.e. undeveloped, topographic region. In Models 2 and 4 the curved topography is due to the shallow dipping slabs, as explained above, whereas in Model 3 the curved topography is probably due to the higher subduction velocity resulting in more compression and therefore more topography formation.

Feature	Model 1 2 cm/year 30°	Model 2 2 cm/year 13° + 28°	Model 3 3 cm/year 30°	Model 4 3 cm/year 13° + 28°
Collisional high	5.8 km	3.5 km	8 km	5 km
Trench	8.5 km	8.0 km	8 km	6 km
Forebulge	1.5 km	2.5 km	4.8 km	4.5 km
Region behind collisional high, i.e. hinterland	Relatively flat Undeveloped	Curved Well-developed	Curved Well-developed	Curved Well-developed
Characteristic	None	After 10 Myr, a new zone of high strain rate localizes	From 8 to 10 Myr, strain rate becomes almost constant throughout the model, resulting in a well-developed hinterland	After 9.5 Myr, a new zone of high strain rate localizes

Table 5.1 Summary oceanic lithosphere models.

5.1.2 Discussion continental lithosphere model

There are multiple reasons why in Model 5 the continental lithosphere starts flowing, with the continental lithospheric mantle dripping as blobs into the asthenosphere (Appendix A.5, figures 7 and 10), instead of simulating subduction. Firstly, by comparing the rheological strength models of the oceanic overriding plate (fig. 3.2) with the continental subducting plate (fig. 3.6), the continental subducting plate is stronger compared to the oceanic overriding plate. A continental lithosphere correlates the "Crème brûlée model" (fig. 5.1) when the strong upper crust is underlain by a weak lower crust and mantle (Burov, 2011).

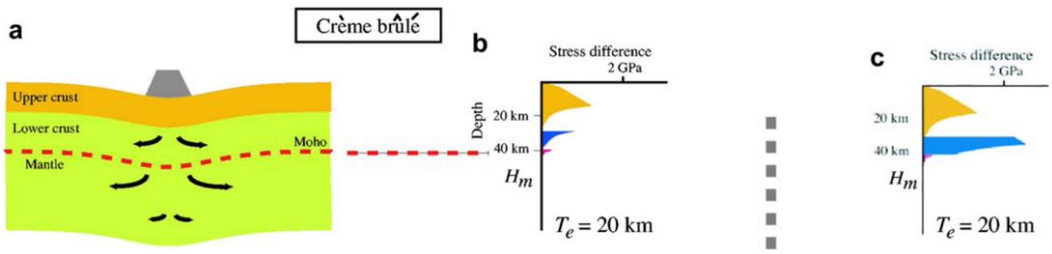

Figure 5.1 a) Deformation model, b) Yield strength envelope of the crème brûlée model with a weak lower crust, c) Yield strength envelope the crème brûlée model with a strong lower crust (Burov, 2011).

The multilayered structure and continental lithospheric thickness enables the rheological layers, i.e. crust and mantle, to decouple mechanically, explaining why this phenomenon does not occur in the two layered oceanic lithospheric models. Exceptions for decoupling occurs once the continental crust is thin or old, hence cold (> 750 Ma) and/or the mantle is dehydrated. In the crème brûlée model, the weak lower crust functions as a weak ductile zone allowing mechanical decoupling between the upper crust and mantle by delamination of the mantle. Once decoupling is finished, the lithospheric mantle start to sink as blobs into the asthenosphere. In addition, the undepleted continental mantle is 25 kg/m^3 denser compared to the underlying asthenosphere. As a result, the gravitational unstable continental lithospheric mantle sinks into the asthenosphere due to the Rayleigh – Taylor instability (fig. 5.2; Burov, 2011).

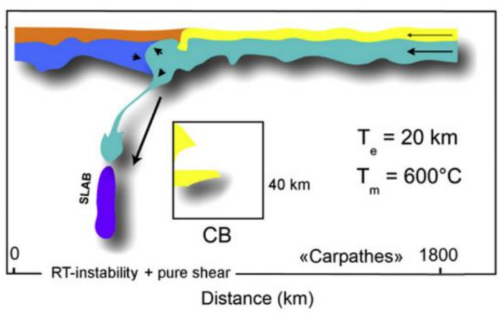

Figure 5.2 The mantle dripping as blobs into the asthenosphere due to the Rayleigh – Taylor instability (Burov, 2011).

Secondly, the subducting continental crust has a lower density than the oceanic overriding lithosphere (Zheng, 2012). This buoyancy contrast causes resistance against subduction of the downgoing plate. Thirdly, deformation barely occurs due to the higher mantle viscosity compared to the continental lithosphere. As a result, the slab buoyancy force causes the mantle below to deform, instead of pulling the continental lithosphere downward (Crameri et al., 2017). Lastly, according to Burov (2011) a continental lithosphere consisting of three layers cannot subduct once convergence velocities are below 2 – 3 cm/year (Burov, 2011). Unfortunately this last argument is a statement in the paper without any detailed explanation, but when convergence velocities are low in combination with the lower density and very strong yield strength envelope, there is more time for decoupling and resistance against subduction enlarges. All aspects do not enable subduction to occur, potentially rejecting the continental lithosphere hypothesis.

5.1.3 Comparing oceanic-continental lithosphere models

Subduction in the oceanic-continental lithosphere models is possible, because the oceanic lithospheric part has a higher density, pulling the continental lithospheric part downward (Zheng, 2012). Nevertheless, at a certain moment the resistance of the continental lithospheric part against subduction overcomes the downward pulling force of the oceanic lithospheric part. At this moment, the slab pull and slab suction forces of the oceanic lithospheric part cause slab break off (Crameri et al., 2017). In Models 8 and 9, the oceanic lithospheric part starts to break off after 8 Myr and is completely ruptured after 10 Myr, whereas in Models 6 and 7 slab break off just started after 10 Myr. The difference in break off timing is due to the varying subduction velocities between the models, where the faster converging forces lead to earlier break off than the slower converging forces. The downward slab pull and slab suction forces increase with slab sinking depth. Overcoming the resisting upward force of the continental lithosphere occurs earlier once subduction velocities are high, resulting in accelerated slab sinking, increasing the downward force significantly triggering slab break off. On the other hand, in a slow subduction velocity setting the downward force increases barely due to slow slab sinking, requiring more time to overcome the resisting upward force and slab break off to occur (Crameri et al., 2017).

By comparing these models, there are some trends observed (table 5.2). Firstly, lithospheric bending dissipation increases with slower convergence rates resulting in higher forebulges (Crameri et al., 2017). In Models 6 and 7, the forebulges are higher compared to Models 8 and 9 due to the subduction velocity of 2 cm/year compared to 3 cm/year, respectively. Additionally, the height of the forebulge depends on the dip angle. The shallower dipping slab in Model 7 explains the higher forebulge compared to Model 6. Secondly, the region behind the collisional high in Model 6 subsides 2.0 km, whereas in Model 7 subsidence varies laterally between 1.0 km directly behind the collisional high, deepening up to 3.0 km with increasing distance from the collisional zone. The difference is explainable by the shallower dipping slab in Model 7 amplifying topographic depressions in the region behind the collisional high, whereas the steeper-dipping slab in Model 6 amplifies topographic depressions around the trench (Crameri et al., 2017). The more curved and well-developed topographic regions behind the collisional high in Models 8 and 9 are due to the higher subduction velocities, causing more compression and therefore more topography formation in the hinterland. For the collisional high and the trench, no clear trends are observed. In Models 8 and 9 the slab is completely ruptured after 10 Myr, affecting the geometry due to the rebounding continental lithosphere.

Feature	Model 6 2 cm/year 30°	Model 7 2 cm/year 13° + 28°	Model 8 3 cm/year 30°	Model 9 3 cm/year 13° + 28°
Collisional high	7.5 km	7.5 km	7.0 km	6.5 km
Trench	6.0 km	5.5 km	5.0 km	6.0 km
Forebulge	2.0 km	3.5 km	1.5 km	1.5 km
Region behind collisional high, i.e. hinterland	Flat Undeveloped	Flat Undeveloped	Curved Well-developed	Curved Well-developed
Characteristic	Slab break off starts after 10 Myr	Slab break off starts after 10 Myr	Slab break off starts after 8 Myr After 10 Myr, slab is completely ruptured	Slab break off starts after 8 Myr After 10 Myr, slab is completely ruptured

Table 5.2 Summary oceanic-continental lithosphere models.

5.1.4 Oceanic vs. oceanic-continental lithosphere models

By comparing the oceanic vs. the oceanic-continental lithosphere models there are also some trends (table 5.1 and 5.2). Firstly, the height of the collisional high is supposed to be strongly controlled by the rheology. The stronger upper plate in the oceanic lithosphere models should result in a higher collisional high (Crameri et al., 2017). Nevertheless, the collisional highs are actually higher in the oceanic-continental lithosphere models. The resistance of the continental lithospheric part against subduction probably accommodates more compression transmitted to the collisional high region, explaining why the expected trend is not observed. Secondly, a stronger plate results in a deeper trench (Crameri et al., 2017). The plate strength in the oceanic lithosphere models is higher compared to the oceanic-continental lithosphere models. This trend is seen in the numerical models, because the trenches in Models 1 – 4, with stronger oceanic lithosphere, are deeper than the trenches in Models 6 – 9, with weak continental lithosphere. Lastly, a thicker and weaker plate results in a more negatively buoyant slab and hence a higher forebulge (Crameri et al., 2017). Hence, higher forebulges are expected in the oceanic-continental lithosphere models due to the thickness and weakness of the continental lithospheric part. By comparing Models 1 and 2 with Models 6 and 7, this trend is observed. However, by comparing Models 3 and 4 with Models 8 and 9, this trend is not observed. This can be argued by the completely ruptured oceanic lithospheric parts in Models 8 and 9, which is an active mechanism stopping subduction. Once the detached slab sinks into the mantle, the slab pull force vanishes, stopping convergence and creating a new thermal equilibrium in the upper part (Zedde and Wortel, 2001). The rebounding continental lithosphere and new thermal equilibrium changes the geometry of a subduction zone.

5.2 Fieldwork observation discussion

5.2.1 Excluded stops

The formation identifications of stops 6.4, 8.3 and 9.2 were uncertain and hence excluded in '*Chapter 4.2 Fieldwork observations*'. Stop 6.4 was recommended by the Geological Survey Department of Cyprus but they did not know the exact formation. On the Geological Survey Map, this could be either Fanglomerate Formation or Holocene depositions. Stop 8.3 is located within the Fanglomerate Formation according to the Geological Survey Map. Nevertheless, the outcrop contains clasts originating from the Umbers (3 – 5%), Chert (5%), Upper and Lower Pillow Basalts and Basal Group (25%), Sheeted Dyke Complex (45%), Plagiogranites (5%), Massive and Layered Gabbro (15%) and Other (2%). In the field, the "Other" could be either identified as quartzite, indicating Fanglomerate Formation, or Umbers, indicating Kakkaristra Formation. Stop 9.2 was a location found during this study (table 3.3). Directly above the Kakkaristra Formation (stop 4.2), conglomerates cropped out on a hill.

Based on stratigraphy (fig. 2.6), a gravel channel from the Apalos Formation was more likely instead of the Fanglomerates Formation (Schirmer et al., 2010).

5.2.2 Observed conglomerate trend

By examining the clast nature within the conglomerates of the Pakhna, Nicosia, Kakkaristra and Fanglomerate Formations, we found that the younger formations contained a higher content of deeper crustal rocks compared to the older formations containing higher limestone contents, which is an indication for continuous uplift since the Miocene. Additionally, a trend in the sortedness, roundness and clast size was observed from the Pakhna Formation, i.e. oldest, towards the Fanlgomerate Formation, i.e. youngest. The conglomerates change from very poorly sorted angular clasts with a large grain size range (< 1 cm – 2 m), towards moderately sorted subangular to rounded clasts with a smaller grain size range (1 mm – 70 cm). Furthermore, the deeper crustal rock contents do also vary with travel distance from the Troodos ophiolite observed at stop 9.3 (fig. 3.10) from the Kakkaristra Formation. By comparing the content of the individual rock types between stop 9.3 and the other stops of the Kakkaristra Formation (table 4.6), the Upper and Lower Pillow Basalts and Basal Group are less than expected, whereas the Massive and Layered Gabbro are more than expected. The Upper and Lower Pillow Basalts and Basal Group were little eroded, because the outcrop is directly deposited above this oceanic crustal unit, explaining why only a few clasts were found. Instead, the Massive and Layered Gabbro are still intact due to the small travel distances, whereas normally these clasts are rare because of the heavily and crumbly weathering.

Within the Pakhna Formation lava clasts from the Troodos ophiolite were expected (Ring and Pantazides, 2019) but not found during this study. The Peripheral Sands Association, which is a poorly developed facies association within the Pakhna Formation, contains ophiolite-derived pebble- to cobble-size clasts, i.e. diabase (dolerite), weathered basalt and rare metalliferous chert from the Limassol Forest Block. The study of Eaton and Robertson (1993), in which mafic material was found in the Pakhna Formation, was conducted in the area south of the Arakapas Fault Zone (Eaton and Robertson, 1993). Within the conglomerates of the Pakhna Formation no clasts with a volcanic origin were identified during this study, indicating the oceanic crust was not exposed to erosion and/or weathering at the time of initial deposition. The deviation from the literature is explainable since 1) this study focused on the northern flank of the Troodos ophiolite, and 2) the ophiolitic terrain, where this study was conducted, was uplifted during the deposition of the Pakhna Formation, resulting in deformation and erosion followed by gravitational transport of the of the ophiolite-derived clasts (Eaton and Robertson, 1993). However, clasts originating from the Pakhna Formation itself are present just on top of the Pakhna reefal limestones, indicating that it was briefly exposed requiring at least 1,600 meter uplift (table 5.3) during the Miocene (23.3 – 6.5 Ma). Within the Nicosia Formation, the deepest clasts originate from the Sheeted Dyke Complex and Plagiogranite unit of the ophiolite, indicating at least 4,340 meter uplift (table 5.3) during the Early Pliocene (5.2 – 2.5 Ma). The deepest clast in the Kakkaristra conglomerates is a Garnet-Gabbro, which is the deepest identified unit during this study, indicating 5,732 up to 9,572 meters uplift (table 5.3) during the Late Pliocene (2.0 – 1.8 Ma). Within the Fanglomerate Formation (ultra)mafic ophiolite derived clasts were expected (Gass et al., 1994). However, during this study the deepest mafic clast found within the Fanglomerate Formation is a Massive or Layered Gabbro, whereas the Garnet-Gabbro in the Kakkaristra originates from deeper. Hence, the ophiolite is not uplifted but instead subject to erosion during the Pleistocene (1.8 – 0.01 Ma). Finding no ultramafic clasts is explainable, because the ultramafic mantle material serpentinized over time. Serpentinization change the rheology of the mantle peridotite from dense, anhydrous, strong and low permeable towards light, hydrated and weak (Evans et al., 2021). The Troodos ophiolite became subject to erosion and weathering since its exposure 2 Ma. The erosional products are not resistant against erosion and therefore completely weathered before the Fanglomerate Formation deposited.

To discuss the accurate amount of uplift at a certain moment in time, knowledge about the ophiolitic sequence (fig. 1.2) and sedimentary cover thicknesses, see '*Chapter 2.2.1 Sedimentary stratigraphy*', are required, as well as ocean depth once the Lefkara Formation was deposited. The thicknesses of the oceanic crustal sequence units is based on figure 5.3 (Gass, 1977). The Pillow Lavas, i.e. Upper and Lower Pillow Basalts and Basal Group, is approximately 580 meters thick, with a 1,300 meters thick Sheeted Dyke Complex underneath (Gass, 1977). The thickness of the Gabbroic Layer, i.e. Massive and Layered Gabbro, is debated in the literature, varying in thickness from 1,160 meters (fig. 5.3; Gass, 1977) to 1,500 meters (Thy, 1987) up to 5,000 meters based on a Gabbroic Layer covering $^2/_3$ of the crustal thickness (Abelson et al., 2001). This report uses both the minimum and maximum thickness for the Gabbroic Layer to calculate minimum and maximum uplift rates (table 5.3).

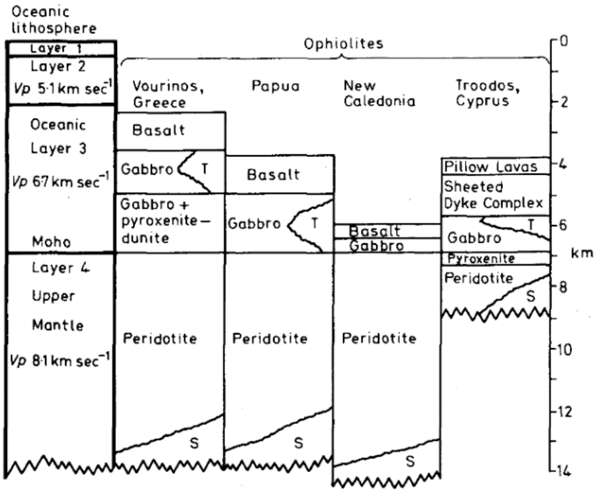

Figure 5.3 Sequence of the oceanic crust and oceanic mantle, providing the used thicknesses from the 'Troodos, Cyprus' stratigraphic column (Gass, 1977).

The Plagiogranite, which officially forms in between the Sheeted Dyke Complex and the Massive and Layered Gabbro (fig. 1.2), is missing in the oceanic crustal sequence of figure 5.3. As seen at the outcrop of Geosite 33, the Sheeted Dyke Complex intrudes through the Plagiogranites, indicating a not well-defined upper boundary of the Plagiogranite unit. Nevertheless, finding Plagiogranite in a conglomerate means that the Sheeted Dyke Complex was most likely almost completely exposed (table 5.3). Furthermore, the lower boundary of the Plagiogranite unit is also debatable, because heavily weathered Plagiogranite and Gabbro are often indistinguishable, especially once hornblende was missing, making rock identification debatable. Some clasts are probably wrongly interpreted in the field, so when doubting the presence of Plagiogranite along with Gabbro indicate that at least the upper part of the Gabbroic Layer was exposed (table 5.3). The depth of the Garnet-Gabbro is not sure, but based on general knowledge about fractional crystallization, the Garnet-Gabbro originate from deepest, while the Massive and Layered Gabbro originate from shallowest (table 5.3).

The total sedimentary cover, as described in '*Chapter 2.2.1 Sedimentary stratigraphy*', has a thickness of 1,932 meters, in which the Lefkara Formation was deposited at a debatable seabed depth (table 5.3), varying between 2,600 to 3,200 meters below sea level (Jenkyns and Winterer, 1982; Robinson et al., 2003). In the uplift calculation, a seabed depth of 3,000 meters below sea level is used (table 5.3).

Formation name	Formation thickness	Minimum uplift	Maximum uplift	Ma
Fanglomerate	86 m	5,732 m	9,572 m	1.8 – 0.01
Apalos	46 m			2.0 – 1.8
Kakkaristra and Athalassa	100 m	5,732 m	9,572 m	2.5 – 2.0
Nicosia	280 m	4,340 m	4,340 m	5.2 – 2.5
Kalavasos	20 m			6.5 – 5.2
Pakhna	450 m	1,600 m	1,600 m	23.3 – 6.5
Lefkara	950 m			74.0 – 23.3
Seabed depth is -3,000 meter below sea-level				
Kannaviou	750 m			83.0 – 74.0
Perapedhi	10 m			90.4 – 83.0
UPB + LPB + BG	~580 m			
SDC + PG	~1,300 m			
PG + MG + LG	~600 – 3,500 m			
Garnet-Gabbro	~560 – 1,500 m			

Table 5.3 Overview of the oceanic crustal and sedimentary cover thicknesses and calculated minimum and maximum uplift correlated to a certain moment in time.

5.3 Correlating numerical modelling and field observational data

Uplift from the obduction event simulated with the numerical models, covers a time period of 10 Myr (Morag et al., 2016), which initiated during the early to middle Late Cretaceous, ca. 90 Ma (Robertson, 1998a) and stopped 80 Ma. The first sediments deposited on the ophiolite are the chalks from the Lefkara Formation during the Maastrichtian (74.0 Ma). The obduction event did not contribute to the uplift calculated in table 5.3 based on the obduction event and the depositional timing of the Lefkara Formation. The first volcanic clasts are found in the Nicosia conglomerates, indicating the ophiolite was not exposed until the Early Pliocene (5.2 Ma). Hence, the maximum uplift contributed by obduction is 3,760 meters based on the seabed depth, i.e. 3,000 meters, and Kannaviou and Perapedhi Formation thicknesses, ensuring that the Upper and Lower Pillow Basalts and Basal Group are not subaerially exposed. By correlating the maximum amount of uplift contributed from obduction with the numerical model data, Model 2 is the only model that generates an approximately 3.5 km high collisional arc after 10 Myr. All other models generate more than 5 km uplift during 10 Myr, producing too much uplift to keep the ophiolite below sea level. Based on this correlation, I propose that the lithosphere of the subducting slab is made of oceanic crust. This would be in line with the studies of Robertson (1998a), Khair and Tsokas (1999), Morag et al. (2016) and Feld et al. (2017) (Feld et al., 2017; Khair and Tsokas, 1999; Morag et al., 2016; Robertson, 1998a).

This study focused on how the collisional high varies with varying footwall origins, subduction velocities and subduction angles. Nevertheless, the numerical models are a simplification of the real world. The first limitation is assuming no phase changes over time. During the convergence, the subducting plate sinks deeper into the mantle. Over time, pressure and temperature increase which normally results in metamorphic reactions, changes in rheological phases and buoyancy. In the models, these effects are excluded, because only one density is used for each phase (Xue et al., 2020). In addition, internal variations or heterogeneities in the crust are excluded. In nature, such heterogeneities might accommodate some stresses affecting the results. Furthermore, initial boundary conditions are arbitrary. In my case I implemented an active lateral stress on the system causing subduction, whereas others use the buoyancy of the downgoing plate to drive subduction (Capitanio et al., 2007).

5.4 Uplift history

In the literature, most authors plead for a two phase uplift history of the Troodos ophiolite, including an obduction event and serpentinization phase. If serpentinization solely caused the total amount of uplift of the Troodos massif, a more circular outcrop pattern is expected instead of the N-S elongated structure based on bouguer gravity anomalies (Ring and Pantazides, 2019; Shelton, 1993). Shelton (1993) provides one theory arguing that the N-S oriented basins on the northern flank of the Troodos ophiolite post-date the serpentinization. Thus, serpentinization resulted in a circular pattern followed by normal listric faulting, deforming the ophiolite towards a more N-S oriented elongated outcrop (Shelton, 1993). However, many authors argue that the serpentinization force is not strong enough to drag also the overlying gabbro, sheeted dykes and pillow lavas upwards (Ring and Pantazides, 2019). Furthermore, Weber et al. (2011) provides magnetostratigraphic data showing a minor uplift phase, probably by underthrusting of the Eratosthenes Seamount, followed by a major uplift phase due to serpentinization causing pulsed uplift (Weber et al., 2011).

The uplift history constrained here comprises at least two uplift phases that can be correlated to uplift phases proposed in the literature, including a minor tectonically induced uplift phase, i.e. obduction (Morag et al., 2016; Robertson, 1998a), followed by a significant uplift phase due to serpentinization (Morag et al., 2016; Robertson, 1977). Based on obtained numerical model and field observational data, individual uplift rates of both events can be calculated to provide knowledge for an accurate uplift history reconstruction.

As discussed in '*Chapter 5.3 Correlating numerical modelling and field observational data*', the likeliest subduction setting obducting the Troodos ophiolite occurred in Model 2. The total topography in the collisional high region increased 3.5 km in a 10 Myr time period. The uplift rate (table 5.4) is calculated with the following formula:

Uplift rate (km/Myr) = Total topography formed in the collisional high region (km) / 10 Myr

Model	Topography formed in collisional high region (km)	Timespan (Myr)	Uplift rate (km/Myr)
2	3.5	10	0.35 km/Myr

Table 5.4 Calculated uplift rate during obduction in Model 2.

The tectonically induced uplift phase is followed by serpentinization, which uplifts the sedimentary cover and the ophiolite sequence. Uplift during the Miocene towards the Late Pleistocene is divided in four phases, in which the individual uplift rates between two conglomerate depositions are calculated. In the calculation, the seabed is used as reference (Uplift = 0 km; Time = 0 Myr), with the stratigraphic age starting 74.0 Ma. The uplift rates (table 5.5) are calculated with the following formula:

Uplift rate (km/Myr) = Amount of uplift between two conglomerates (km) / timespan between the two conglomerates (Myr)

For example, 1) The <u>minimum uplift rate</u> for the Nicosia Formation, or 2) The <u>maximum uplift rate</u> for Kakkaristra Formation:

1) Uplift rate = (4.34 – 1.6) / (6.5 – 2.5) = 0.685 km/Myr
2) Uplift rate = (9.572 – 4.34) / (2.5 – 2.0) = 10.46 km/Myr

Formation	Age (Ma)	Total uplift (km)[1]	Uplift quantity between two conglomerates (km)	Timespan between the two formations (Myr)	Uplift rate (km/Myr)
Minimum uplift rate					
Pakhna	23.3 – **6.5**	**1.6**	1.6	67.5	0.02
Nicosia	5.2 – **2.5**	**4.34**	2.74	4	0.69
Kakkaristra	2.5 – 2.0	5.73	1.392	0.5	2.78
Fanglomerate	1.8 – 0.01	5.73	0.0	1.99	0.00
Maximum uplift rate					
Pakhna	23.3 – 6.5	1.6	1.6	67.5	0.02
Nicosia	5.2 – **2.5**	**4.34**	2.74	4	0.69
Kakkaristra	2.5 – **2.0**	**9.57**	5.23	0.5	10.46
Fanglomerate	1.8 – 0.01	9.57	0.0	1.99	0.00

Table 5.5 Calculated maximum and minimum uplift rates for each individual uplift pulse during the Miocene towards the Late Pleistocene based on the sedimentary cover. [1]Total uplift is calculated in table 5.3.

The individual uplift rates can be correlated to regional tectonic evolution events, as described in '*Chapter 2.1.1 Regional tectonic evolution*', providing knowledge to constrain an accurate uplift history.

The uplift started with a tectonically induced uplift phase. If we consider the obduction as the mechanism for the first phase as modelled in Model 2, this should occurred during oblique obduction from 90 – 80 Ma (Dilek and Thy, 1990) resulting in a minor uplift phase of 0.35 km uplift/Myr (table 5.4), covering a time period of 10 Myr (Morag et al., 2016). Uplift was generated by 1) obduction induced deformed ultramafic rocks of oceanic layer 4, and 2) serpentinization due to liberated fluids from the crust of the downgoing plate that brought these hydrating fluids in the mantle wedge of the subduction zone (Morag et al., 2016; Robertson, 1977). Serpentinization during this early uplift phase would also fit with the oceanic lithosphere hypothesis, because the subducted oceanic crust releases plenty aqueous fluid phases altering the ultramafic rocks, whereas in subducted continental crust free fluid phases are scarce (Hermann et al., 2013).

In the second uplift phase (74.0 – 6.5 Ma), the ongoing oblique oceanic lithospheric subduction from continued convergence between Africa and Eurasia resulted in the 90^{o} counterclockwise rotation of the Troodos ophiolite during the Late Campanian-Maastrichtian until the Eocene (McPhee and van Hinsbergen, 2019; Robertson, 1998a), decreasing uplift rates to 0.02 km/Myr (table 5.5). In combination with the reduced northward movement of Africa with respect to Eurasia (McPhee and van Hinsbergen, 2019; Reilinger et al., 2015; Robertson, 1998a) and obtained paleomagnetic data, uplift appears to be gradual lacking any distinguishable significant uplift phase until the middle Miocene (Morag et al., 2016; Robertson, 1977), when the Eratosthenes Seamount started to underthrust, likely increasing uplift rates towards the end of the Miocene (Khair and Tsokas, 1999; Robertson, 1998a).

From our field analysis, we can correlate the underthrusting of the Eratosthenes Seamount below the ophiolite to the third uplift phase that lasts from the late Miocene – early Pliocene uplift. During this period, the Nicosia Formation (5.2 – 2.5 Ma) was deposited and uplift rates increased to 0.69 km/Myr (table 5.5). Furthermore, the subduction zone located south of Cyprus is revived during this period and the dormant Cyprian arc is reactivated by the slab break off (Morag et al., 2016). Consequently, the third uplift phase reached its peak only post-late Miocene at the end of the Nicosia Formation (Morag et al., 2016).

The relatively tectonic stable uplift phases are replaced by significant uplift rate acceleration during the fourth uplift phase to 2.78 – 10.46 km/Myr (table 5.5) when the Kakkaristra (2.5 – 2.0 Ma) conglomerate was deposited (Robertson, 1977). Since the Pliocene (< 2.58 Ma), serpentinization is triggered by the reactivated subduction zone introducing hydrating fluids (Robertson, 1977), announcing the fourth uplift phase. The formed serpentinite diapir exhumes deep-seated plutonic and mantle rocks in the center of the Troodos massif by normal faulting and diapiric uplift, resulting in the dome-shaped structure (Morag et al., 2016; Robertson, 1977). Hence, the Troodos ophiolite became subaerially exposed since 2 Ma (Ring and Pantazides, 2019; Robertson, 1998a). Since the Late Pleistocene, subduction velocities slowed down towards 6 to 10 mm/year (Saleh, 2013; Symeou et al., 2017), resulting in negligible compressional forces. Both the subaerial exposure and negligible compressional forces resulted in an erosional phase during the deposition of the Fanglomerate Formation (1.8 – 0.01 Ma). Nevertheless, the Pleistocene uplift mechanism is obscure and still an ongoing debate (Robertson, 1977).

Chapter 6 Conclusion

6.1 Main conclusions

In conclusion, nine lithosphere-scale numerical models simulating topography during the Troodos ophiolite obduction event combined with field observations of the sedimentary cover enabled me to assess and answer the main research question: '*What type of lithosphere subducted underneath the Troodos ophiolite during obduction and how did the subsequent uplift history lead to its subaerial exposure?*'. Despite the limitations of our numerical models, i.e. the exclusion of phase changes, internal heterogeneities in the initial lithosphere structure and arbitrary initial boundary conditions, this study shows that the subducting plate more likely consists of oceanic lithosphere and I therefore reject the continental and oceanic-continental lithosphere hypotheses. The Troodos ophiolite likely obducted onto an oceanic originated footwall that subducts with a shallow dip angle of 13° until 45 km depth which continues with a ~28° dip angle below 45 km depth and that converges with 2 cm/year, resulting in 3.5 km uplift after 10 Myr. The continental lithosphere hypothesis is rejected, because the continental lithosphere starts to flow instead of simulating subduction due to its multilayered structure and large density and viscosity contrast between the subducting continental and overriding oceanic lithospheres, and the underlying mantle. The remaining three oceanic and all four oceanic-continental lithosphere models are rejected, because more than 5 km uplift is generated in 10 Myr which contradicts field observations.

During fieldwork, the identified clasts within the conglomerates of the Pakhna, Nicosia, Kakkaristra and Fanglomerate Formations, show an increase in clasts from deeper segments of the oceanic crustal sequence with decreasing Formation age. The uplift history of the Troodos ophiolite is constrained by combining the numerical modelling data with field observations, distinguishing four separate uplift phases with associated uplift rates correlating properly with tectonic events occurring in the Eastern Mediterranean and one erosional phase once the Troodos ophiolite exposes subaerial. The first phase lasts from 90 – 80 Ma with an uplift rate op 0.35 km/Myr and coincides with the obduction initiation. The second uplift phase lasts from 74.0 – 6.5 Ma with an uplift rate of 0.02 km/Myr and coincides with the 90° counterclockwise rotation of the Troodos ophiolite in combination with Africa moving slower towards Eurasia. The third uplift phase lasts from 5.2 – 2.5 Ma with an uplift rate of 0.69 km/Myr and coincides with the underthrusting of the Eratosthenes Seamount and reactivation of the subduction zone located south of Cyprus. Consequently, serpentinization accelerated uplift rates significantly announcing the fourth uplift phase lasting from 2.5 – 2.0 Ma, resulting in the subaerial exposure since 2 Ma. The uplift history finishes with an erosional phase due to the subaerial exposure and reduced compressional forces by slower subduction velocities.

6.2 Recommendations

After finishing this Master Thesis, there are several recommendations and prospects for following-up research, divided in numerical modelling limitations, model parameters and fieldwork, described in the section below.

Apart from the limitations of the numerical models mentioned in '*Chapter 5.3 Correlating numerical modelling and field observational data*', the results from the performed lithosphere-scale numerical models are also affected by numerical limitations that include a limited resolution of the numerical grid due to limited computing power. Furthermore, lateral variations are ignored in the 2D numerical models, affecting the result. Most importantly, erosion is not considered in the nine performed lithosphere-scale numerical models. In this Master Thesis, I assumed obduction initiated 90 Ma on the ocean floor, remaining the following 10 Myr below sea level and stopped 80.0 Ma under water before the deepwater sedimentary chalks from the Lefkara Formation were deposited 74.0 Ma enabling the exclusion of the erosion parameter. Nevertheless, once the ophiolite becomes subaerial during obduction in the period from 90.0 – 80.0 Ma, erosion and weathering will affect the height of the collisional high generated in the numerical models. By including erosion into the models, the expectation is that the topographic highs become lower compared to the described model results in '*Chapter 4.1 Numerical modelling*', resulting in more possible subduction settings, indicating less rejected models and probably more possible footwall natures on which the Troodos ophiolite obducted.

Secondly, two model parameters are uncertain, namely the subduction velocity and plate length. The data set becomes more accurate and complete by performing an additional set of numerical models varying the uncertain parameters intensively. The subduction velocity is uncertain, because the actual convergence velocity between Africa and Eurasia during obduction initiation in the middle to early Late Cretaceous was not obtained from the literature. The used subduction velocities of 2 – 3 cm/year are based on convergence slowing down to 14 mm/year since 25 Ma (Reilinger et al., 2015) combined with present day convergence velocities of 6 to 10 mm/year. Based on the deceleration, I interpreted higher subduction velocities in the past. The second uncertain parameter is the plate length. The used plate lengths in the performed numerical models are randomly estimated, because before reading the paper of Crameri et al. (2017) the impact of this parameter on the results was unknown. Apparently, the slab buoyancy depends on slab thickness and its length (Crameri et al., 2017) affecting the generated amount of convection-induced topography, the height of the forebulge and collisional high, trench depth and the geometry of the subsided area behind the collisional high. In addition, Xue et al. (2020) show that the subducting plate length affects the slab geometry and kinematic style in a subduction system, including trench movement, either retreating or advancing, affecting the partitioning subduction velocity into the trench velocity and subduction plate velocity (Xue et al., 2020). The presented numerical modelling data set in this report does not contain the plate length parameter. In future research, it is recommended to do an intensive literature review, obtaining accurate subduction velocities during obduction initiation in the middle to early Late Cretaceous and precise plate lengths of both the downgoing and overriding plates, based on the distance from the subduction zone to the African margin and the accurate length of Cyprus, respectively.

Lastly, during fieldwork clasts within the conglomerates having a size > 2 cm were classified and investigated. Consequently, the abundance of each individual sedimentary formation and/or oceanic crustal unit within the conglomerates of the Pakhna, Nicosia, Kakkaristra and Fanglomerate Formations are based on the clasts having a size > 2 cm, whereas possible present mantle material in an outcrop having a size < 2 cm is missed during this research. The mantle exposures that we analyzed in the field consisted of large, relatively fragile rocks, which implies that larger clasts may have eroded and weathered easily to < 2 cm large clasts. In future research, it is recommended to intensively identify clasts having a size > 2 cm but also < 2 cm, to ensure that smaller clasts of ultramafic mantle material are present or absent from the different conglomerate deposits.

Acknowledgement

This Master Thesis is written as graduation assignment for the Master Earth Science at the Vrije University of Amsterdam. The project was mainly executed from home in the period from the 6th of February till the 31st of July 2023, with a short fieldtrip to Cyprus from the 2nd till 14th of May and obtaining data from the optical microscopy at the Vrije University Amsterdam on the 3rd of July. I would like to thank Anouk Beniest for offering this master thesis and guiding me. Furthermore, I would like to thank Richard Wessels, Demi Schutte and Anke van Grieken who joined me during the fieldwork in Cyprus for their enjoyable cooperation. Additionally, I would like to thank Vasilis Symeou from the Geological Survey of Cyprus for joining us in the field and providing access to specific literature, Bouke Lancet for preparing my thin section and Wouter Schellart as second assessor for checking this Master Thesis enabling me to graduate.

References

Abelson, M., Baer, G. and Agnon, A. (2001) Evidence from gabbro of the Troodos ophiolite for lateral magma transport along a slow-spreading mid-ocean ridge. *Nature*, **409,** 72-5.
Agard, P., Jolivet, L., Vrielynck, B., Burov, E. and Monie, P. (2007) Plate acceleration: The obduction trigger? *ScienceDirect*, **258,** 428-441.
Beniest, A., Koptev, A. and Burov, E. (2017) Numerical models for continental break-up: Implications for the South Atlantic. *Earth and Planetary Science Letters*, **461,** 176-189.
Brookfield, M.E. (1977) The emplacement of giant ophiolite nappes I. Mesozoic—Cenozoic examples. *Tectonophysics*, **37,** 247-303.
Burov, E.B. (2011) Rheology and strength of the lithosphere. *Marine and Petroleum Geology*, **28,** 1402-1443.
Capitanio, F.A., Morra, G. and Goes, S. (2007) Dynamic models of downgoing plate-buoyancy driven subduction: Subduction motions and energy dissipation. *Earth and Planetary Science Letters*, **262,** 284-297.
Chen, G. and Robertson, A.H.F. (2019) Provenance and magmatic-tectonic setting of Campanian-aged volcaniclastic sandstones of the Kannaviou Formation in western Cyprus: Evidence for a South-Neotethyan continental margin volcanic arc. *Sedimentary Geology*, **388,** 114-138.
Clube, T.M.M., Creer, K.M. and Robertson, A.H.F. (1985) Palaeorotation of the Troodos microplate, Cyprus. *Nature*, **317,** 522-525.
Clube, T.M.M. and Robertson, A.H.F. (1986) The palaeorotation of the troodos microplate, cyprus, in the late mesozoic-early cenozoic plate tectonic framework of the Eastern Mediterranean. *Surveys in Geophysics : An International Review Journal Covering the Entire Field of Geosciences and Related Areas*, **8,** 375-437.
Crameri, F., Lithgow-Bertelloni, C.R. and Tackley, P.J. (2017) The dynamical control of subduction parameters on surface topography. *Geochemistry, Geophysics, Geosystems*, **18,** 1661-1687.
Dilek, Y. and Flower, M.F.J. (2003) Arc-trench rollback and forearc accretion: 2. A model template for ophiolites in Albania, Cyprus, and Oman. *Geological Society, London, Special Publications*, **218,** 43-68.
Dilek, Y. and Thy, P. (1990) Tectonic evolution of the Troodos ophiolite within the Tethyan framework. *Tectonics*, **9,** 811.
Duretz, T., Agard, P., Yamato, P., Ducassou, C., Burov, E.B. and Gerya, T.V. (2016) Thermo-mechanical modeling of the obduction process based on the Oman Ophiolite case. *Gondwana Research*, **32,** 1-10.
Eaton, S. and Robertson, A. (1993) The Miocene Pakhna Formation, southern Cyprus and its relationship to the Neogene tectonic evolution of the eastern Mediterranean. *Sedimentary Geology*, **86,** 273-296.
Eppelbaum, L., Ben-Avraham, Z., Katz, Y., Cloetingh, S. and Kaban, M. (2020) Combined Multifactor Evidence of a Giant Lower-Mantle Ring Structure below the Eastern Mediterranean. *Positioning*, **11,** 11-32.
Ergün, M., Okay, S., Sari, C., Oral, E.Z., Ash, M., Hall, J. and Miller, H. (2005) Gravity anomalies of the Cyprus Arc and their tectonic implications. *Marine Geology*, **221,** 349-358.
Evans, A.D., Teagle, D.A.H., Craw, D., Henstock, T.J. and Falcon-Suarez, I.H. (2021) Uplift and Exposure of Serpentinized Massifs: Modeling Differential Serpentinite Diapirism and Exhumation of the Troodos Mantle Sequence, Cyprus. *Journal of Geophysical Research: Solid Earth*, **126**.
Federal Geographic Data Committee (2006) 37 - Lithological patterns *FGDC Digital Cartographic Standard for Geologic Map Symbolization*, **FGDC Document Number FGDC-STD-013-2006,** A-37-1 to A-37-3.
Feld, C., Mechie, J., Hübscher, C., Hall, J., Nicolaides, S., Gurbuz, C., Bauer, K., Louden, K. and Weber, M. (2017) Crustal structure of the Eratosthenes Seamount, Cyprus and S. Turkey from an amphibian wide-angle seismic profile. *Tectonophysics*, **700-701,** 32-59.
Follows, E.J. (1990) *Sedimentology and tectonic setting of miocene reef and related sediments in Cyprus*, University of Edinburgh Edinburgh.

Gaieb, S. and Jallouli, C. (2017) New overview of the neotectonic and seismotectonic studies in Tunisian domains. *Arabian Journal of Geosciences*, **10,** 1-11.
Garzanti, E., Andò, S. and Scutellà, M. (2000) Actualistic Ophiolite Provenance: The Cyprus Case. *The Journal of Geology*, **108,** 199-218.
Gass, I.G. (1977) Origin and emplacement of ophiolites. *Geological Society, London, Special Publications*, **7,** 72-76.
Gass, I.G., MacLeod, C.J., Murton, B.J., Panayiotou, A., Simonian, K.O., Xenophontos, C., Adamides, N.G., Allerton, S. and Georgiou, E. (1994) *The geology of the southern Troodos transform fault zone*. Geological Survey Department, Ministry of Agriculture, Natural Resources and Environment, Nicosia.
Goetze, C. and Evans, B. (1979) Stress and temperature in the bending lithosphere as constrained by experimental rock mechanics. *Geophysical Journal International*, **59,** 463-478.
Google Earth (2023) "Cyprus". *36°10'38.48"N 28°17'15.28"E*, 14-12-2015. 09-03-2023.
Harrison, R.W. (2008) A model for the plate tectonic evolution of the eastern Mediterranean region that emphasizes the role of transform (strike-slip) structures. In: *Environmental and Geoscience* (Eds A. De Santis, R. Baker, B. Klug, P. Vanicek, L.J.H. D'El-Rey Silva, A. Foyo, M. Ercanoglu and D. Dordevic). WSEAS Press, Malta.
Hermann, J., Zheng, Y. and Rubatto, D. (2013) Deep fluids in subducted continental crust. *Elements*, **9,** 281-287.
Hirth, G. and Kohlstedt, D.L. (1996) Water in the oceanic upper mantle: implications for rheology, melt extraction and the evolution of the lithosphere. *Earth and Planetary Science Letters*, **144,** 93-108.
Jenkyns, H.C. and Winterer, E.L. (1982) Palaeoceanography of Mesozoic ribbon radiolarites. *Earth and Planetary Science Letters*, **60,** 351-375.
Jolivet, L., Faccenna, C., Agard, P., De Lamotte, D.F., Menant, A., Sternai, P. and Guillocheau, F. (2016) Neo-Tethys geodynamics and mantle convection: from extension to compression in Africa and a conceptual model for obduction. *Canadian Journal of Earth Sciences*, **53,** 1190-1204.
Karato, S., Paterson, M.S. and FitzGerald, J.D. (1986) Rheology of synthetic olivine aggregates: Influence of grain size and water. *Journal of Geophysical Research: Solid Earth*, **91,** 8151-8176.
Khair, K. and Tsokas, G.N. (1999) Nature of the Levantine (eastern Mediterranean) crust from multiple-source Werner deconvolution of Bouguer gravity anomalies. *Journal of Geophysical Research: Solid Earth*, **104,** 25469-25478.
Kinnaird, T.C., Robertson, A.H.F. and Morris, A. (2011) Timing of uplift of the Troodos Massif (Cyprus) constrained by sedimentary and magnetic polarity evidence. *Journal of the Geological Society of London*, **168,** 457-470.
Krijgsman, W., Hilgen, F.J., Raffi, I., Sierro, F.J. and Wilson, D.S. (1999) Chronology, causes and progression of the Messinian salinity crisis. *NATURE -LONDON-*, 652-654.
Lallemand, S. and Funicello, F. (2009) Subduction Zones Geodynamics, *Frontiers in Earth Sciences*. Springer, Berlin.
Lau, K.W.H., Watremez, L., Louden, K.E. and Nedimovíć, M.R. (2015) Structure of thinned continental crust across the Orphan Basin from a dense wide-angle seismic profile and gravity data. *Geophysical Journal International*, **202,** 1969-1992.
Le Pourhiet, L., Burov, E. and Moretti, I. (2004) Rifting through a stack of inhomogeneous thrusts (the dipping pie concept). *Tectonics*, **23**.
Longiaru, S. (1987) Visual comparators for estimating the degree of sorting from plane and thin section. *Journal of Sedimentary Research*, **57**.
Luccio, F.D. and Pasyanos, M.E. (2007) Crustal and upper-mantle structure in the Eastern Mediterranean from the analysis of surface wave dispersion curves. *Geophysical Journal International*, **169,** 1139-1152.
Mackwell, S.J., Zimmerman, M.E. and Kohlstedt, D.L. (1998) High-temperature deformation of dry diabase with application to tectonics on Venus. *Journal of Geophysical Research: Solid Earth*, **103,** 975-984.

Maffione, M., Hinsbergen, D.J.J., Gelder, G.I.N.O., Goes, F.C. and Morris, A. (2017) Kinematics of Late Cretaceous subduction initiation in the Neo-Tethys Ocean reconstructed from ophiolites of Turkey, Cyprus, and Syria. *Journal of Geophysical Research: Solid Earth*, **122,** 3953-3976.
McCallum, J.E. (1989) *Sedimentation and tectonics of the Plio-Pleistocene of Cyprus*.
McCallum, J.E. and Robertson, A.H.F. (1995) Sedimentology of two fan-delta systems in the Pliocene-Pleistocene of the Mesaoria Basin, Cyprus. *Sedimentary Geology*, **98,** 215-244.
McPhee, P.J. and van Hinsbergen, D.J.J. (2019) Tectonic reconstruction of Cyprus reveals Late Miocene continental collision of Africa and Anatolia. *Gondwana Research*, **68,** 158-173.
Morag, N., Haviv, I. and Katzir, Y. (2016) From ocean depths to mountain tops: Uplift of the Troodos ophiolite (Cyprus) constrained by low-temperature thermochronology and geomorphic analysis. *Tectonics*, **35,** 622-637.
Papanikolaou, D. (2010) Major paleogeographic, tectonic and geodynamic changes from the last stage of the Hellenides to the actual Hellenic arc and trench system. *Bulletin of the Geological Society of Greece*, **43,** 72-85.
Papanikolaou, D.I. (2021) The Mediterranean. In: *The Geology of Greece* (Ed D.I. Papanikolaou), pp. 25-44. Springer International Publishing, Cham.
Payne, A.S. and Robertson, A.H.F. (1995) Neogene supra-subduction zone extension in the Polis Graben system, West Cyprus. *Journal of the Geological Society of London***,** 613.
Poole, A. and Robertson, A. (1998) Pleistocene fanglomerate deposition related to uplift of the Troodos Ophiolite, Cyprus. *Proceedings - Ocean Drilling Program Scientific Results***,** 545-568.
Porkoláb, K., Duretz, T., Yamato, P., Auzemery, A. and Willingshofer, E. (2021) Extrusion of subducted crust explains the emplacement of far-travelled ophiolites. *Nature Communications*, **12**.
Powers, M. (1953) A new roundness scale for sedimentary particles. *Journal of Sedimentary Petrology*, **23,** 117-119.
Ranalli, G. (2000) Rheology of the crust and its role in tectonic reactivation. *Journal of geodynamics*, **30,** 3-15.
Ranalli, G. and Murphy, D.C. (1987) Rheological stratification of the lithosphere. *Tectonophysics*, **132,** 281-295.
Reilinger, R., McClusky, S. and ArRajehi, A. (2015) Geodetic Constraints on the Geodynamic Evolution of the Red Sea. In: *The Red Sea : The Formation, Morphology, Oceanography and Environment of a Young Ocean Basin*, *Springer Earth System Sciences 2197-960X*, pp. 135-149. Berlin, Heidelberg : Springer Berlin Heidelberg : Springer.
Ring, U. and Pantazides, H. (2019) The Uplift of the Troodos Massif, Cyprus. *Tectonics*, **38,** 3124-3139.
Robertson, A. (2004) Development of concepts concerning the genesis and emplacement of Tethyan ophiolites in the Eastern Mediterranean and Oman regions. *Earth-Science Reviews*, **66,** 331-387.
Robertson, A. and Xenophontos, C. (1993) *Development of concepts concerning the Troodos ophiolite and adjacent units in Cyprus*. Geological Society, London.
Robertson, A.H.F. (1977) Tertiary uplift history of the Troodos Massif, Cyprus. *Geological Society of America Bulletin*, **88,** 1763-1772.
Robertson, A.H.F. (1998a) Mesozoic-Tertiary tectonic evolution of the easternmost Mediterranean area: integration of marine and land evidence. *Proceedings of the Ocean Drilling Program, Scientific Results, Vol. 160; Chapter 54*.
Robertson, A.H.F. (1998b) Tectonic significance of the Eratosthenes Seamount: a continental fragment in the process of collision with a subduction zone in the eastern Mediterranean (Ocean Drilling Program Leg 160). *Tectonophysics*, **298,** 63-82.
Robinson, P.T., Malpas, J. and Xenophontos, C. (2003) The Troodos Massif of Cyprus: Its role in the evolution of the ophiolite concept. *Y. Dilek & S. Newcomb (eds): Ophiolite concept and the evolution of geological thought*, **Geol. Soc. A., Spec. Pap. 373**.
Saleh, S. (2013) 3D Crustal and Lithospheric Structures in the Southeastern Mediterranean and Northeastern Egypt. *Pure and Applied Geophysics*, **170,** 2037-2074.

Schirmer, W., Weber, J., Bachtadse, V., BouDagher-Fadel, M., Heller, F., Lehmkuhl, F., Panayides, I. and Schirmer, U. (2010) Fluvial stacking due to plate collision and uplift during the Early Pleistocene in Cyprus. In: *Open Geosciences*, **2**, pp. 514-523.
Schuiling, R.D. (2011) Troodos: A giant serpentinite diapir. *International Journal of Geosciences*, **2,** 98.
Searle, M.P. and Malpas, J. (1980) Structure and metamorphism of rocks beneath the Semail ophiolite of Oman and their significance in ophiolite obduction. *Earth and Environmental Science Transactions of the Royal Society of Edinburgh*, **71,** 247-262.
Searle, M.P. and Stevens, R.K. (1984) *Obduction processes in ancient, modern and future ophiolites*. [s.n.], Oxford ;.
Shelton, A.W. (1993) Troodos revisited: the Mount Olympus gravity anomaly. *Geological Society, London, Special Publications*, **76,** 197-212.
Stoneley, R. (1975) On the origin of ophiolite complexes in the southern Tethys region. *Tectonophysics*, **25,** 303-322.
Symeou, V., Homberg, C., Nader, F.H., Darnault, R., Lecomte, J. and Papadimitriou, N. (2017) Longitudinal and temporal evolution of the tectonic style along the Cyprus Arc system, assessed through 2D reflection seismic interpretation.
Thy, P. (1987) Magmas and magma chamber evolution, Troodos ophiolite, Cyprus. *Geology*, **15,** 316-319.
Trabucho Alexandre, J.P. (2017) Sediments and Sedimentary Rocks in Hand Specimen. *GEO1-1099 Onderwijslint voorbereiding veldwerk 1*, **ß version 2017/8**.
Twining, K. (1996) Origin of plagiogranite in the Troodos ophiolite, Cyprus. In: *The Ninth Keck Research Symposium in Geology*, pp. 245-248.
Uyeda, S. (1981) Subduction zones and back arc basins - A review. *Geologische Rundschau*, **70,** 552-569.
Van Avendonk, H.J.A., Davis, J.K., Harding, J.L. and Lawver, L.A. (2017) Decrease in oceanic crustal thickness since the breakup of Pangaea. *Nature Geoscience*, **10,** 58-61.
Varga, R.J. (1991) Modes of extension at oceanic spreading centers: evidence from the Solea graben, Troodos ophiolite, Cyprus. *Journal of Structural Geology*, **13,** 517-537.
Varga, R.J. and Moores, E.M. (1985) Spreading structure of the Troodos Ophiolite, Cyprus. *Geology (Boulder)*, **13,** 846-850.
Wacey, D., McLoughlin, N., Saunders, M. and Kong, C. (2014) The nano-scale anatomy of a complex carbon-lined microtube in volcanic glass from the ~ 92 Ma Troodos Ophiolite, Cyprus. *Chemical Geology*, **363,** 1-12.
Weber, J., Schirmer, W., Heller, F. and Bachtadse, V. (2011) Magnetostratigraphy of the Apalós Formation (early Pleistocene): Evidence for pulsed uplift of Cyprus. *Geochemistry, Geophysics, Geosystems*, **12**.
Welford, J.K., Hall, J., Hubscher, C., Reiche, S. and Louden, K. (2015) Crustal seismic velocity structure from Eratosthenes Seamount to Hecataeus Rise across the Cyprus Arc, eastern Mediterranean. *Geophysical Journal International*, **200,** 933-951.
Welland, M.J.P. and Mitchell, A.H.G. (1977) Emplacement of the Oman ophiolite; a mechanism related to subduction and collision. *Geological Society of America Bulletin*, **88,** 1081-1088.
Whitechurch, H., Juteau, T. and Montigny, R. (1984) Role of the Eastern Mediterranean ophiolites (Turkey, Syria, Cyprus) in the history of the Neo-Tethys. *Geological Society, London, Special Publications*, **17,** 301-317.
Xue, K., Schellart, W.P. and Strak, V. (2020) Effect of Plate Length on Subduction Kinematics and Slab Geometry: Insights From Buoyancy-Driven Analog Subduction Models. *Journal of Geophysical Research: Solid Earth*, **125**.
Yamato, P., Agard, P., Burov, E., Le Pourhiet, L., Jolivet, L. and Tiberi, C. (2007) Burial and exhumation in a subduction wedge: Mutual constraints from thermomechanical modeling and natural P-T-t data (Schistes Lustrés, western Alps). *Journal of Geophysical Research: Solid Earth*, **112**.

Yamato, P., Burov, E., Agard, P., Le Pourhiet, L. and Jolivet, L. (2008) HP-UHP exhumation during slow continental subduction: Self-consistent thermodynamically and thermomechanically coupled model with application to the Western Alps. *Earth and Planetary Science Letters*, **271,** 63-74.
Zedde, D.M.A.v.d. and Wortel, M.J.R. (2001) Shallow slab detachment as a transient source of heat at midlithospheric depths. *Tectonics*, **20,** 868-882.
Zheng, Y. (2012) Metamorphic chemical geodynamics in continental subduction zones. *Chemical Geology*, **328,** 5-48.

Appendix A

The phase, topography and strain rate figures and/or graph of all nine models are added below. There is an important remark to mention about all phase, topography and strain rate figures and graph, because the timing above the graph or figure is given in Ma (‘*Million years ago*’). However, this timing indicates the amount of million years (Myr) after the model simulation started. For example, the title ‘@1.5 Ma’ in figures 1, 2, 3; Appendix A.1 shows the phase, topography and strain rate conditions after simulating 1.5 Myr.

Appendix A.1 Model 1 Oceanic lithosphere

<table>
<tr><th>Phases</th><th>Topography</th><th>Strain rate</th></tr>
<tr><td>1 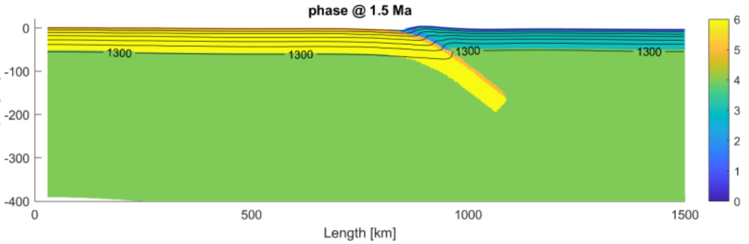</td><td>2 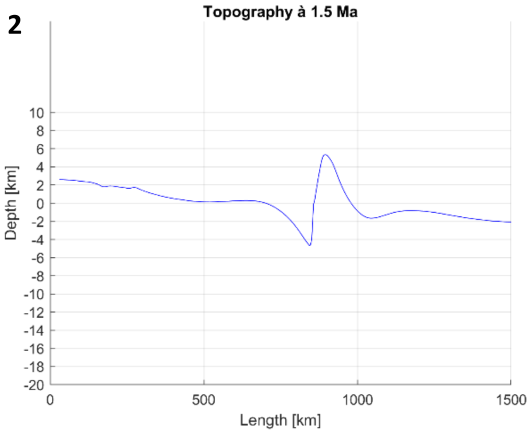</td><td>3 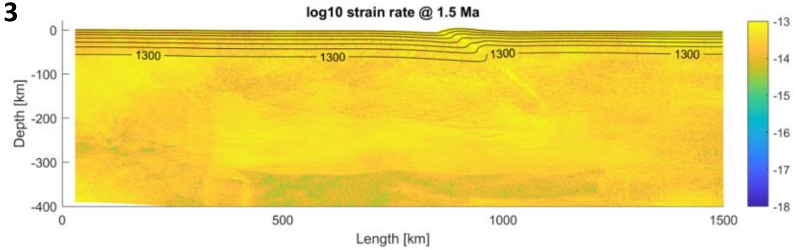</td></tr>
</table>

4

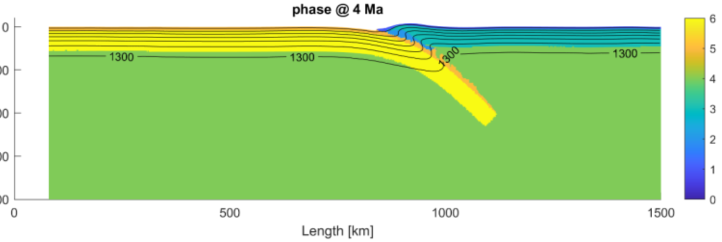
phase @ 4 Ma
Depth [km]
Length [km]

5

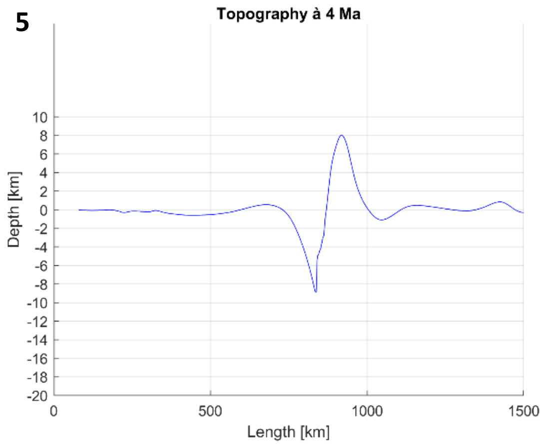
Topography à 4 Ma
Depth [km]
Length [km]

6

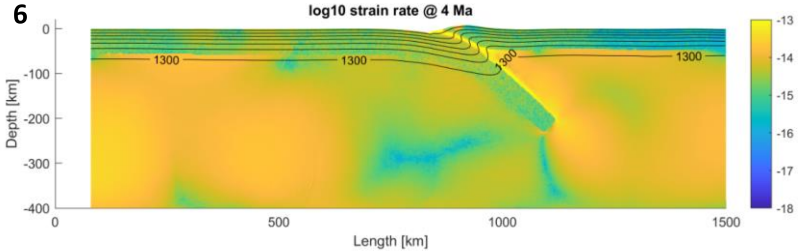
log10 strain rate @ 4 Ma
Depth [km]
Length [km]

7

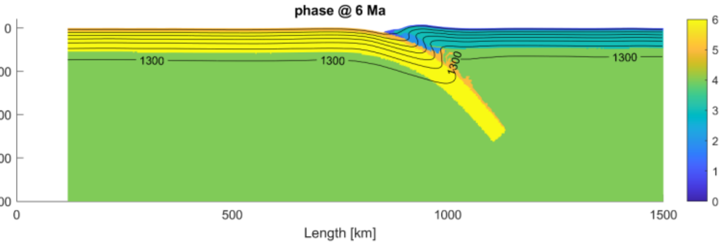
phase @ 6 Ma
Depth [km]
Length [km]

8

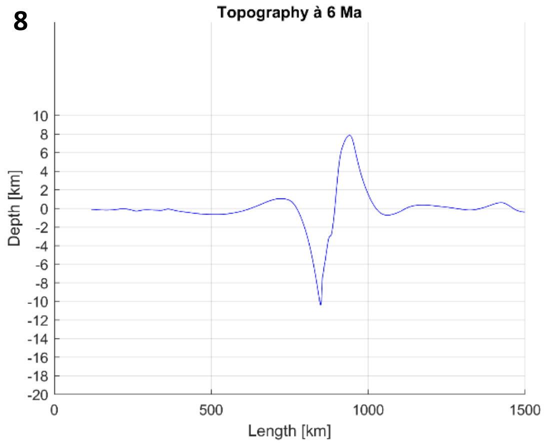
Topography à 6 Ma
Depth [km]
Length [km]

9

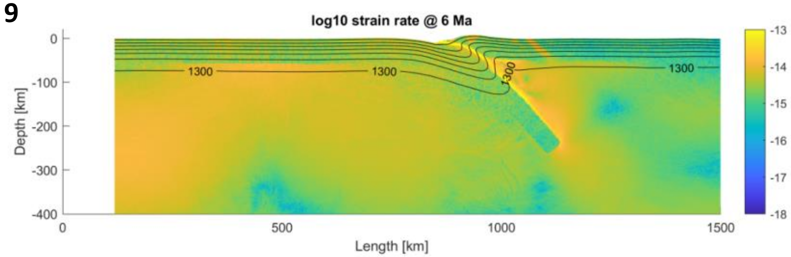
log10 strain rate @ 6 Ma
Depth [km]
Length [km]

10 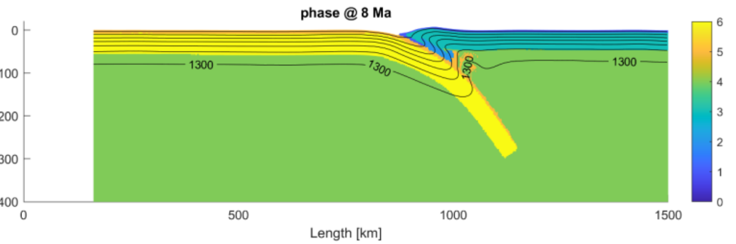	11 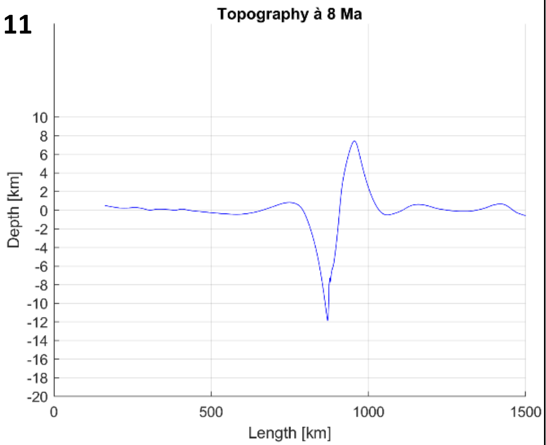	12 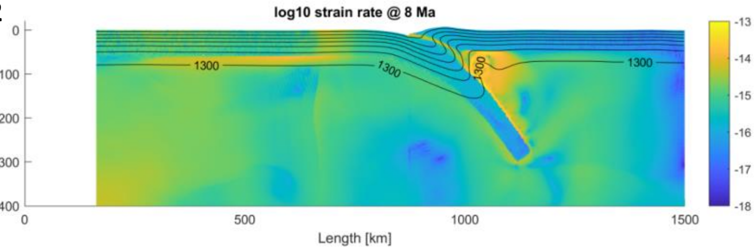
13 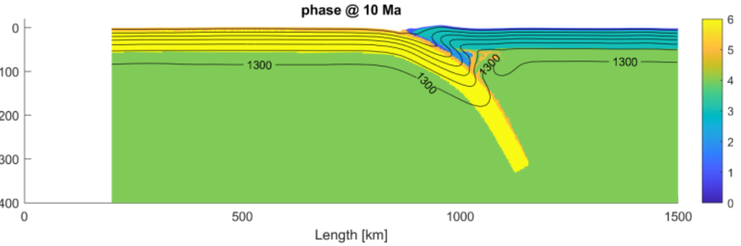	14 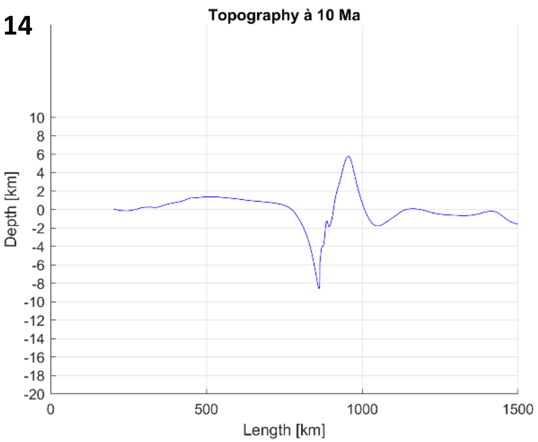	15 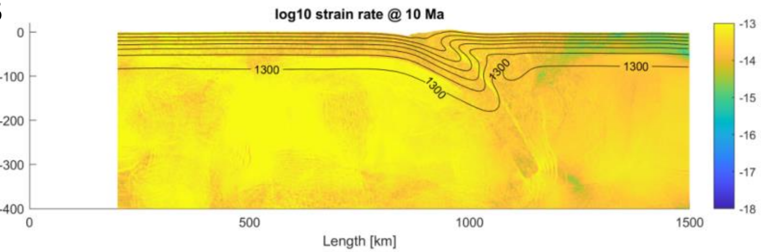

Table A.1 Phase, topography and strain rate results of Model 1.

Appendix A.2 Model 2 Oceanic lithosphere

Phases	Topography	Strain rate

1

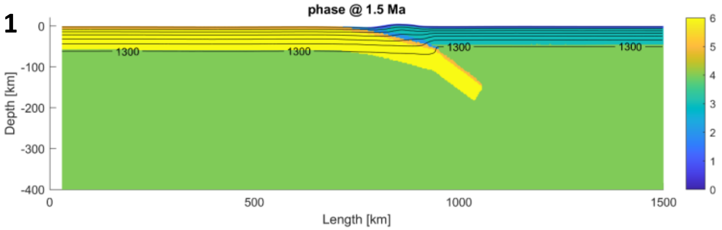

2

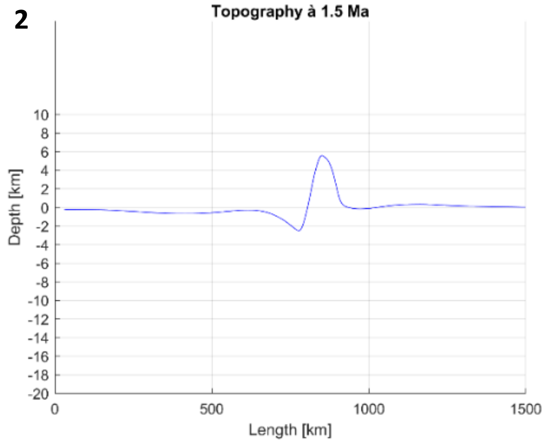

3

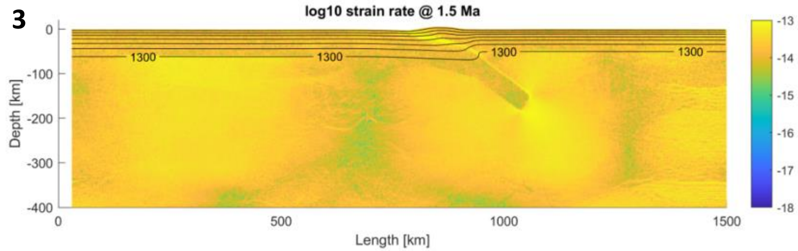

4

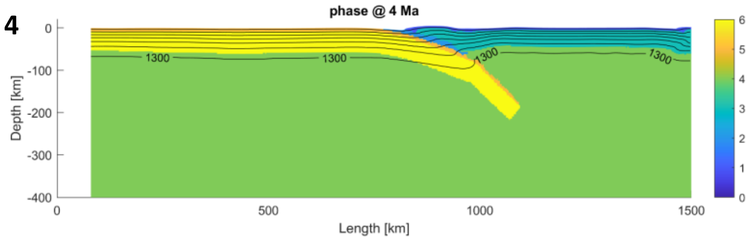

5

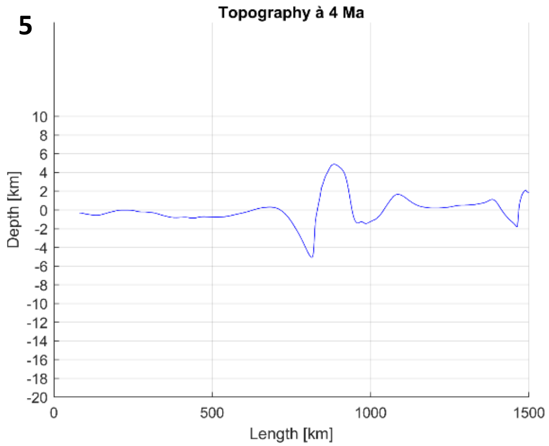

6

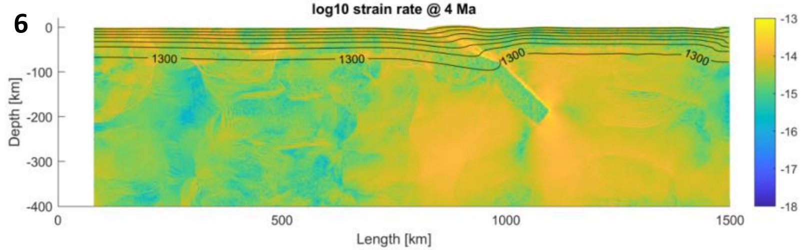

7

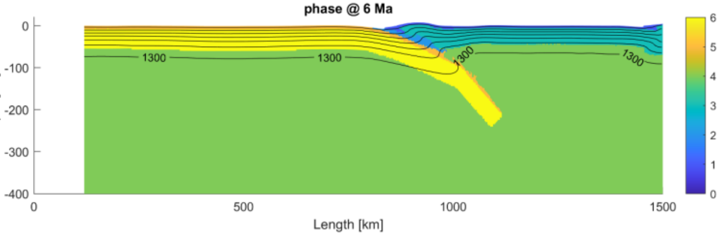
phase @ 6 Ma
Depth [km]
0
-100
-200
-300
-400
0
500
1000
1500
Length [km]
1300
1300
1300
1300
6
5
4
3
2
1
0

8

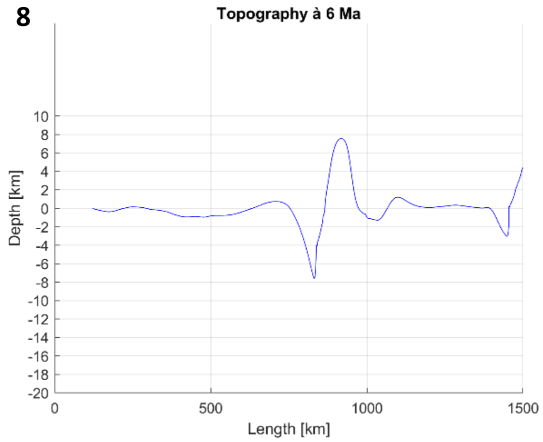
Topography à 6 Ma
Depth [km]
10
8
6
4
2
0
-2
-4
-6
-8
-10
-12
-14
-16
-18
-20
0
500
1000
1500
Length [km]

9

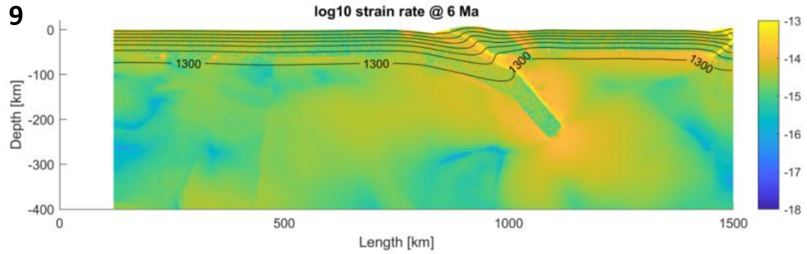
log10 strain rate @ 6 Ma
Depth [km]
0
-100
-200
-300
-400
0
500
1000
1500
Length [km]
1300
1300
1300
1300
-13
-14
-15
-16
-17
-18

10

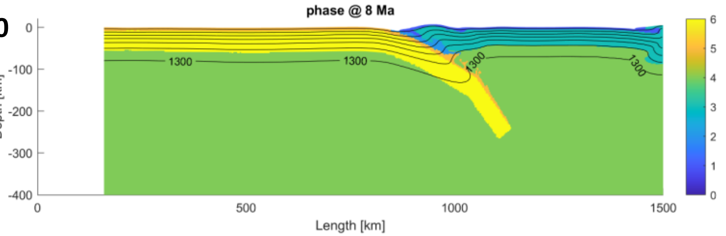
phase @ 8 Ma
Depth [km]
0
-100
-200
-300
-400
0
500
1000
1500
Length [km]
1300
1300
1300
1300
6
5
4
3
2
1
0

11

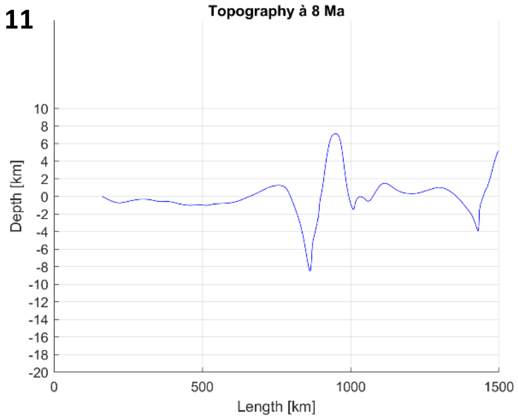
Topography à 8 Ma
Depth [km]
10
8
6
4
2
0
-2
-4
-6
-8
-10
-12
-14
-16
-18
-20
0
500
1000
1500
Length [km]

12

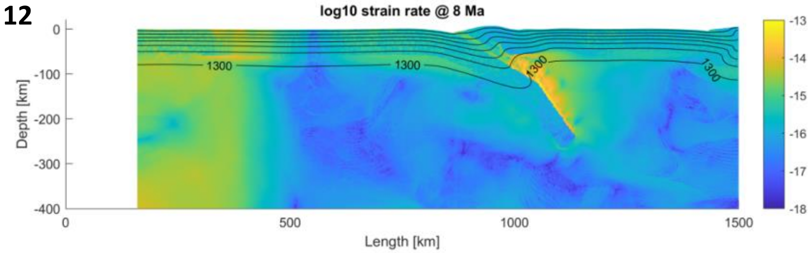
log10 strain rate @ 8 Ma
Depth [km]
0
-100
-200
-300
-400
0
500
1000
1500
Length [km]
1300
1300
1300
1300
-13
-14
-15
-16
-17
-18

13

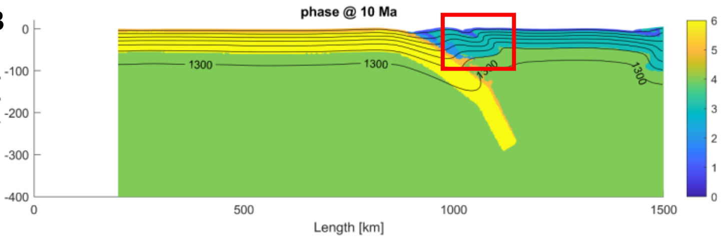

14

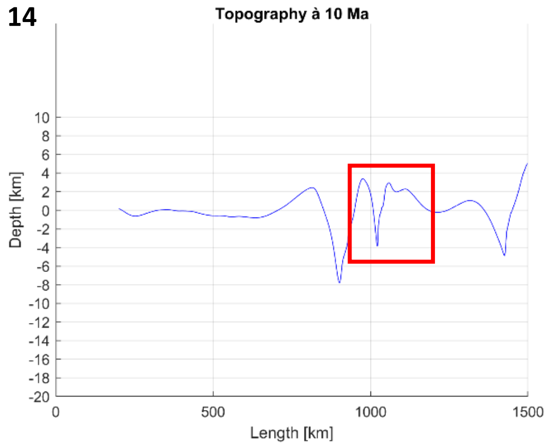

15

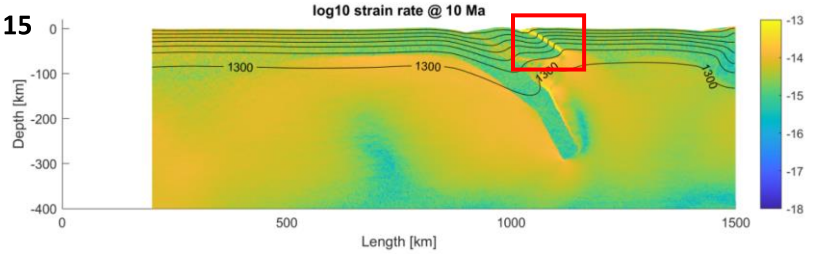

Table A.2 Phase, topography and strain rate results of Model 2.

Appendix A.3 Model 3 Oceanic lithosphere

Phases

1

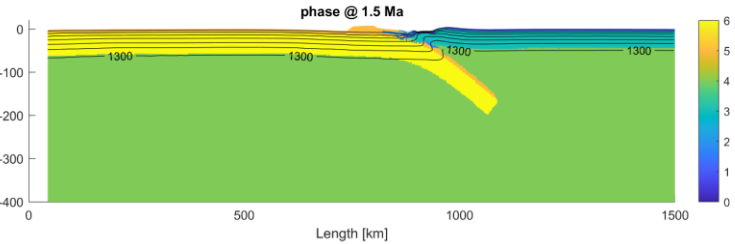

Topography

2

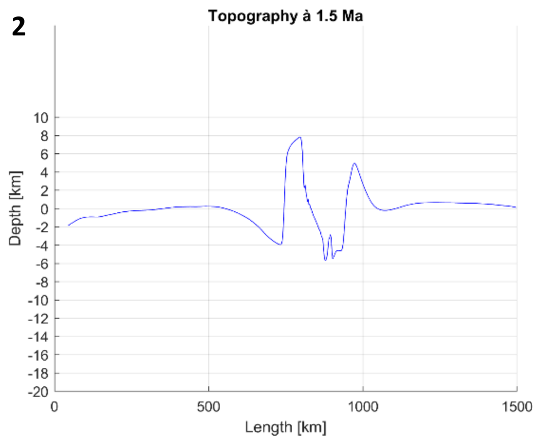

Strain rate

3

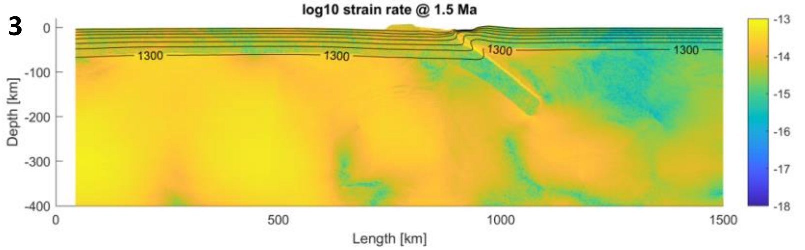

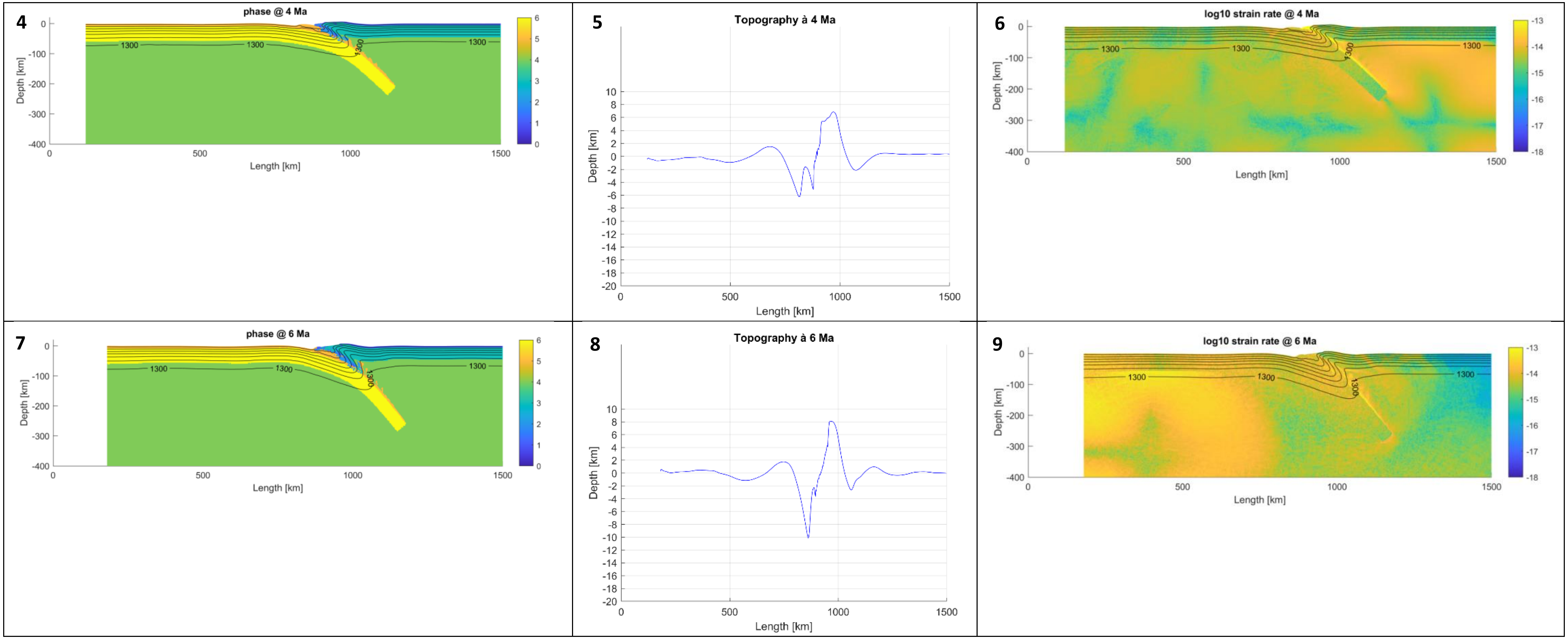
4
phase @ 4 Ma
Depth [km]
Length [km]
1300
5
Topography à 4 Ma
Depth [km]
Length [km]
6
log10 strain rate @ 4 Ma
Depth [km]
Length [km]
1300
7
phase @ 6 Ma
Depth [km]
Length [km]
1300
8
Topography à 6 Ma
Depth [km]
Length [km]
9
log10 strain rate @ 6 Ma
Depth [km]
Length [km]
1300

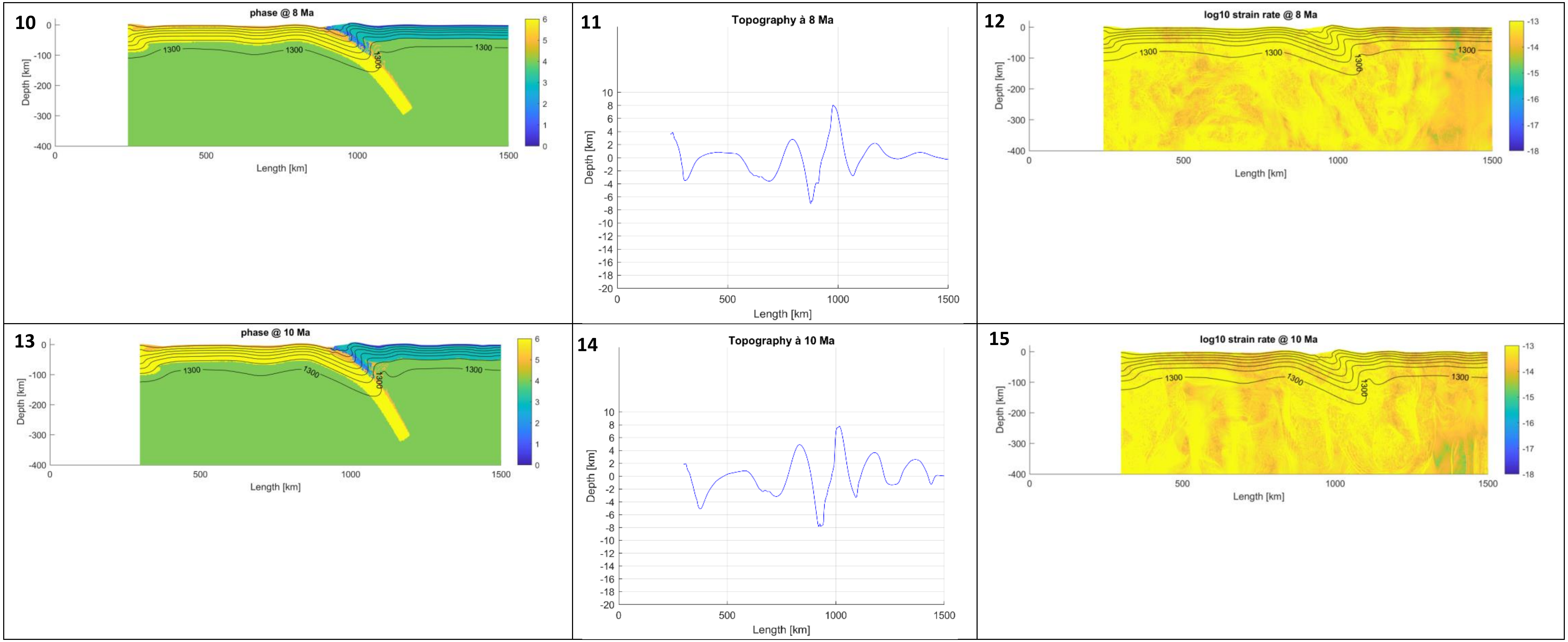

Table A.3 Phase, topography and strain rate results of Model 3.

Appendix A.4 Model 4 Oceanic lithosphere

Phases	Topography	Strain rate

1

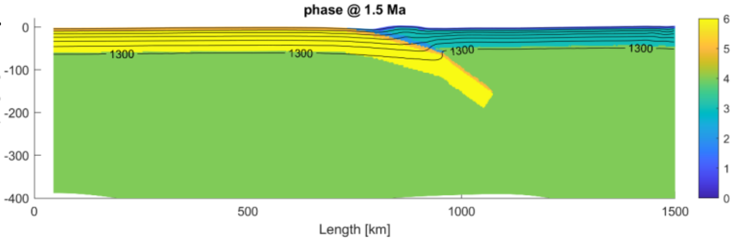

2

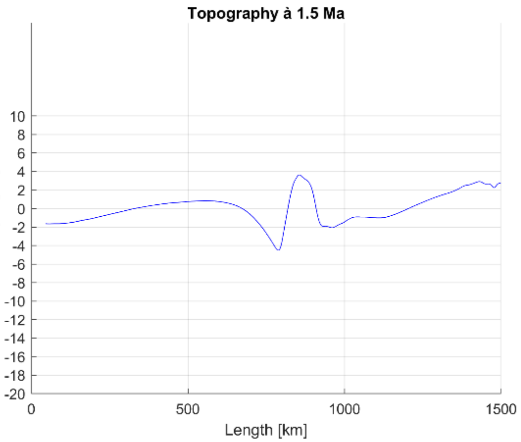

3

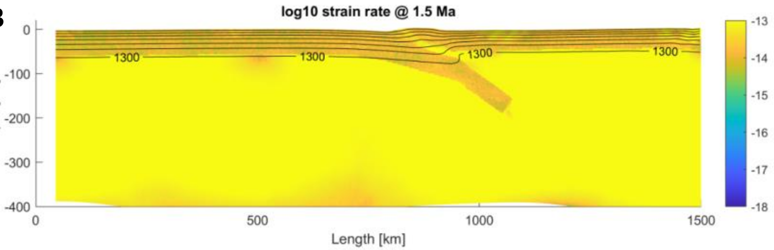

4

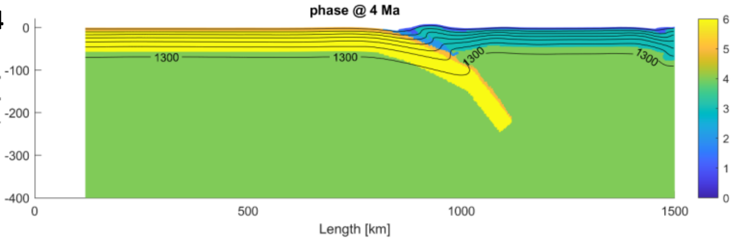

5

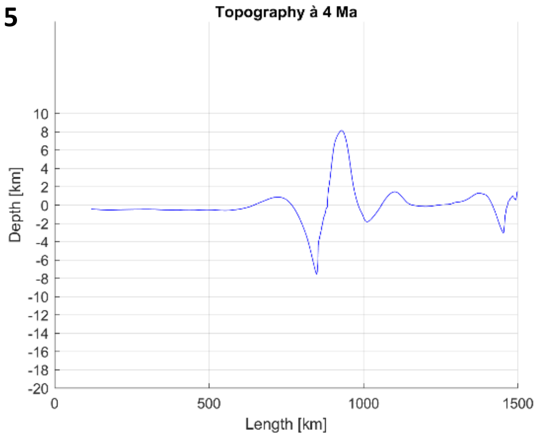

6

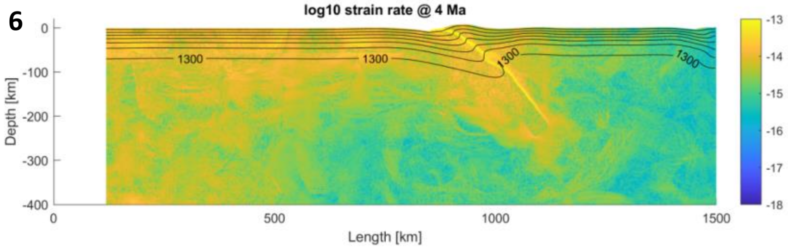

7

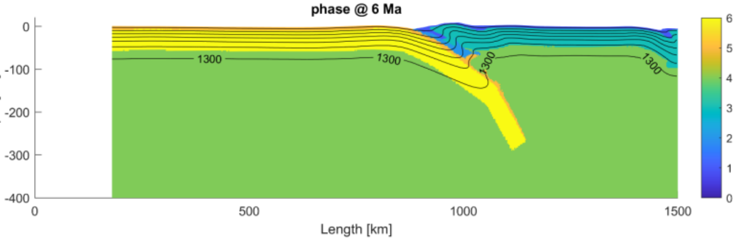
phase @ 6 Ma
Depth [km]
Length [km]
1300

8

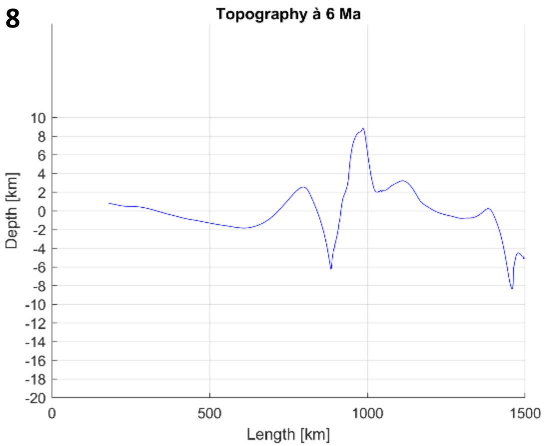
Topography à 6 Ma
Depth [km]
Length [km]

9

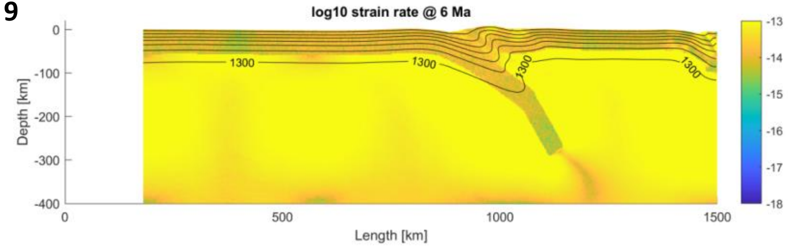
log10 strain rate @ 6 Ma
Depth [km]
Length [km]
1300

10

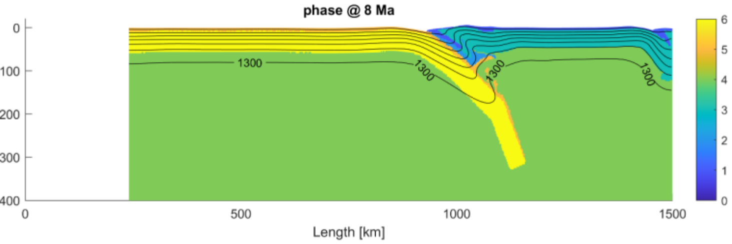
phase @ 8 Ma
Depth [km]
Length [km]
1300

11

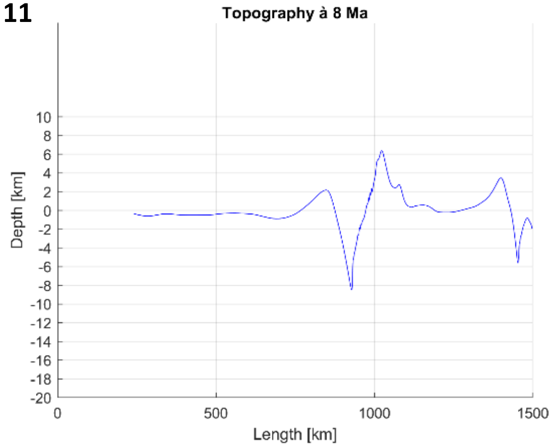
Topography à 8 Ma
Depth [km]
Length [km]

12

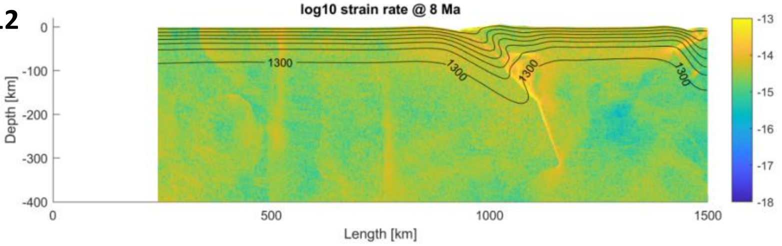
log10 strain rate @ 8 Ma
Depth [km]
Length [km]
1300

13

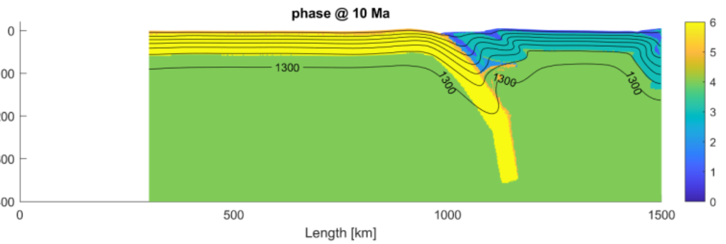

14

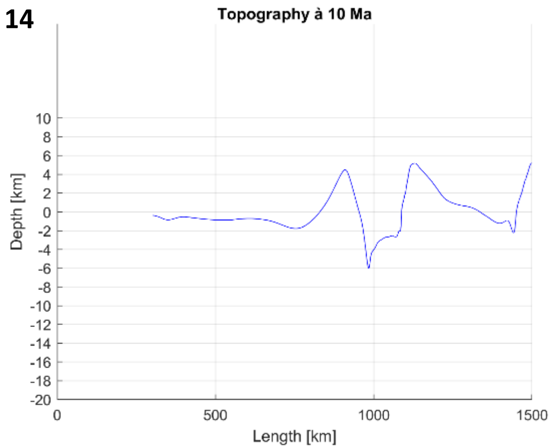

15

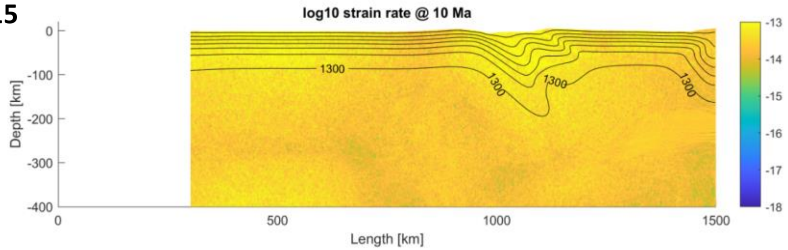

Table A.4 Phase, topography and strain rate results of Model 4.

Appendix A.5 Model 5 Continental lithosphere

Phases	Topography	Strain rate

1

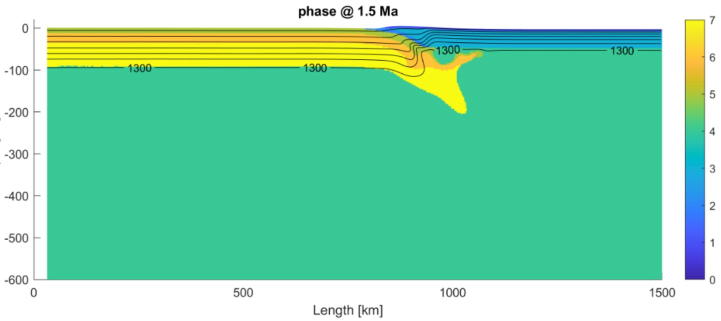

2

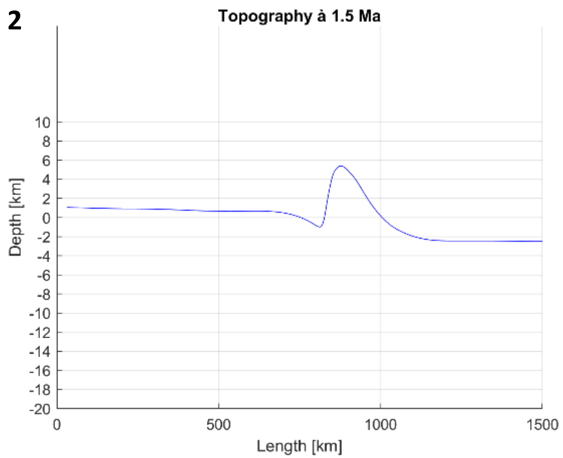

3

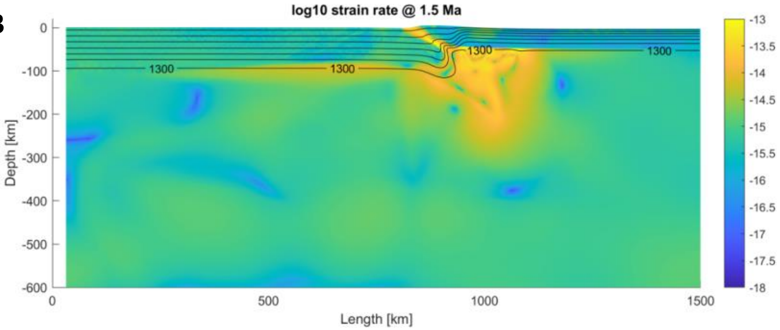

4

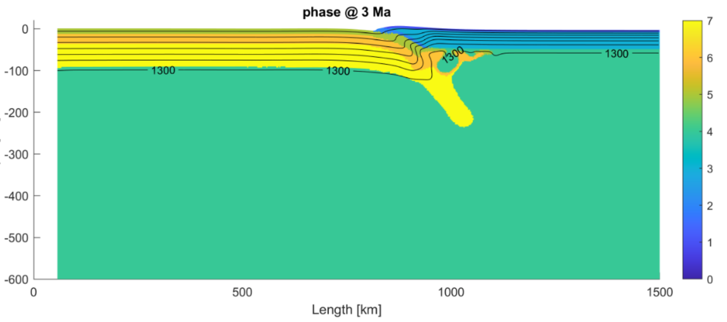
phase @ 3 Ma
Depth [km]
Length [km]
1300

5

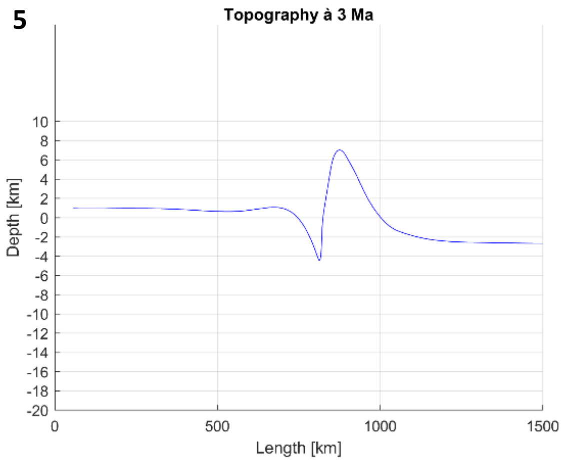
Topography à 3 Ma
Depth [km]
Length [km]

6

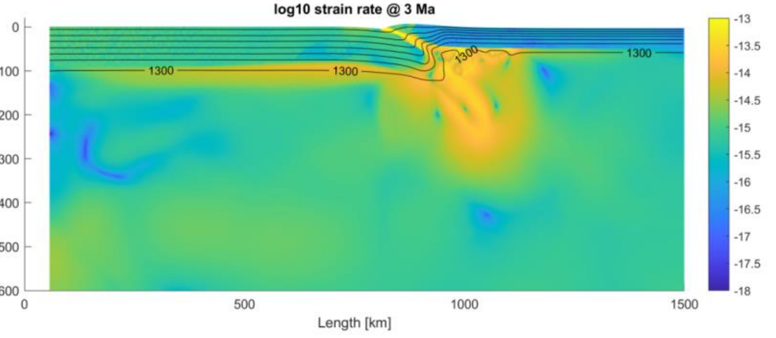
log10 strain rate @ 3 Ma
Depth [km]
Length [km]
1300

7

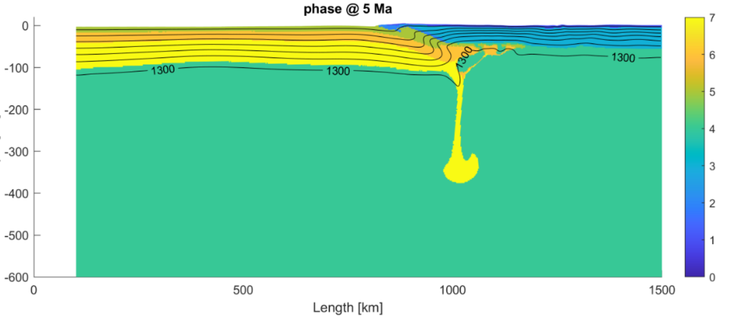
phase @ 5 Ma
Depth [km]
Length [km]
1300

8

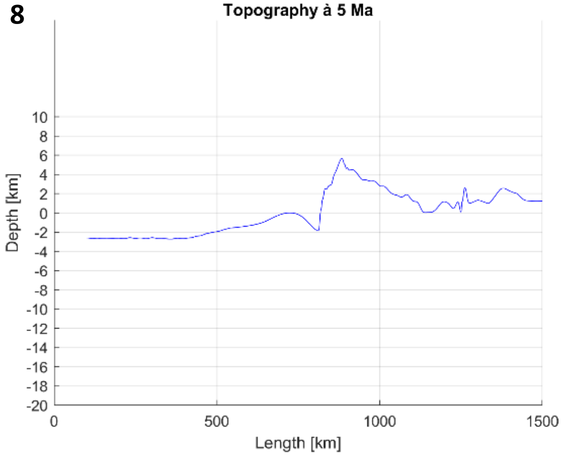
Topography à 5 Ma
Depth [km]
Length [km]

9

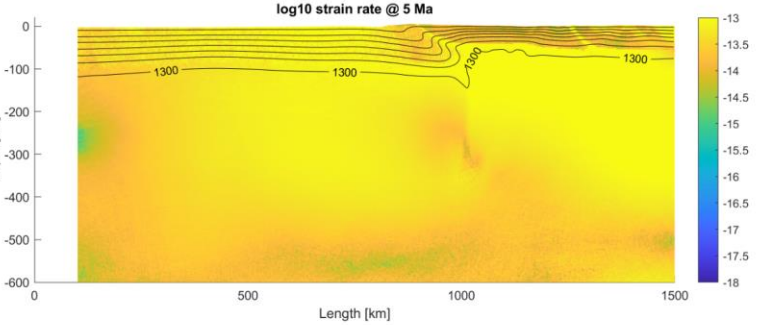
log10 strain rate @ 5 Ma
Depth [km]
Length [km]
1300

10
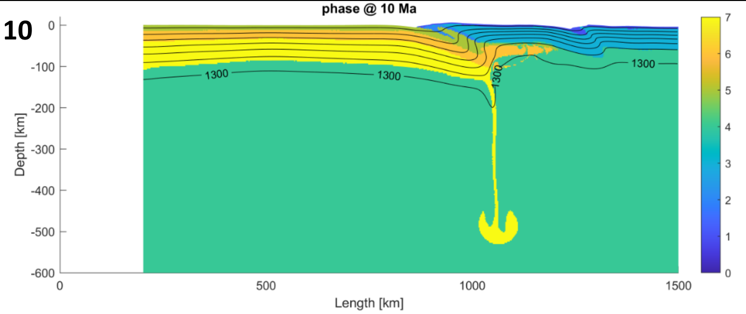

11
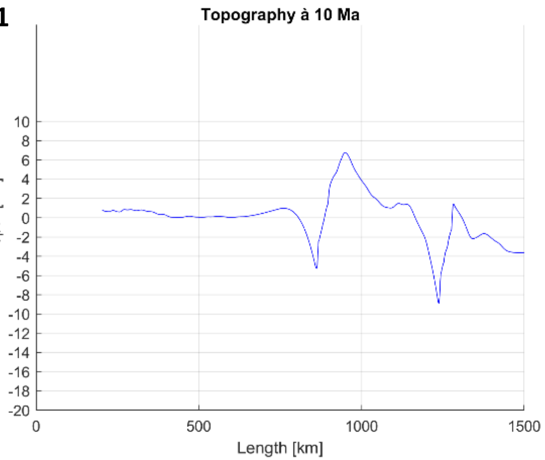

12
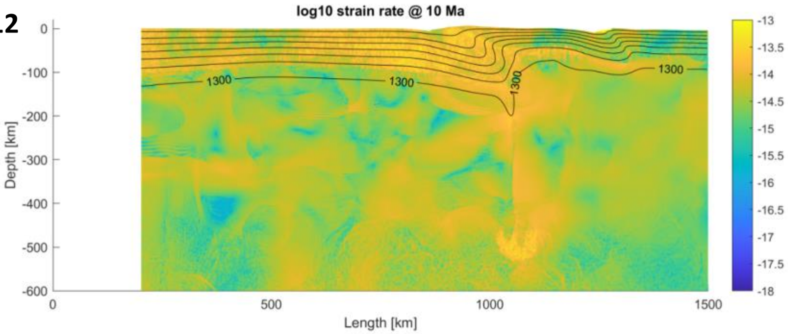

Table A.5 Phase, topography and strain rate results of Model 5.

Appendix A.6 Model 6 Oceanic-continental lithosphere

Phases	Topography	Strain rate

1
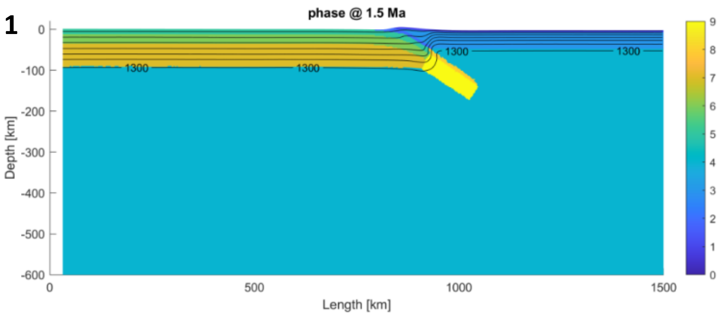

2
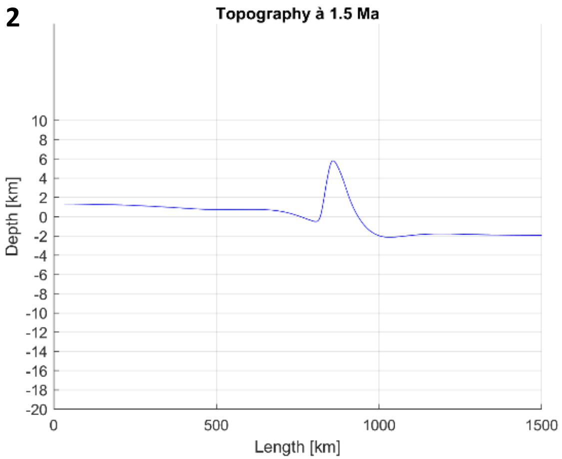

3
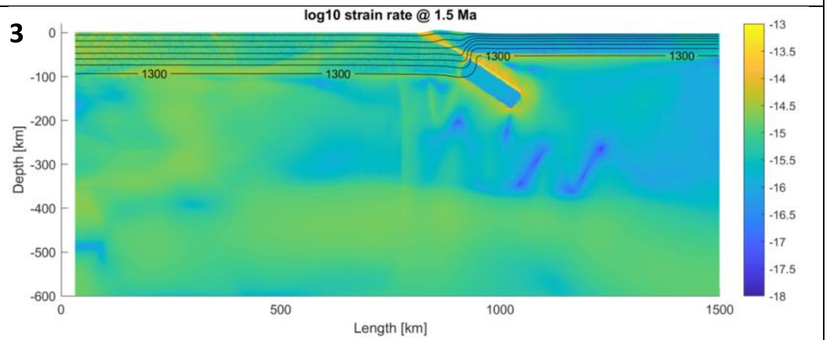

4

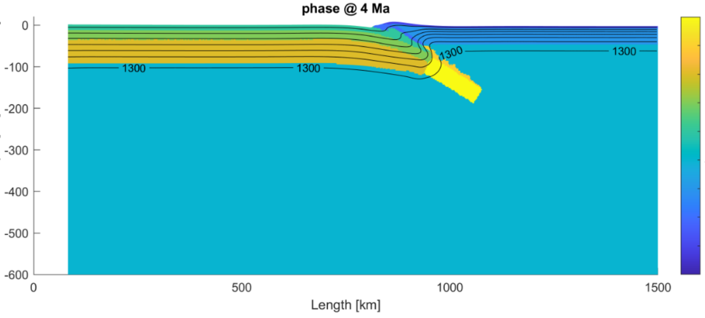
phase @ 4 Ma
Depth [km]
Length [km]
1300

5

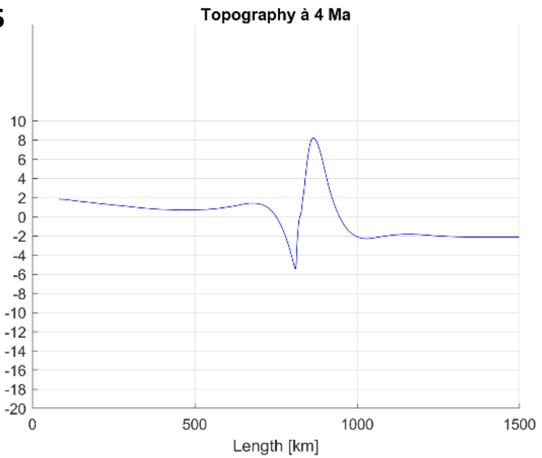
Topography à 4 Ma
Depth [km]
Length [km]

6

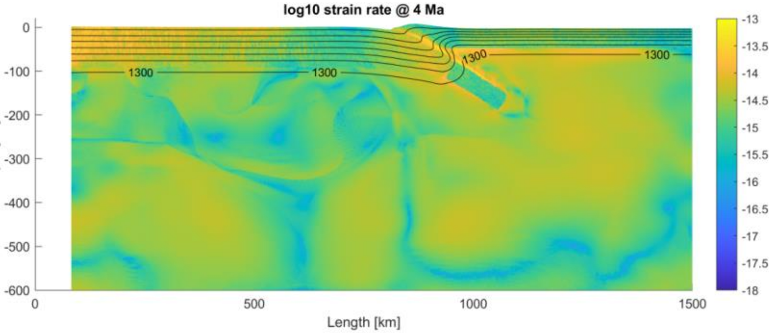
log10 strain rate @ 4 Ma
Depth [km]
Length [km]
1300

7

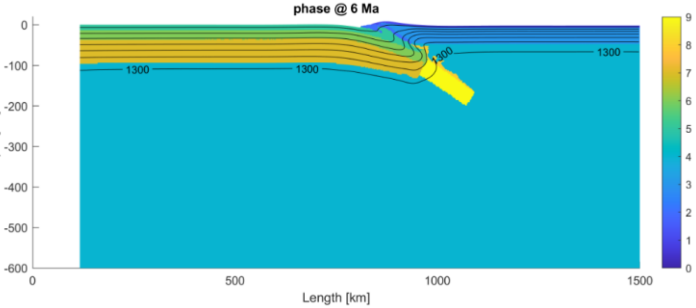
phase @ 6 Ma
Depth [km]
Length [km]
1300

8

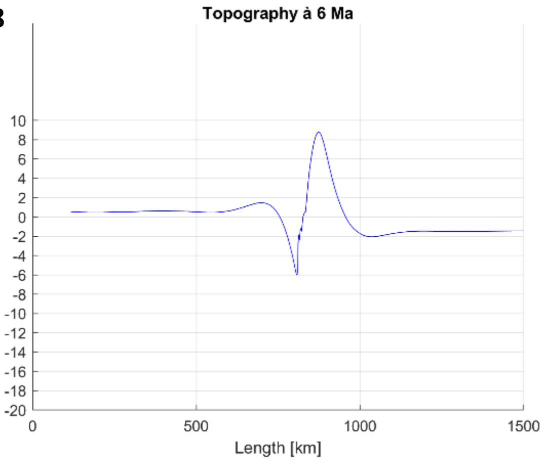
Topography à 6 Ma
Depth [km]
Length [km]

9

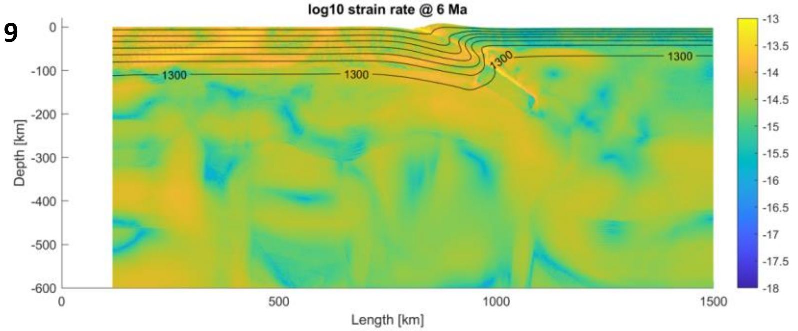
log10 strain rate @ 6 Ma
Depth [km]
Length [km]
1300

10 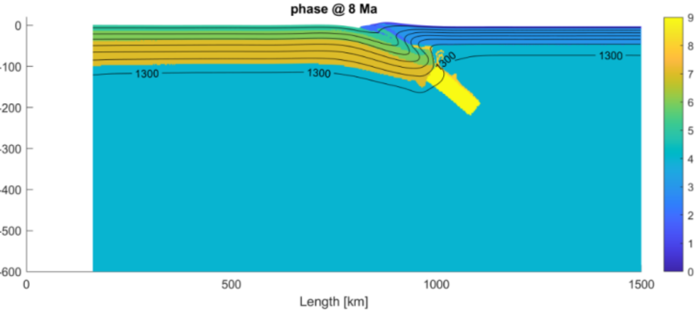	11 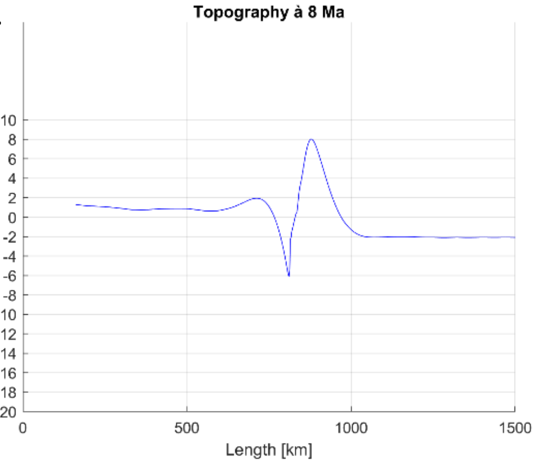	12 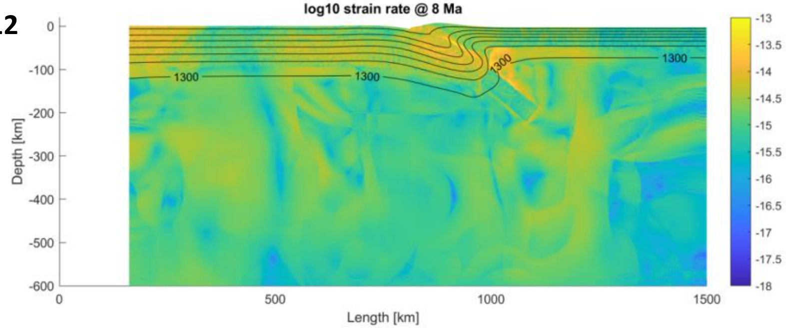
13 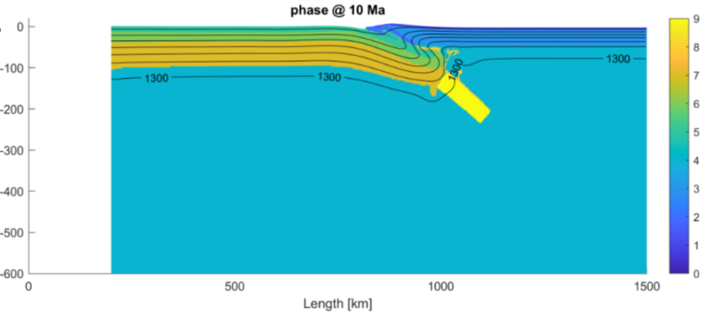	14 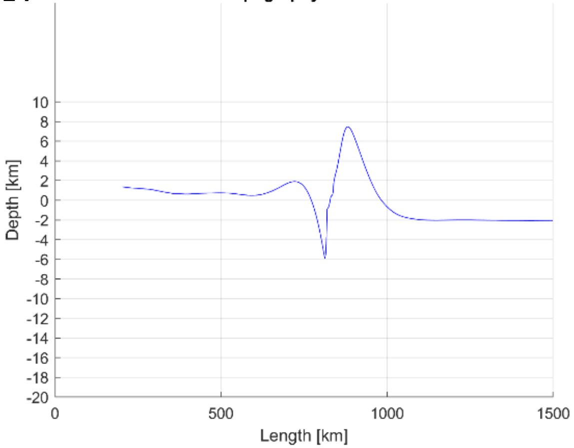	15 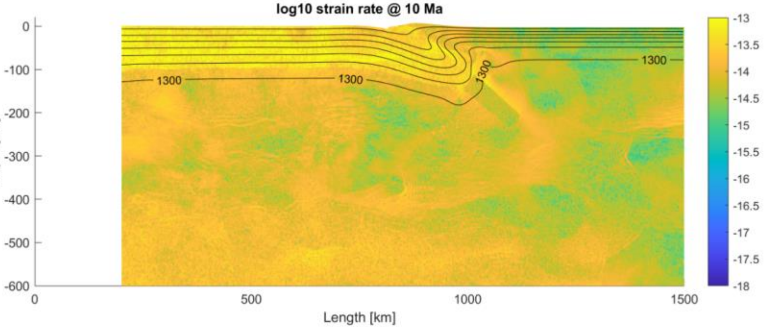

Table A.6 Phase, topography and strain rate results of Model 6.

Appendix A.7 Model 7 Oceanic-continental lithosphere

Phases	Topography	Strain rate
1 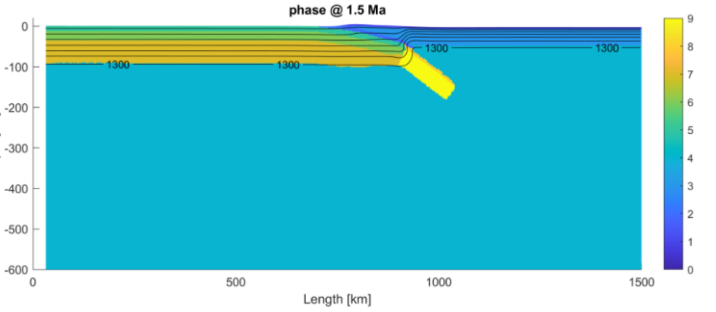	2 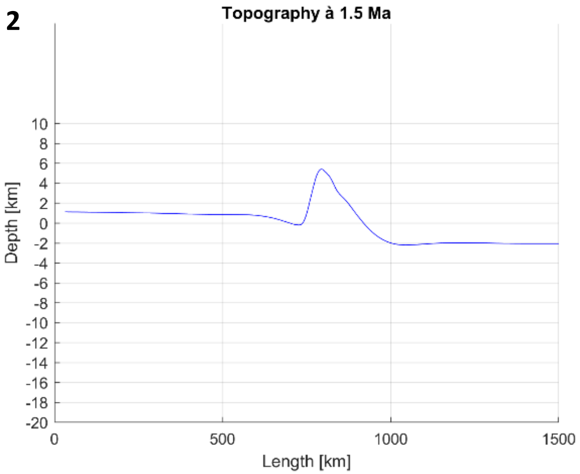	3 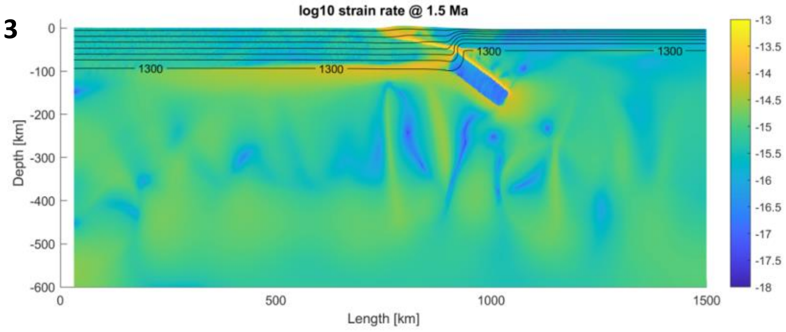
4 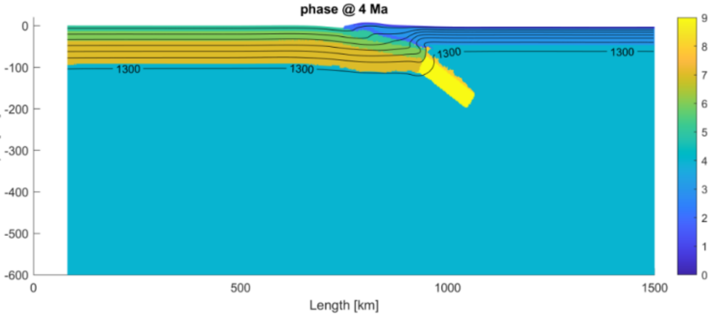	5 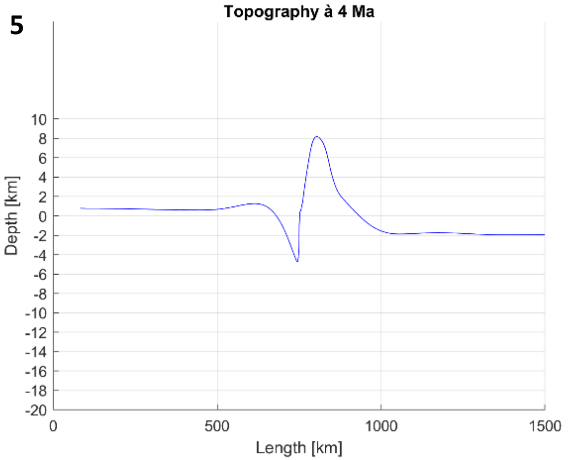	6 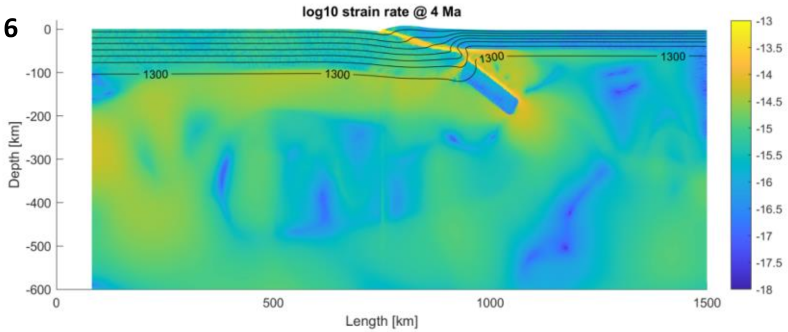

7

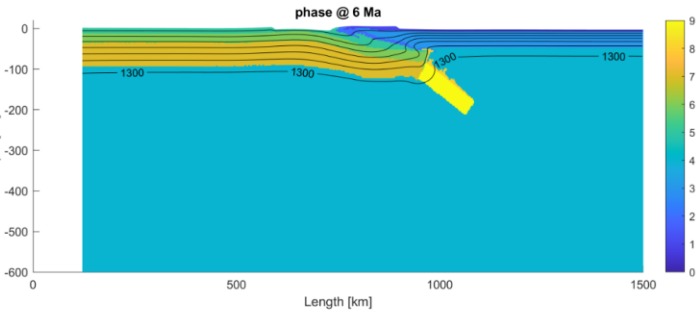
phase @ 6 Ma
Depth [km]
Length [km]
1300

8

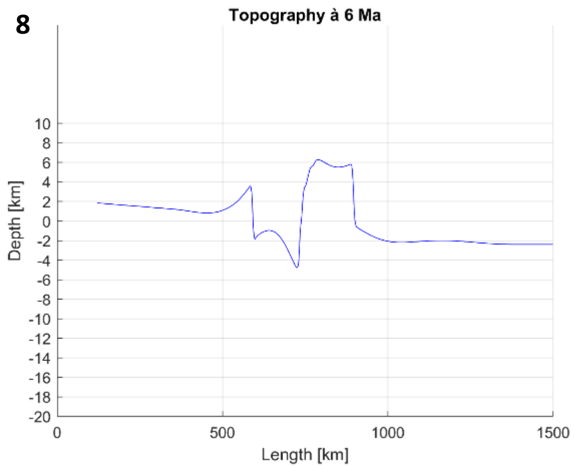
Topography à 6 Ma
Depth [km]
Length [km]

9

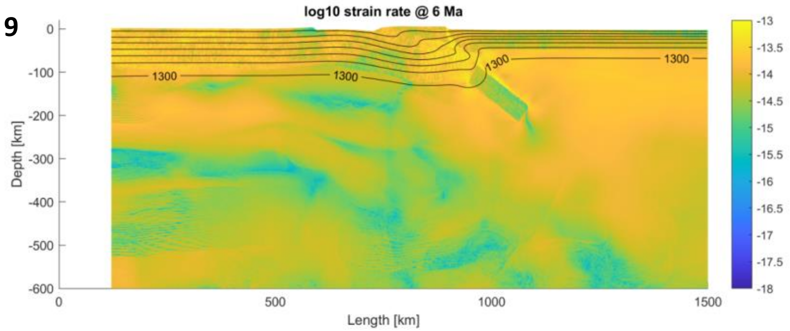
log10 strain rate @ 6 Ma
Depth [km]
Length [km]
1300

10

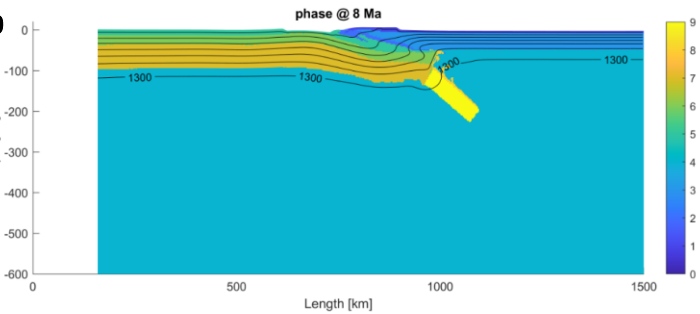
phase @ 8 Ma
Depth [km]
Length [km]
1300

11

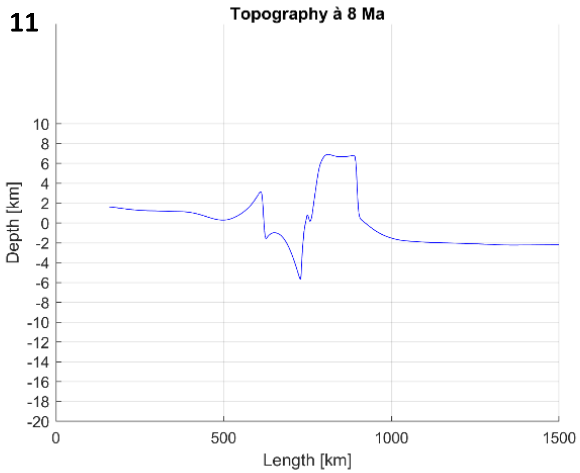
Topography à 8 Ma
Depth [km]
Length [km]

12

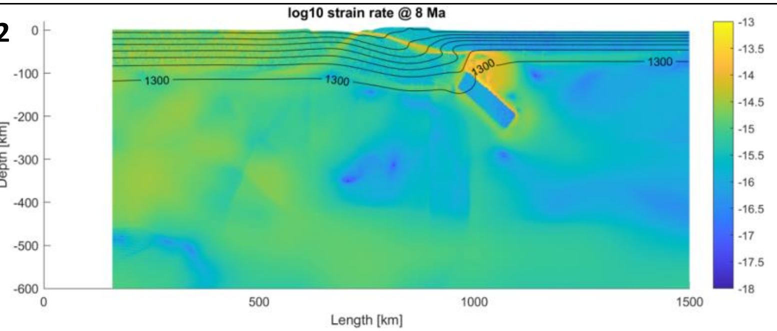
log10 strain rate @ 8 Ma
Depth [km]
Length [km]
1300

13 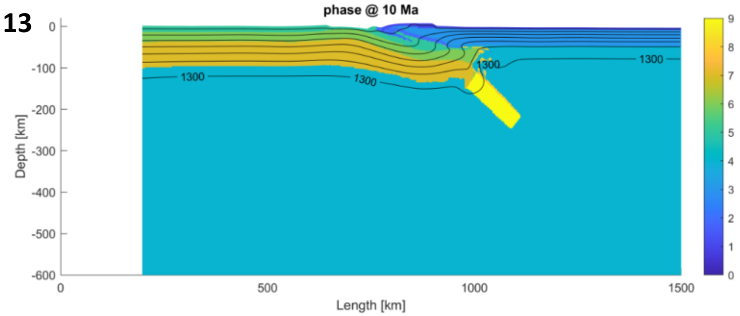	**14** 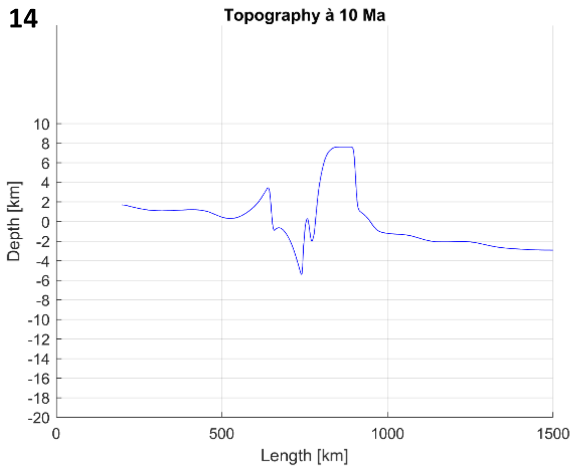	**15** 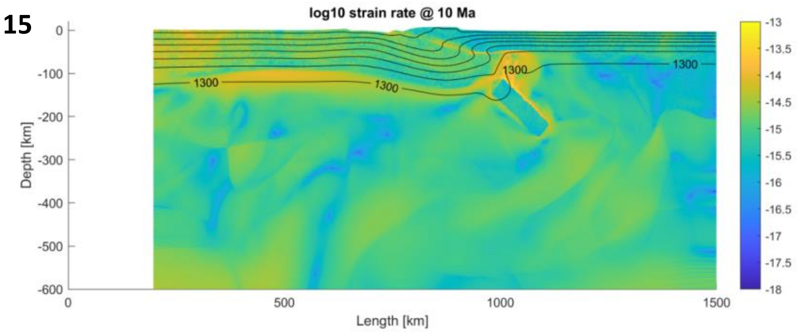

Table A.7 Phase, topography and strain rate results of Model 7.

Appendix A.8 Model 8 Oceanic-continental lithosphere

Phases	Topography	Strain rate
1 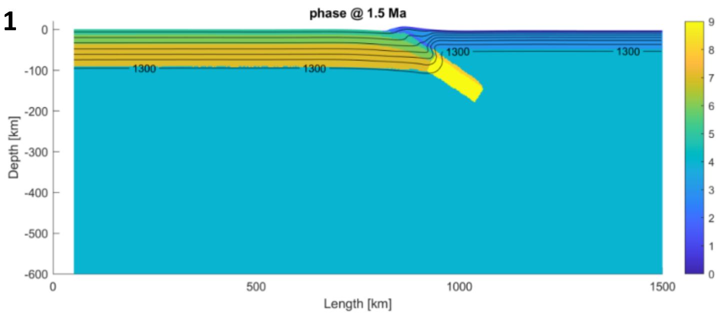	**2** 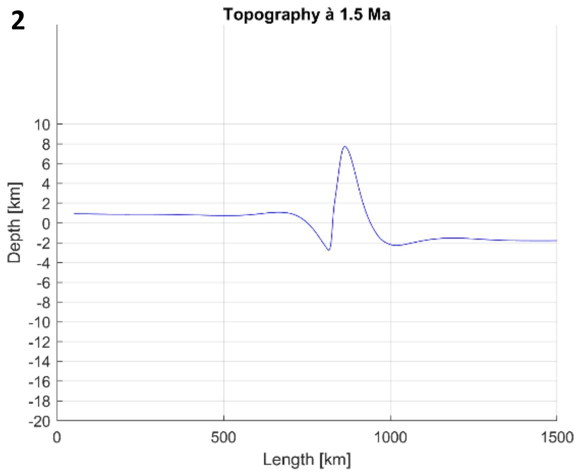	**3** 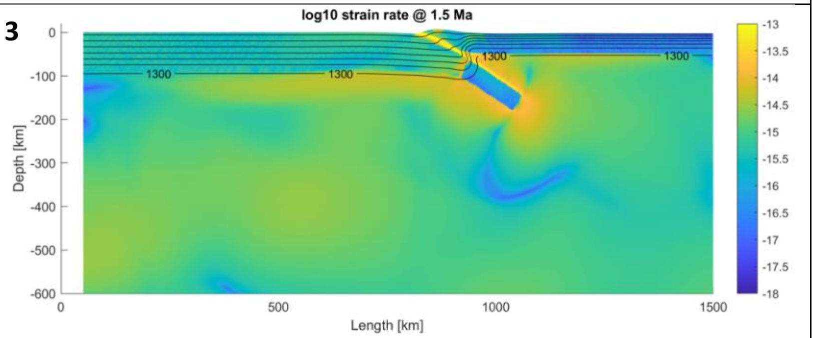

4
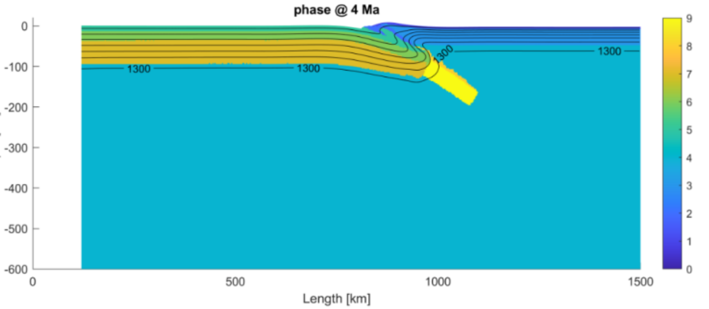
phase @ 4 Ma
Depth [km]
Length [km]
1300
1300
1300
1300

5
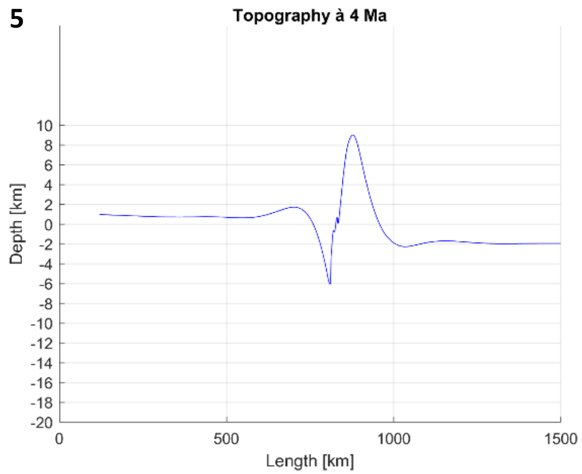
Topography à 4 Ma
Depth [km]
Length [km]

6
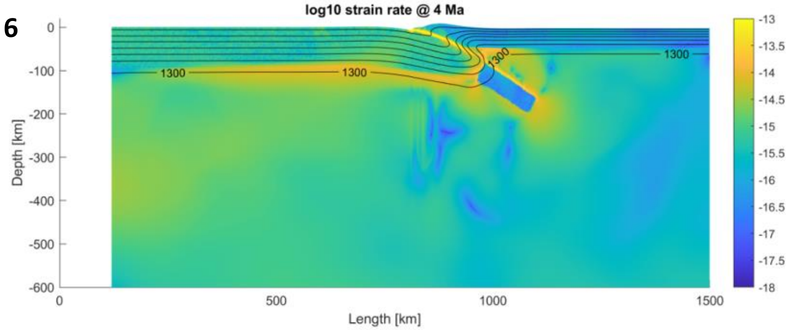
log10 strain rate @ 4 Ma
Depth [km]
Length [km]
1300
1300
1300
1300

7
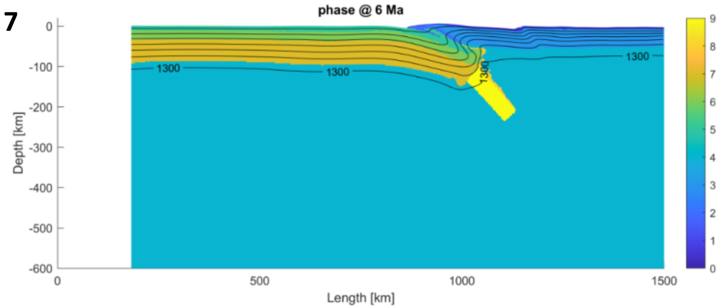
phase @ 6 Ma
Depth [km]
Length [km]
1300
1300
1300
1300

8
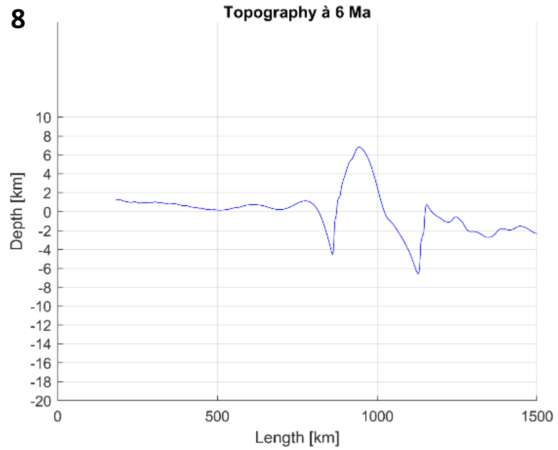
Topography à 6 Ma
Depth [km]
Length [km]

9
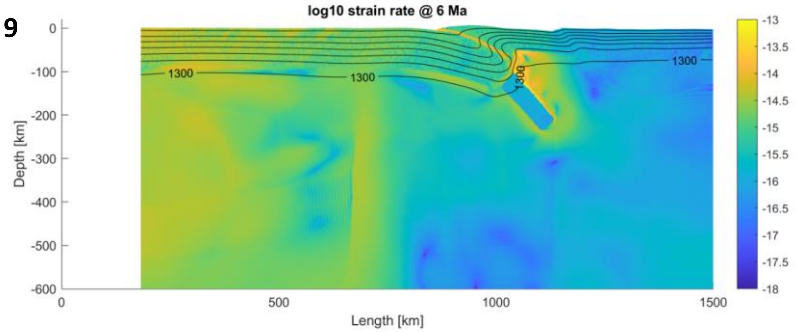
log10 strain rate @ 6 Ma
Depth [km]
Length [km]
1300
1300
1300
1300

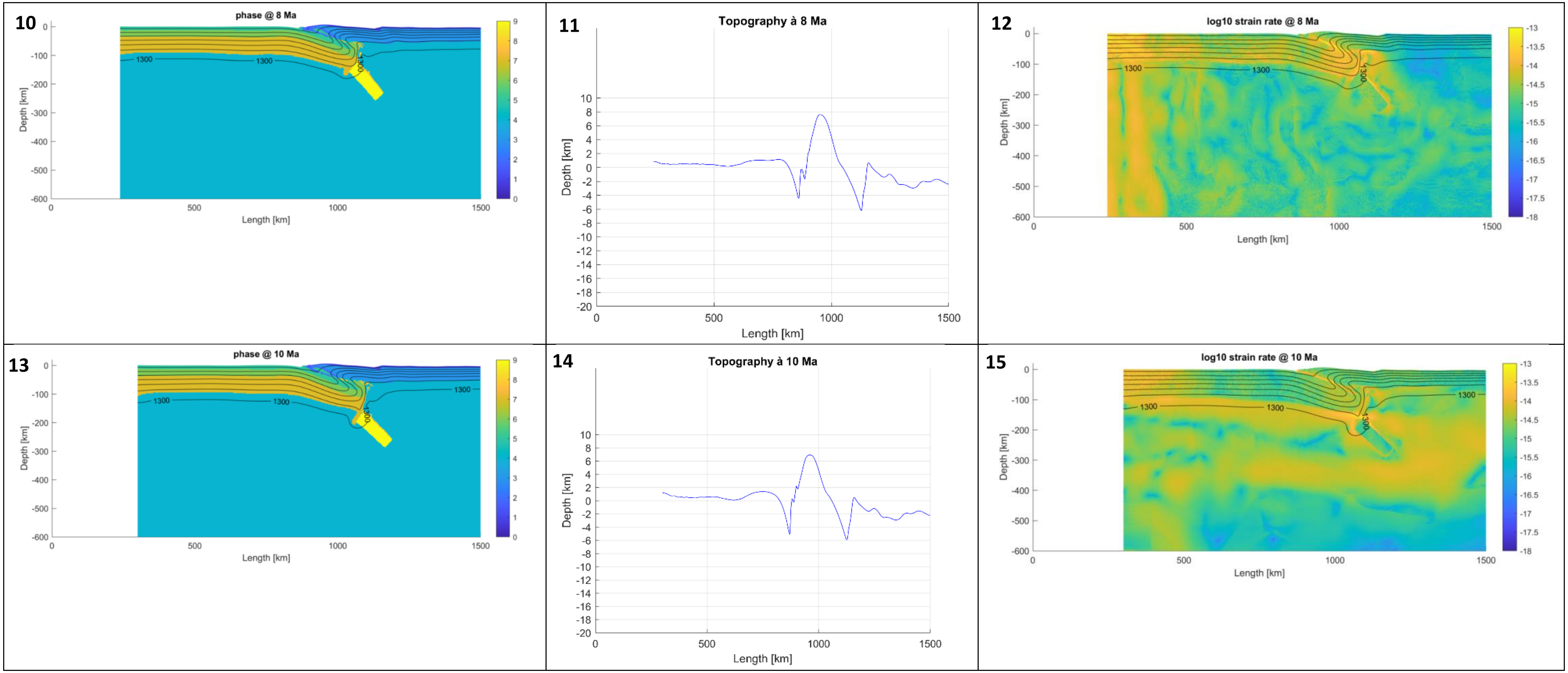

Table A.8 Phase, topography and strain rate results of Model 8.

Appendix A.9 Model 9 Oceanic-continental lithosphere

Phases	Topography	Strain rate
1 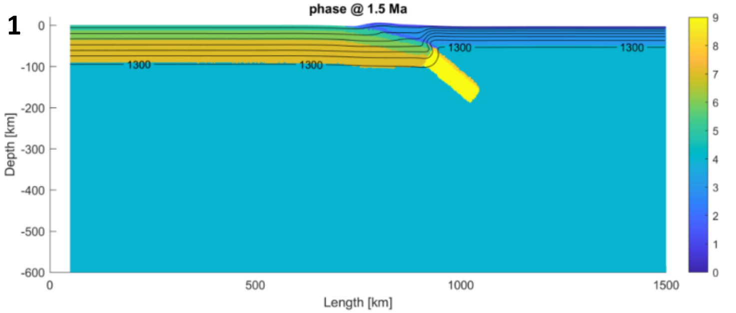	2 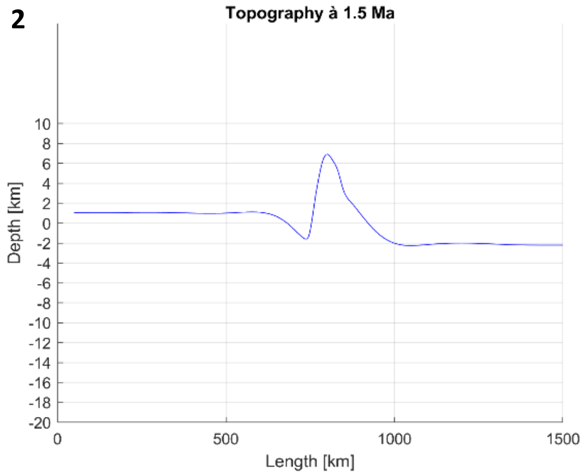	3 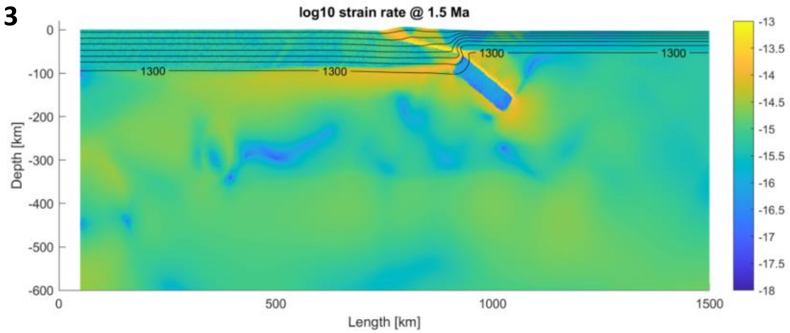
4 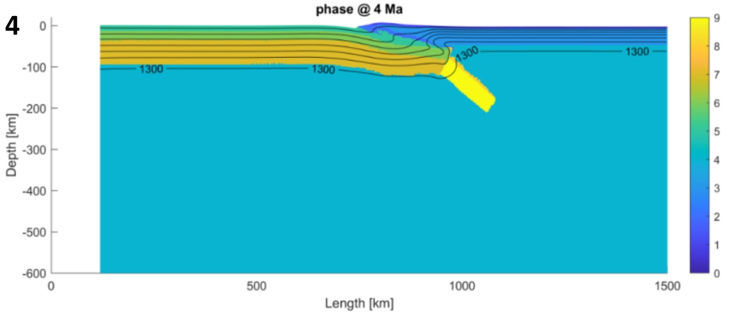	5 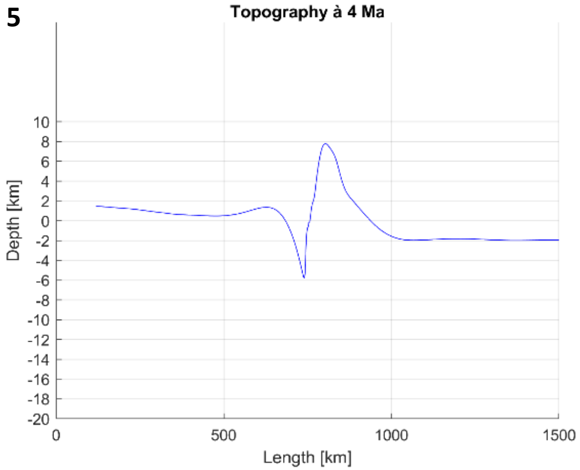	6 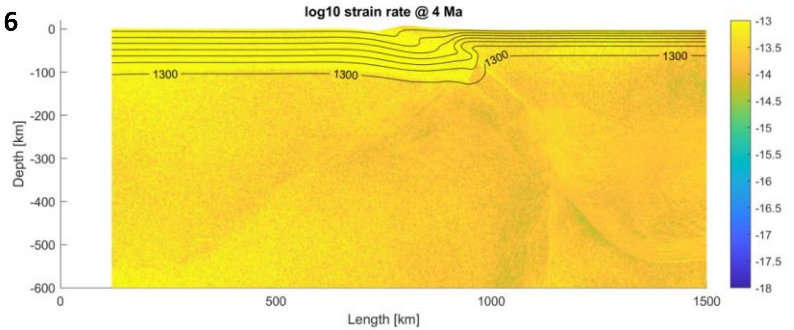

7
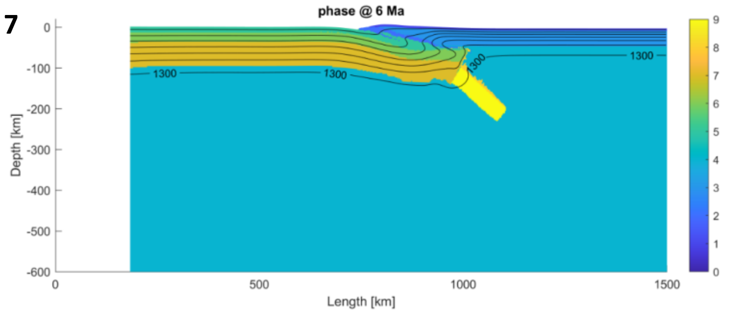
phase @ 6 Ma
Depth [km]
Length [km]
1300

8
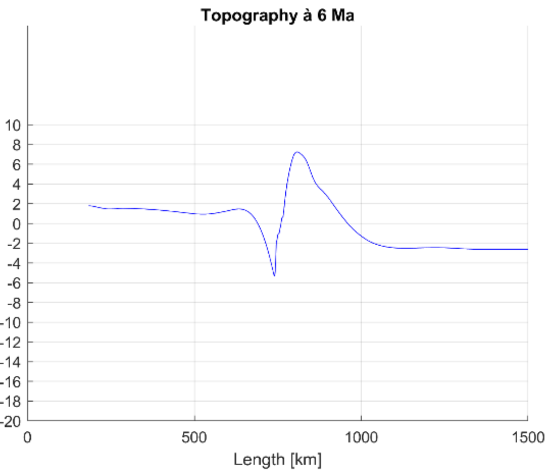
Topography à 6 Ma
Depth [km]
Length [km]

9
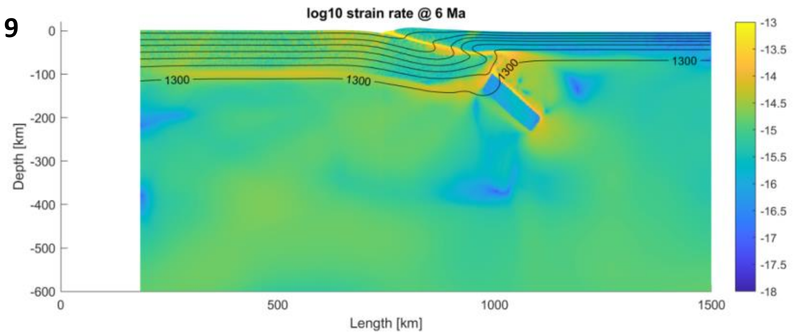
log10 strain rate @ 6 Ma
Depth [km]
Length [km]
1300

10
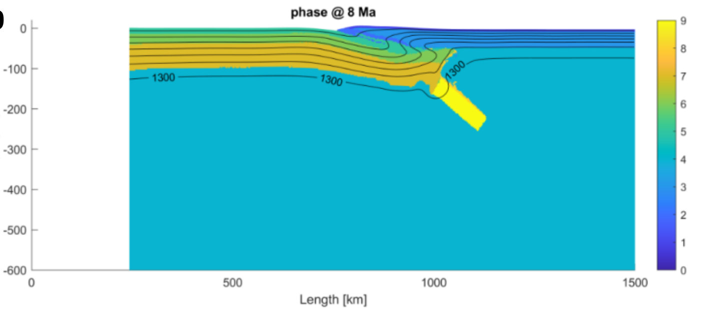
phase @ 8 Ma
Depth [km]
Length [km]
1300

11
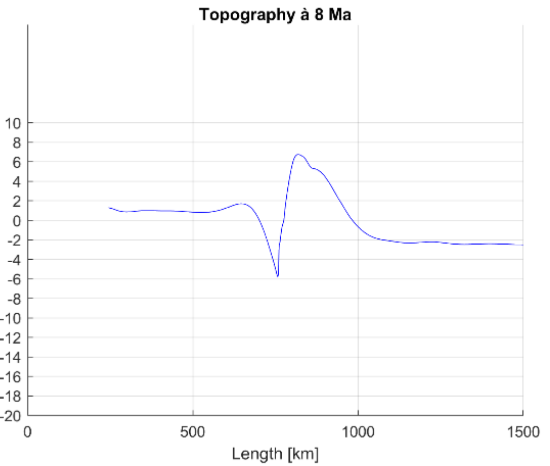
Topography à 8 Ma
Depth [km]
Length [km]

12
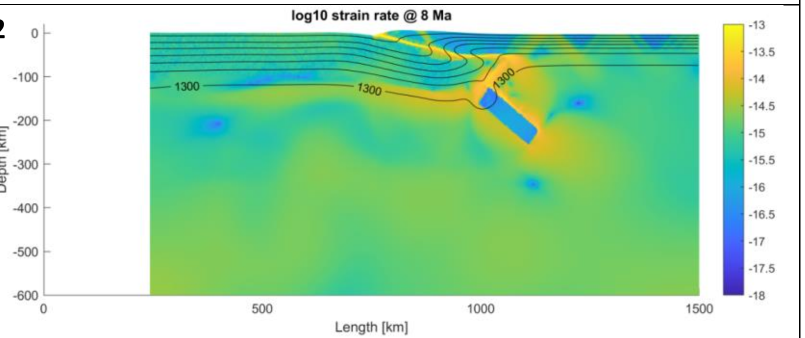
log10 strain rate @ 8 Ma
Depth [km]
Length [km]
1300

13

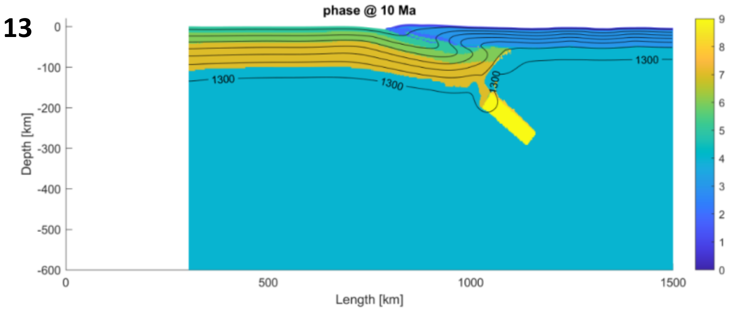

14

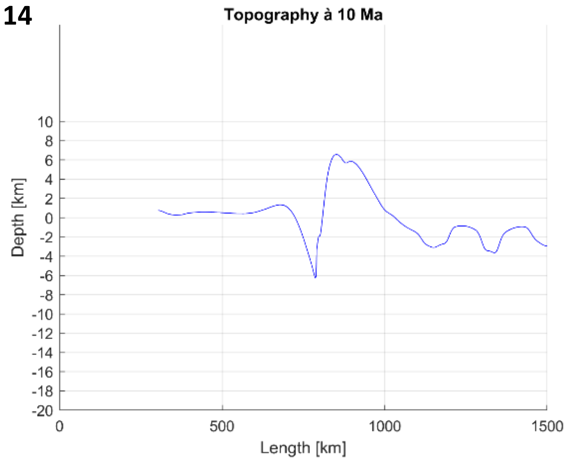

15

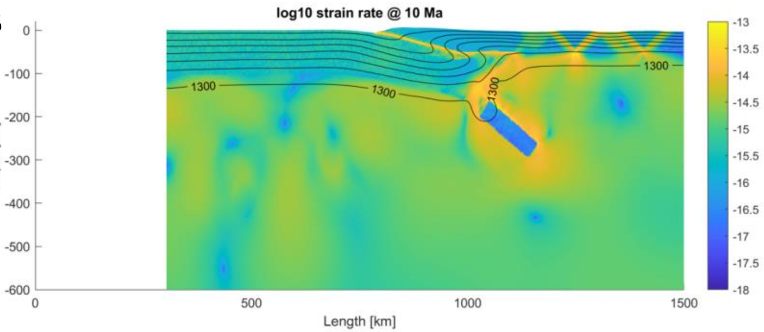

Table A.9 Phase, topography and strain rate results of Model 9.